# DEVELOPMENT OF A NOVEL LINEAR MAGNETOSTRICTIVE

# ACTUATOR

A Dissertation

by

ALI SADIGHI

Submitted to the Office of Graduate Studies of
Texas A&M University
in partial fulfillment of the requirements for the degree of

DOCTOR OF PHILOSOPHY

August 2010

Major Subject: Mechanical Engineering

# DEVELOPMENT OF A NOVEL LINEAR MAGNETOSTRICTIVE

# ACTUATOR

A Dissertation

by

ALI SADIGHI

Submitted to the Office of Graduate Studies of
Texas A&M University
in partial fulfillment of the requirements for the degree of

DOCTOR OF PHILOSOPHY

Approved by:

| | |
|---|---|
| Chair of Committee, | Won-Jong Kim |
| Committee Members, | Hamid A. Toliyat |
| | Reza Langari |
| | Daniel A. McAdams |
| Head of Department, | Dennis O'Neal |

August 2010

Major Subject: Mechanical Engineering

# ABSTRACT

Development of a Novel Linear Magnetostrictive Actuator.

(August 2010)

Ali Sadighi, B.S., Sharif University of Technology, Tehran;

M.S., K.N. Toosi University of Technology, Tehran

Chair of Advisory Committee: Dr. Won-Jong Kim


This dissertation presents the development of a novel linear magnetostrictive actuator. The magnetostrictive material used here is Terfenol-D, an alloy of the formula $Tb_{0.3}Dy_{0.7}Fe_{1.92}$. In response to a traveling magnetic field inside the Terfenol-D element, it moves in the opposite direction with a peristaltic motion. The proposed design offers the flexibility to operate the actuator in various configurations including local and conventional three-phase excitation.

The conceptual design of the linear magnetostrictive actuator was performed during which different configurations were analyzed. Finite Element Analysis (FEA) was extensively used for magnetic circuit design and analysis in conceptual design. Eventually one of these designs was chosen based on which detailed design of linear magnetostrictive actuator was carried out. A new force transmission assembly incorporates spring washers to avoid the wear due to the sudden collision of Terfenol-D element with the force transmission assembly. All mechanical parts were then fabricated at the mechanical engineering machine shop.

The power electronics to operate the motor in a local three-phase mode was designed and implemented. It was demonstrated that the power consumption can be

reduced significantly by operating the magnetostrictive linear actuator in the local excitation mode.

A finite-element model of the actuator was developed using ATILA and an empirical model was presented using the data gathered from numerous tests performed on the actuator. The closed-loop control system was implemented using relay control which resulted in an optimal closed-loop performance. The magnetostrictive actuator has demonstrated 410-N load capacity with a travel range of 45 mm, and the maximum speed is 9 mm/min. The maximum power consumption by the motor is 95 W.

The sensorless control of the linear magnetostrictive actuator was successfully conducted using two different approaches. First, using a linear-approximation method, we achieved a position estimation capability with ±1 mm error. Then, an adaptive neuro-fuzzy inference system was employed for estimating the position which resulted in a position estimation capability with only a ±0.5 mm error.

In the name of Allah, most gracious, most merciful

# ACKNOWLEDGMENTS

# TABLE OF CONTENTS

Page

# LIST OF FIGURES

Page

# LIST OF TABLES

# CHAPTER I

# INTRODUCTION

## 1.1 Background and Motivation

Electric actuators have found many industrial applications and are extensively used in machine-tool sliding tables, pen recorders, textile sewing machine, free piston pumps and compressors, etc. [1], [2]. However, there are key applications which impose limits on the space required for the actuator or its power consumption. Meeting all these requirements is a challenging task which pushes us to explore new technologies for the development of such actuators [3]. Hydraulic motors, despite their high-force-generating capability, are not applicable where ample space is unavailable to accommodate the auxiliary parts of the hydraulic system such as a hydraulic pump. On the other hand, direct-drive linear electric motors could not compete with hydraulic ones in generating high forces, so rotary motors have been combined with gear reducers and ball or lead screws to increase the force capability. This approach, although effective in many situations, requires the added complexity of a speed reducer and introduces backlash.

Considering these limitations, attentions have been paid to smart materials as a new approach to develop novel actuators. Among them, giant magnetostrictive materials are in competition with piezo ceramics [4], [5]. The magnetostrictive materials have found their place in specific applications such as low-voltage, high-force actuators, high-power low-frequency transducers, and space cryogenic positioning. In other cases piezo-ceramic actuators are employed because of their low-power consumption and high-output energy per unit mass [6].

_____

This dissertation follows the style of *IEEE/ASME Transactions on Mechatronics*.

**1.2    Review of Prior Art**

The electrical energy is transformed into the mechanical energy by means of the magnetic field in magnetic actuators. The mechanical motion in mechanical actuators is assumed to be over a limited range unlike the motors where the range of motion can be unlimited. In the following sections, first the conventional actuators such as solenoid, and moving-coil transducers will be presented and then two main types of non-conventional actuators, i.e. piezoelectric and magnetostrictive actuators are discussed.

**1.2.1    Conventional Actuators**

Electromagnetics is one of the most common methods used for energy conversion in electromechanical actuators. This is due to high energy density in electromagnetic actuators in comparison with their electrostatic counterparts. The electromechanical energy conversion takes place in the air gap which separates the stationary part and the moving part [7]. The two fundamental principles governing the electromagnetic actuators are Lorentz's law of electromagnetic forces and Faraday's law of electromagnetic induction which are briefly described here.

**Lorentz's Law of Electromagnetic Force**

Lorentz's law states that when a current carrying conductor is placed in a magnetic field, it will be subjected to an induced force (shown in Fig. 1.1) given by

$$\vec{F} = \vec{i} \times \vec{B}$$

where $\vec{F}$ is the force vector, $\vec{i}$ is the current vector, and $\vec{B}$ is the magnetic flux density. The force is called the electromagnetic force or the Lorentz force [7].

*F*
*Electromagnetic*
*force*

*i*
*Electric current*

*B*
*Flux density*
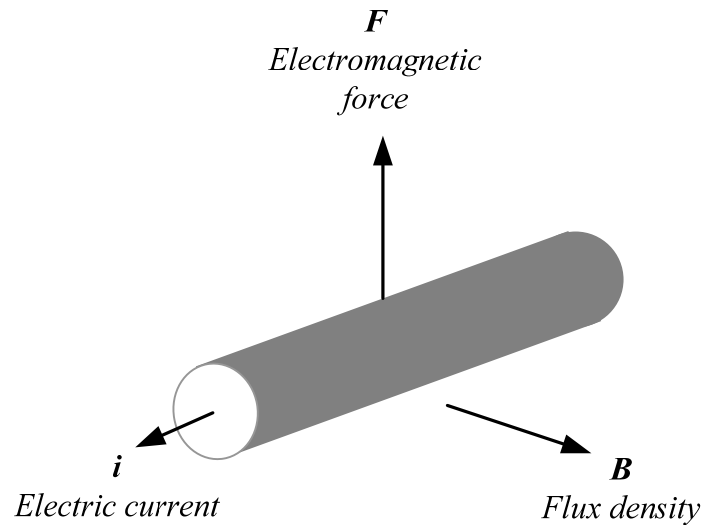
Fig. 1.1 Lorentz's force.

**Faraday's Law of Electromagnetic Induction**

The motion of a conductor in a magnetic field will produce an electromotive force (emf), or electric potential, across the conductor given by

$$emf = E = -\frac{d\phi}{dt}$$

where $\phi$ is the magnetic flux [7].

**Solenoid Actuators**

The solenoid actuator is available in linear and rotary configuration and used for variety of applications such as switches and relays. The schematic of a solenoid valve is shown in Fig. 1.2.

A solenoid consists of a stator, an armature, and a coil. By energizing the coil, the magnetic field is induced inside the coil and the armature moves toward the stator to increase the flux linkage. The generated magnetic force is approximately proportional to the square of

the coil current and is inverse proportional to the square of the air gap, which is the stroke of

the solenoid. When the coil is de-energized, the armature moves back to its initial position

either by its load or by means of a return spring [7].
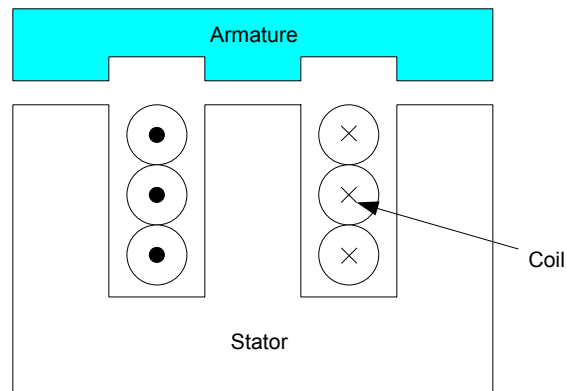


(a)



(b)

Fig. 1.2 (a) Schematic diagram of a solenoid actuator (b) Solenoid actuators [8].

**Voice Coil Actuator**

A voice-coil actuator (Fig. 1.3) consists of a moving coil (armature) and a permanent magnet. The permanent magnet induces the required magnetic field whose interaction with the current in the coil generates the Lorentz force and moves the armature. There is a linear relationship between the generated force and the coil current. This along with the bidirectional motion capability makes a voice-coil actuator more attractive than a solenoid actuator [7].



(a)



(b)
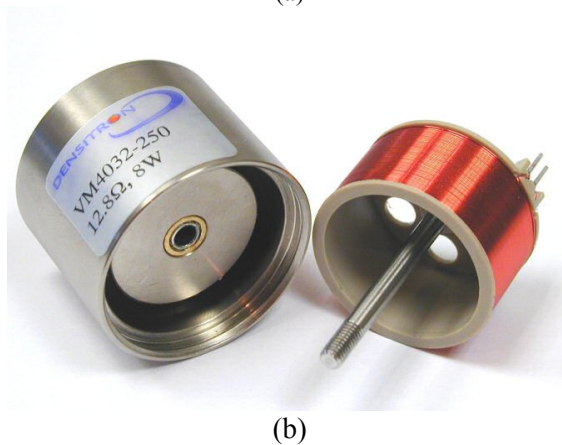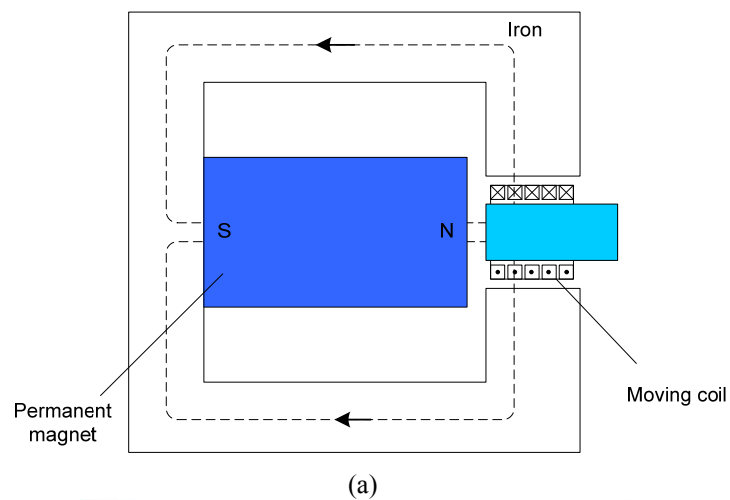
Fig. 1.3. (a) Schematic diagram of a voice-coil actuator (b) A voice-coil actuator (Source: Densitron Inc.).

### 1.2.2    Non-Conventional Actuators

Non-conventional actuators are those that do not follow the fundamental working principles of the conventional actuators as seen in the previous section. Smart-material-based actuators are among non-conventional actuators. They incorporate a smart material in the structure of the actuator and their working principle vary based on the properties of the specific material incorporated. When a smart material is exposed to an external stimuli, its shape changes. This property can be used for developing new types of actuators and sensors. Piezoelectric ceramics and magnetostrictive alloys are among the most popular smart materials to be described here.

**Piezoelectric Actuator**

Certain materials produce electric charges on their surfaces when a mechanical stress is applied and the induced charges are proportional to the mechanical stress. This is called the direct piezoelectric effect and was discovered in quartz by Pierre and Jacques Curie in 1880. Materials showing this phenomenon conversely have a geometric strain proportional to an applied electric field. This is the converse piezoelectric effect, verified by Gabriel Lippmann in 1881 [9]. The converse piezoelectric effect is the phenomenon employed in the development of piezoelectric actuators.  Some applications of piezoelectric actuators are shown in Fig. 1.4 and described below [7]:

a) Dampers: Piezoelectric dampers could convert the mechanical energy into the electrical energy. The electrical energy then could be dissipated as heat by short circuiting.

b) Microrobots: Piezoactuators are used in robot legs. By applying voltage to the electrodes, piezolegs are lengthened, shortened, or bent in any direction in a fine

movement.

c)  Micropump: A diaphragm is actuated by a piezoactuator, input and output check valves are subsequently opened for liquid or gas pumping. Advantages are fast switching and a high compression rate.

d)  Microgripper: A piezoactuator works on contraction for gripping motion based on the compliant mechanism. A gripper is of very small size and almost any required geometrical shape.

e)  Micromanipulator: Due to the unlimited resolution, piezoactuators are used in numerous positioning applications.

f)  Microdosage device: Piezoactuators allow a high-precision dosage of a wide variety of liquids in a range of nanoliters for various applications.
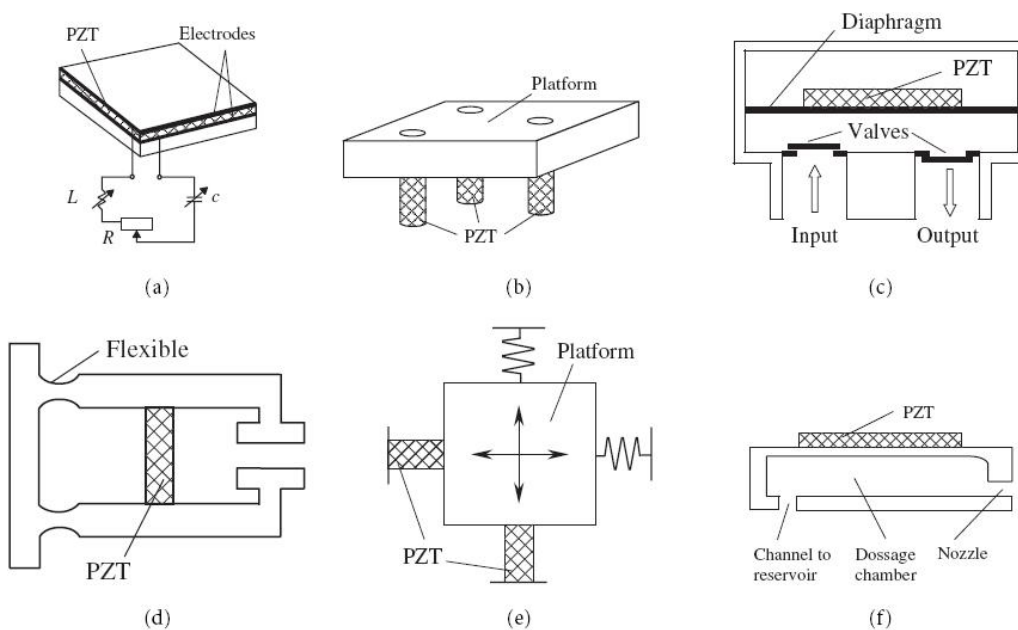


Fig. 1.4. Applications of piezoelectric actuators [7].

**Magnetostrictive Actuators**

Magnetostriction was discovered by James Joule in the 19th century. Magnetostriction can be described most generally as the deformation of a body in response to a change in its magnetization (Fig. 1.5). Terfenol-D, an alloy of formula $Tb_{0.3}Dy_{0.7}Fe_{1.92}$, was developed in the 1950's at the Naval Ordnance Laboratory. This alloy has the highest magnetostriction of any alloy, up to 2000 ppm [10], [11]. Due to this small magnetostriction strain level, most of the available magnetostrictive actuators are capable of generating high forces within a very small range of actuation. One of the first studied applications of these materials was as a generator of force and motion for underwater sound sources [12], [13].
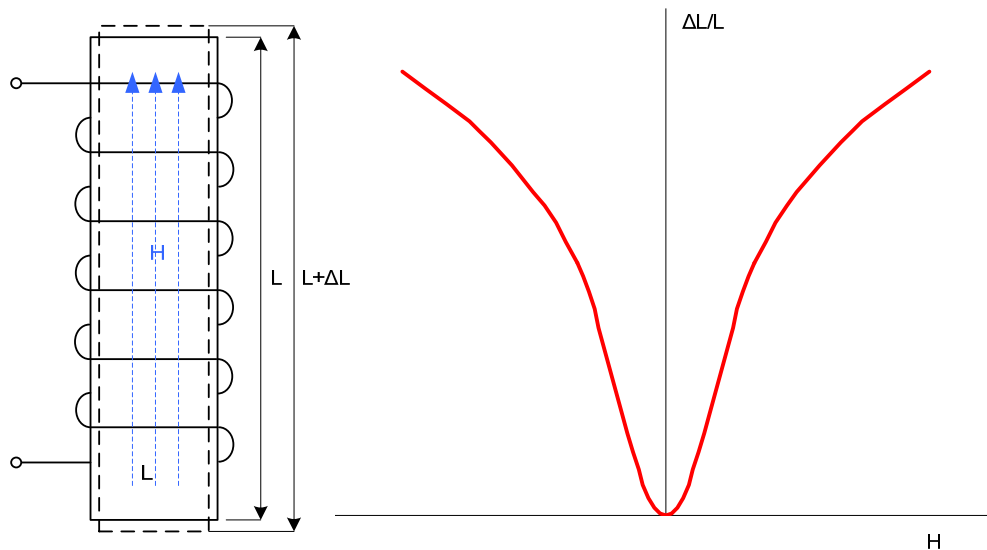


Fig. 1.5. Magnetostriction.

Magnetostrictive actuators could be classified in two main groups considering the mechanism through which they generate force and movement. One is direct motion control

and the other is indirect motion control. In direct motion control, the end of the active material (magnetostrictive material) is fixed. With the applied magnetic field, the active material could elongate through the other end. The main advantage of this mechanism is its relatively simple structure although high precision manufacturing is crucial in achieving the required performance of the actuator. Besides, these actuators usually have very limited range of operation (from hundredths to tenths of millimeter) which confines their applications. The schematic of a magnetostrictive actuator with direct motion control is shown in Fig. 1.6.
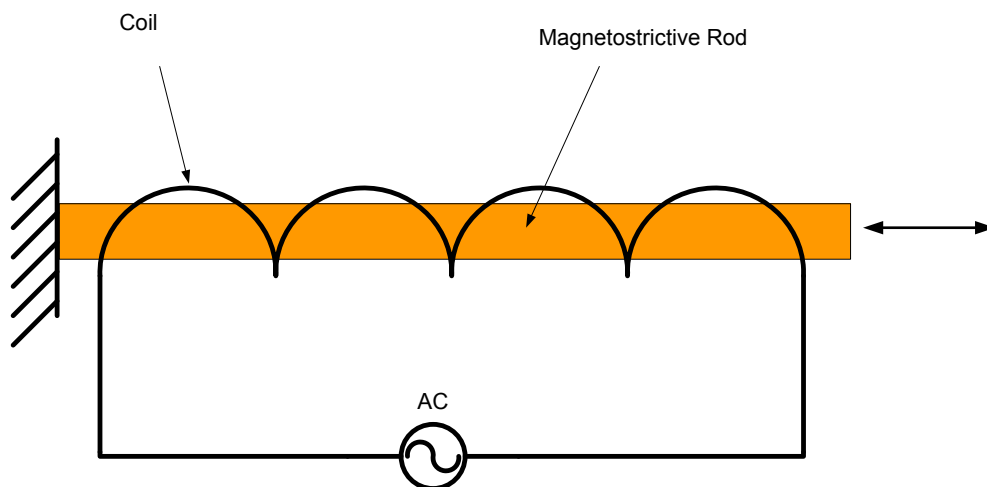
Fig. 1.6. Schematic diagram of a magnetostrictive actuator with direct motion control.

In indirect motion control, the magnetostrictive material is not fixed at one end and could move to generate the required force and extended-range motion. A schematic diagram of a magnetostrictive actuator with indirect motion control is shown in Fig. 1.7. When the left clamp is active, the circuit switch closes and make the magnetostrictive rod elongate to

the right. Then the right clamp is activated and the left clamp is deactivated. Now by opening the switch, the whole rod has had an overall movement to right. If we keep following this sequence or a reverse one, the actuator could move further to the right or left. Unlike the direct motion control, here we may achieve extended motion range.
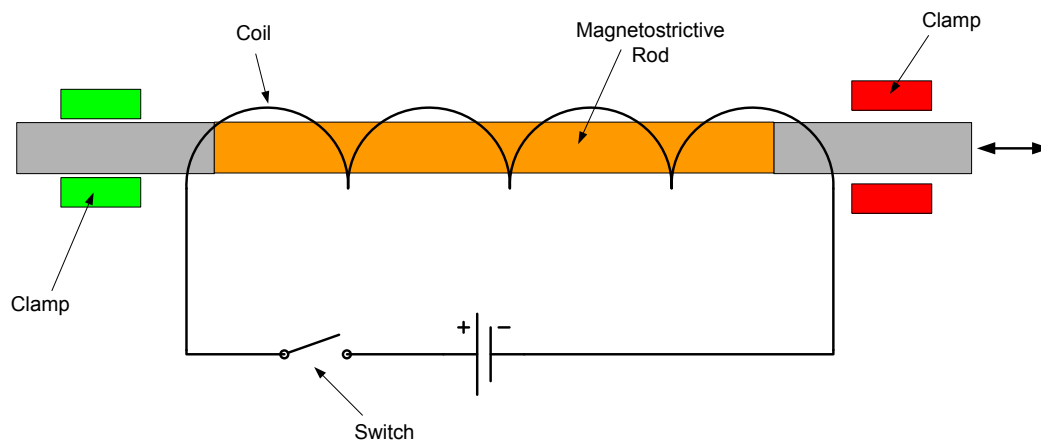


Fig. 1.7.  Schematic diagram of a magnetostrictive actuator with indirect motion control.

### 1.2.3    Kiesewetter Motor

A special type of magnetostrictive actuator with indirect motion control is Kiesewetter motor. Kiesewetter conceived of the idea of generating the peristaltic motion with a Terfenol-D rod in a tight-fitting tube [14]. The schematic of Kiesewetter motor is shown in Fig. 1.8. The main drawback of Kiesewetter motor is wear, which would cause a loose contact between the Terfenol-D rod and the tube, leading to the loss of its force-generating capability.

Coils

Magnetostrictive
Rod

Tube
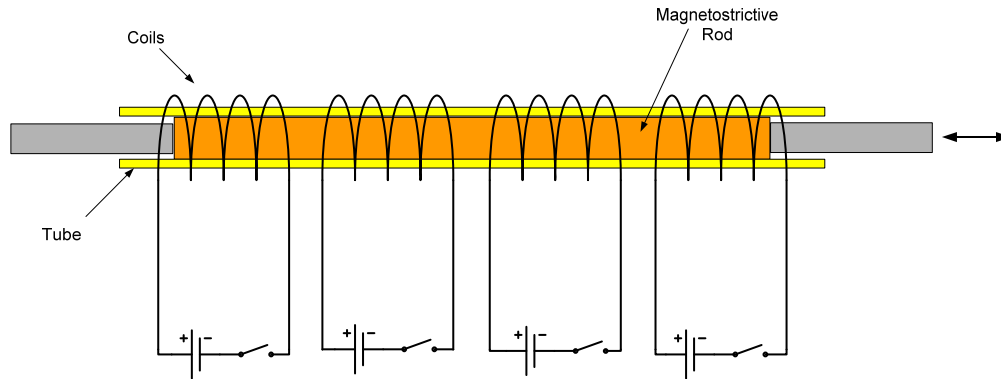
Fig. 1.8. Schematic diagram of Kiesewetter motor.

To overcome this problem Kim, et al. constructed an extended-range linear magnetostrictive motor with double-sided three-phase stators [15]. Unlike the Kiesewetter motor, they used Terfneol-D slab placed between two tight-fitting plates spring-loaded to maintain proper contact in spite of wear, thermal expansion, or motion. They demonstrated force generating capability up to 140 N and a travel range of 25 mm. However the power consumption was high due to applying conventional three-phase excitation in high frequency which gave rise to eddy-current loss [16].
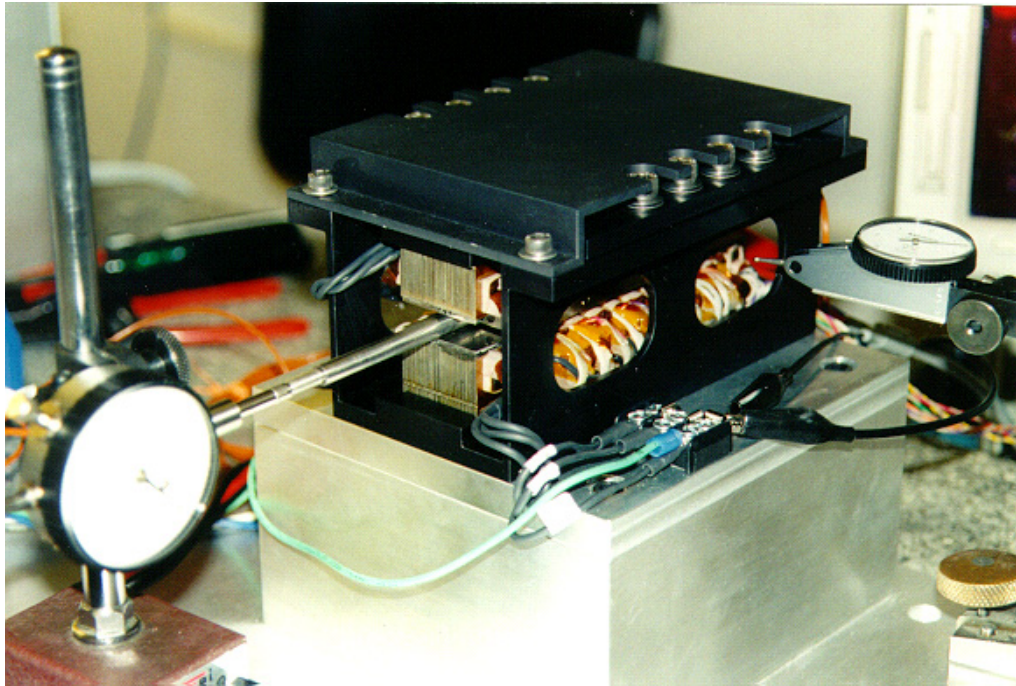
Fig. 1.9. Photograph of the extended-range linear magnetostrictive actuator with double-sided three-phase stators [15].

## 1.3 Contributions of This Dissertation

The main contribution of this dissertation is the development of a novel type of linear magnetostrictive actuator. To overcome the power consumption limitation, we designed and implemented a novel configuration for coils. In this actuator, the coils' magnetic axis coincides with the active element's magnetic axis, which aligns the direction of magnetic field inside the Terfenol-D slab better and results in higher magnetic flux density, and consequently, higher magnetostrictive strain. Furthermore, this design enables us to implement various operation modes such as the conventional multiphase excitation or a local multiphase excitation.

Another contribution of this dissertation is to implement the sensorless control for this novel type of actuator. This sensorless control scheme combined with the unique features of this class of actuator, i.e., self-braking and low-power consumption, is a promising alternative in applications where conventional methods of actuation and sensing are proved incapable due to technical or reliability issues.

### 1.3.1 Objectives

With reference to the previously mentioned pros and cons of available technologies, the objectives of this research are as follows:

(a) to design and construct a linear magnetostrictive actuator with high force-generating capability and low power consumption

(b) to design and implement the power electronics which results in a smooth operation of the linear magnetostrictive actuator

(c) to develop an effective closed-loop control system

(d) to develop a sensorless position monitoring and control of the linear magnetostrictive actuator

### 1.3.2 Dissertation Overview

This dissertation contains seven chapters. Chapter I presents a literature review of existing conventional and non-conventional actuators. Specifically in this chapter various types of magnetostrictive actuators are discussed, and their differences are studied.

In Chapter II, conceptual design of the linear magnetostrictive actuator is performed. In this stage, five different configurations for its key components such as stators, coils, and active element are proposed, and the finite-element analysis (FEA) is run for each of them.

By taking into account other design considerations such as ergonomics, ease of manufacturing, and assembly, the best conceptual design is chosen for detailed design.

Chapter III covers the electromechanical design of the linear magnetostrictive actuator. In this chapter, various components in the magnetic circuit are specified. The power electronics and instrumentation structure is also presented.

In Chapter IV, the mechanical design, fabrication, and assembly of the linear magnetostrictive actuator is discussed. In the end of this chapter the troubleshooting of the actuator is presented.

Chapter V is devoted to the experiment results, modeling and control. In this chapter after demonstrating the open-loop results, a modified model is given for the linear magnetostrictive actuator. Then the closed-loop control of the actuator is implemented using a relay-control scheme.

In Chapter VI, the sensorless position estimation and control of the actuator is presented. With the development of a fundamental relationship between the active element's position and the coils' inductances, two different approaches are developed for sensorless position estimation. Then, the sensorless closed-loop control of the actuator is presented.

Chapter VII concludes this dissertation with a summary of the achievements in this work and suggestions for possible future work. Appendices include the engineering drawings of mechanical components and the Simulink® block diagrams used to control the actuator.

# CHAPTER II

# CONCEPTUAL DESIGN

The first stage of the project was to develop the conceptual design. To be able to propose a conceptual design based on which the detailed design of the prototype magnetostrictive motor is developed, we considered various geometries like tubular and flat ones and a variety of configurations in which coils could be arranged. Then for each of these configurations, the mechanical and electrical basic design was carried out to get the approximate size of the Terfenol-D piece, stators and force transmission assembly. Based on this initial geometry, the main parts of the motor such as the Terfenol-D element, stators, coils and transmission assembly were modeled using Solidworks software. All these models then were transferred to Maxwell 3-D, a finite-element-analysis (FEA) software by ANSOFT, Inc. [17], where the magnetic circuit analysis of the motor was done. In Fig. 2.1, the overall design process of the magnetostrictive actuator has been shown. The magnetic flux density inside the Terfenol-D active material was studied carefully and a sensitivity analysis was performed to check the impacts of coil position on the active material magnetization. Eventually different parameters such as geometry, ergonomics, ease of manufacturability, ease of assembly, power consumption, and magnetic field concentration were used to compare the configurations, and finally one conceptual design was selected and the detailed design was proceeded based on that.

## 2.1 Design Configurations of Magnetostrictive Linear Actuator

The magnetostrictive linear motor could generally be categorized to two main groups of flat and tubular configurations. The other decisive factor is the arrangement of coils which

determines the overall geometry and features of the magnetostrictive linear motor. All possible configurations have been shown in Fig. 2.2 and will be explained in more details now.



Fig. 2.1. The overall design process of the magnetostrictive actuator.
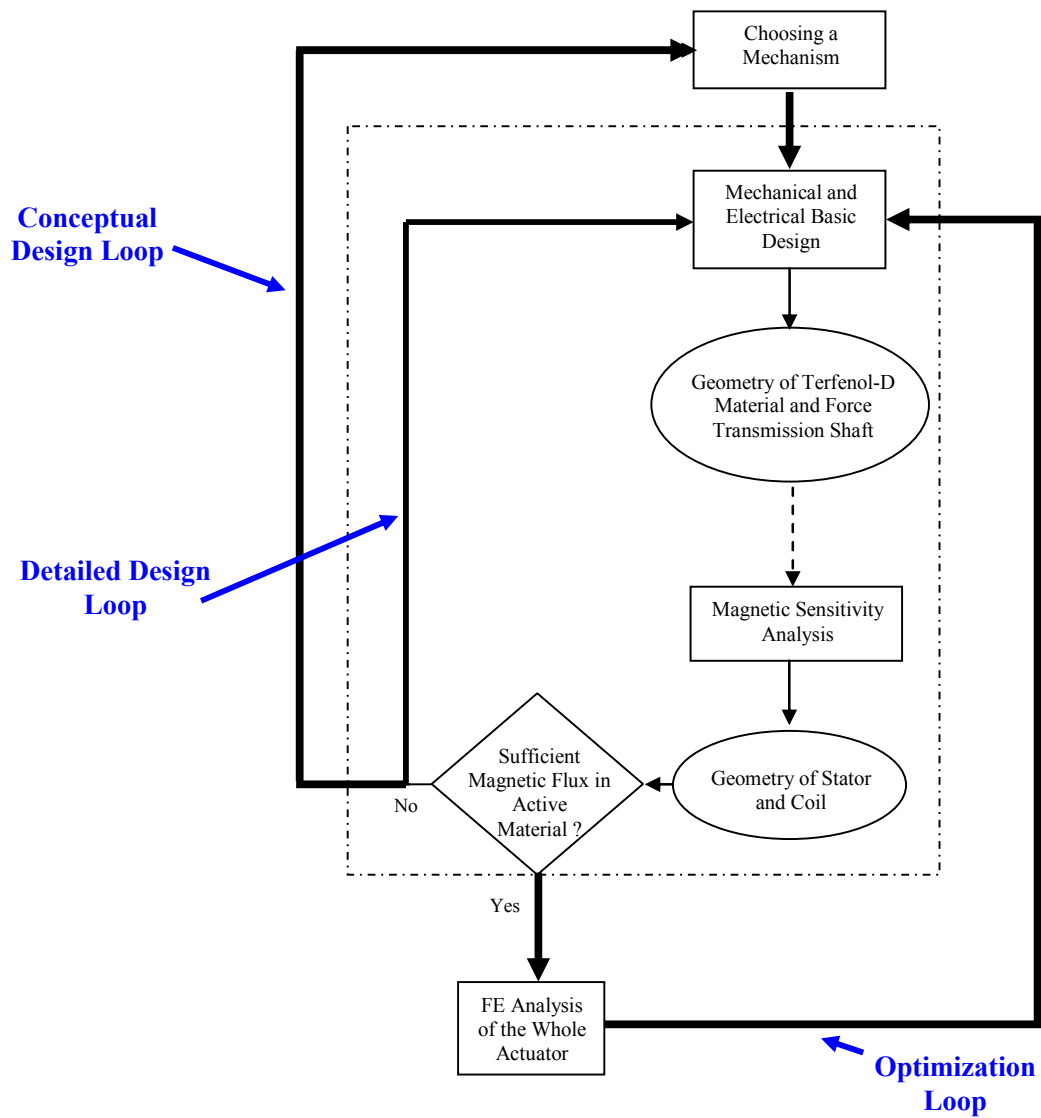
```
                    ┌─────────────────────┐
                    │ Magnetostrictive Linear │
                    │        Motor        │
                    └─────────────────────┘
```
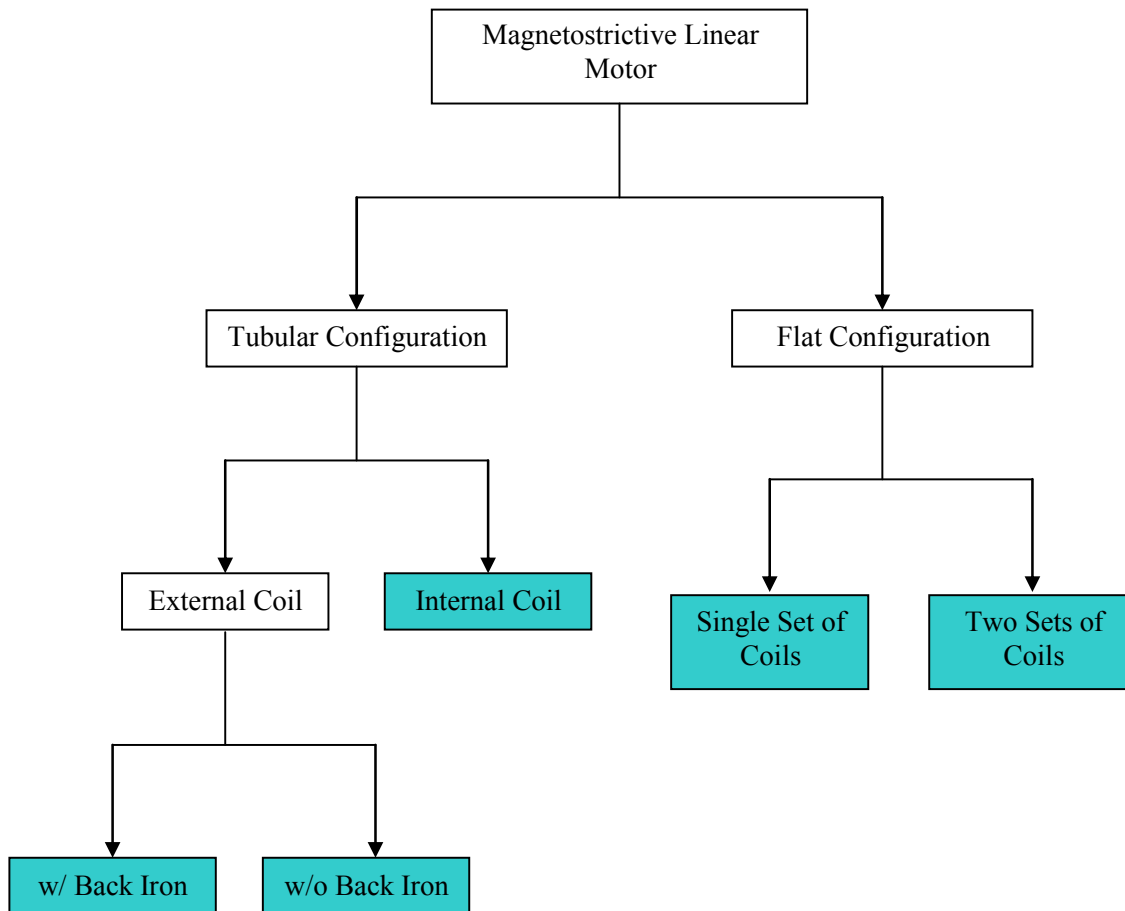
Fig. 2.2. Design configurations of magnetostrictive motor.

## 2.1.1    Conceptual Designs Description

Abovementioned   various configurations for magnetostrictive actuator are described below.


**Tubular Configuration, External Coil, without Back Iron**

In this configuration, the coils are put outside the tube in which the Terfenol-D rod has been fit. As seen in Fig. 2.3 there is no back iron and the generated force could be transmitted by a shaft going through the hollow Terfenol-D rod.
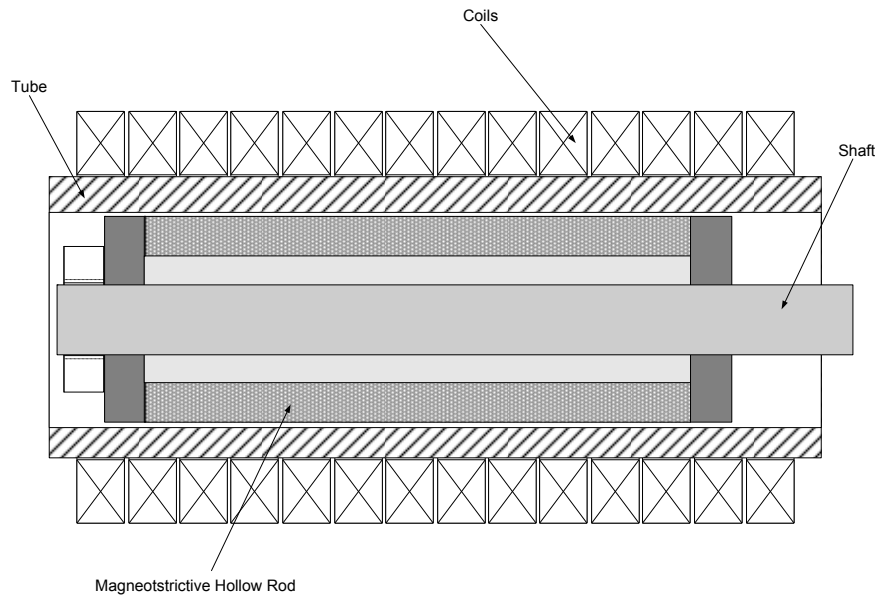
Fig. 2.3. Tubular configuration, external coil, without back iron.

**Tubular Configuration, External Coil, with Back Iron**

It is the same as the last configuration with the difference that back iron is used to lower the magnetic loss and increase the magnetic field concentration. Fig. 2.4 shows this configuration.
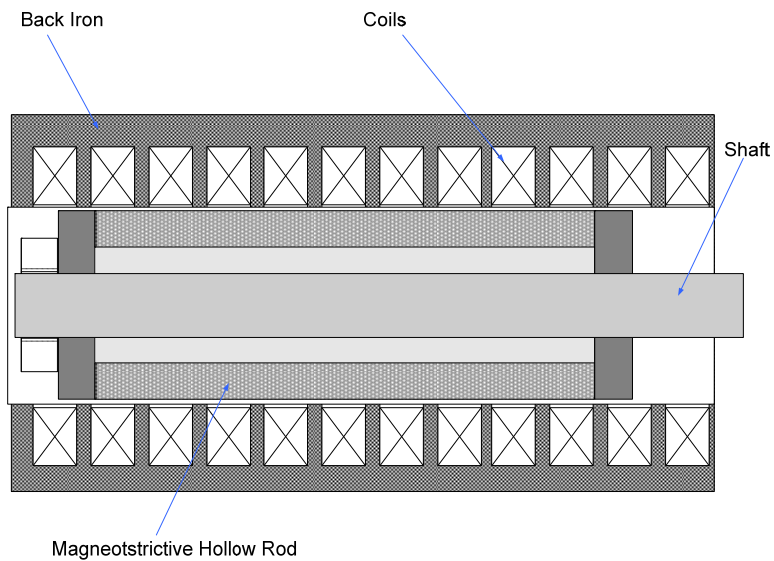


Fig. 2.4. Tubular configuration, external coil, with back iron.

## Tubular Configuration, Internal Coil

In this configuration, the coils have been put inside the hollow Terfenol-D rod as shown in Fig. 2.5. To lower the magnetic loss, the generated force is transmitted using a high-permeability shaft.
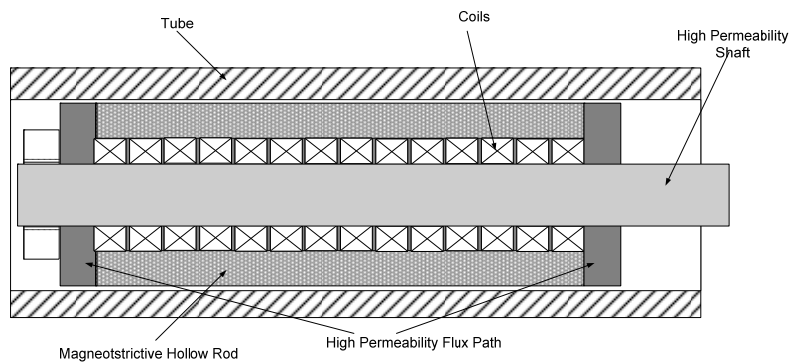


Fig. 2.5. Tubular configuration with internal coil.

## Flat Configuration, Two Sets of Coils

In this configuration, the Terfenol-D piece is in rectangular shape. As shown if Fig. 2.6, the coils are put separately in upper and lower stators.
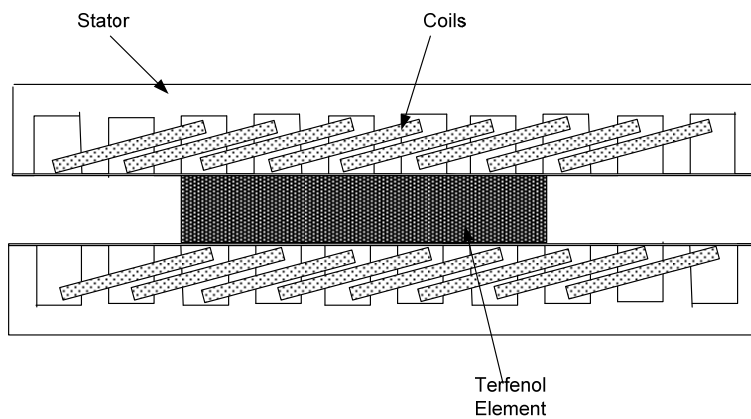


Fig. 2.6. Flat configuration, two sets of coils.

**Flat Configuration, Single Set of Coils**

It is the same as last configuration. The only difference is that the coils encircle the Terfenol-D element with only one set of coils. Fig. 2.7 shows this configuration.
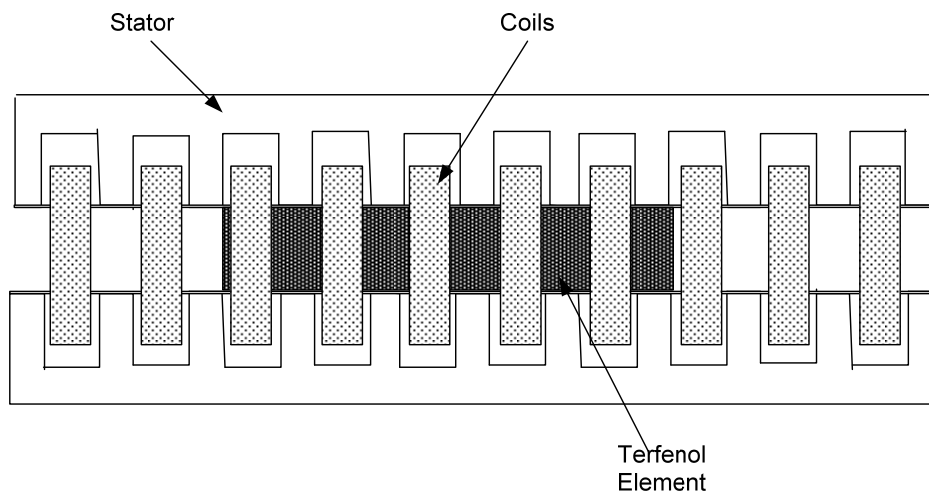


Fig. 2.7. Flat configuration, single set of coils.

## 2.2 Preliminary Design

To be able to do the magnetic-circuit analysis of magnetostrictive motor for each of the mentioned configurations, we carried out a preliminary mechanical design to get a sense of the overall dimensions of the key parts like the Terfenol-D element, stators, and the force transmission assembly. The Terfenol-D mechanical properties were taken from the ETREMA [18] datasheets. The stator material was chosen to be iron, and force transmission assembly, stainless steel grades with relative permeability close to one. Since the active

material is straight and the action line of force coincides with the axis of the active material and there is not any discontinuity or abrupt change in cross section, we may assume uniformly distributed stresses in preliminary design. Since Terfenol-D is a brittle material, the Coulomb-Mohr failure theory [19] is used for the Terfenol-D material and the maximum shear stress theory is used for stator and force transmitting assembly.

Depending on the required amount of magnetic flux density in the active material, we are able to calculate the number of turns and the current for each coil using Ampere's law. The calculated values for current and number of turns are only the starting points, based on which we could simulate the magnetic circuit. And then we optimize them to meet the power requirements of the motor.

There is a direct relation between the level of magnetostriction and the magnetic flux density inside the Terfenol-D active material. Thus the main objective of preliminary magnetic circuit design and analysis was to direct as much of the obtained flux as possible through the active material. Besides, by having a concentrated magnetic field in the active material we would be able to lower the power consumption and increase the force generating capability.

To reach the most accurate results on magnetic circuit design, an FEA was performed using Maxwell 3D. To do this, after carrying out the preliminary mechanical and electrical design, the 3-D models were developed in Solidworks and then they were imported to Maxwell for further analysis. To make the FEA less cumbersome, the magnetic field generated by only one coil was considered, and the overall current in that coil was held constant in different configurations to make the comparison possible.

## 2.3 Tubular Configuration, External Coil, without Back Iron

In Fig. 2.8 a 3-D model of such a linear motor is shown. The coils are placed outside the stator and the Terfenol-D rod is inside the squeezing tube which has some longitudinal slots which makes it flexible. The required friction force is generated using the normal pressure transferred by a wedge mechanism between the squeezing tube and the stator. Eventually the output force is transmitted using a stainless-steel shaft. To allow maximum flux density going through the Terfenol-D rod, the stator tube and the shaft should have low relative permeability. The manufacture of this mechanism is fairly easy, but attention should be paid in the design and construction of the wedge mechanism to assure the uniform normal pressure throughout the Terfenol-D rod.
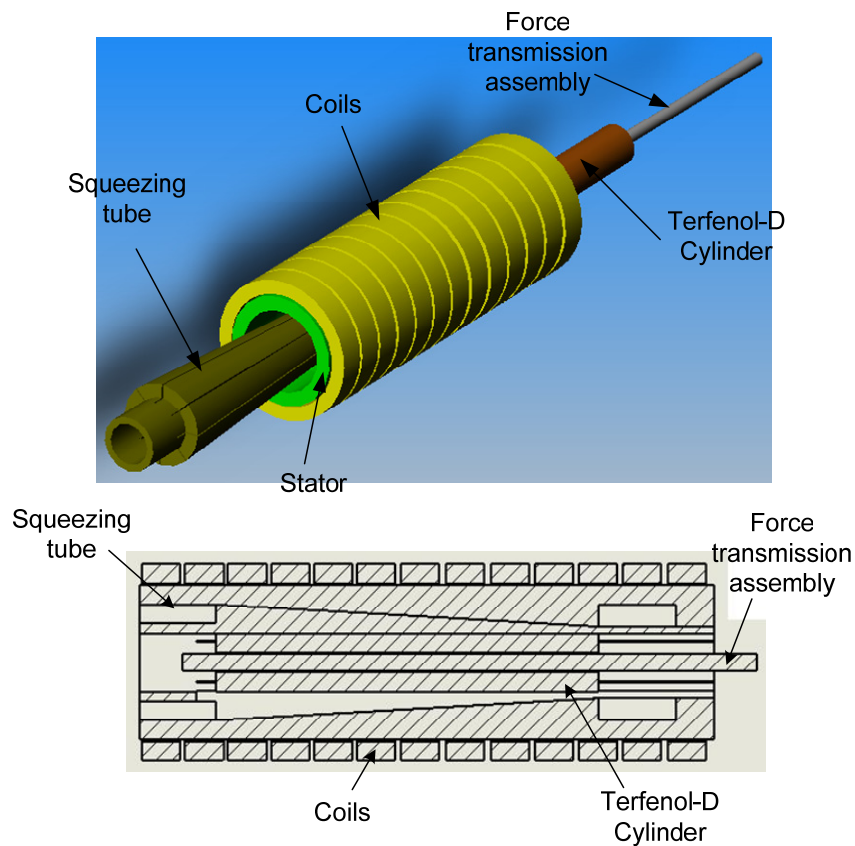


Fig. 2.8. Tubular configuration, external coils, without back iron.

A small number of components and a simple squeezing mechanism would have made the assembly of this linear motor quite easy. To carry out the FEA of this configuration, a simpler model was developed and some details such as wedge mechanism were discarded. In Table 2.1 the overall dimensions of the magnetostrictive linear motor in tubular configuration with external coils and without back iron are given.

Table 2.1. General dimensions used for FEA in tubular configuration, external coil, without back iron.

| Component | Material | Electrical Properties | Geometry Specification |
|:---:|:---:|:---:|:---:|
| Shaft | Stainless Steel | $\mu_r = 1.0$<br>$\sigma = 1.1 \times 10^6$ S/m | D = 9 mm<br>L = 200 mm |
| Active element | Terfenol-D | Nonlinear B-H curve specified in Fig. 2.9 | ID = 10 mm<br>OD = 30 mm<br>L = 200 mm |
| Stator tube | Brass | $\mu_r = 1.0$<br>$\sigma = 1.5 \times 10^7$ S/m | ID = 30 mm<br>OD = 40 mm<br>L = 200 mm |
| Coil | Copper | $\mu_r = 0.9999$<br>$\sigma = 5.8 \times 10^7$ S/m | ID = 42 mm<br>OD = 62 mm<br>L = 20 mm |

The materials of different parts were assigned using the Maxwell material library except for Terfenol-D which its nonlinear B-H curve was defined and added to the Maxwell material library. In Fig. 2.9, nonlinear B-H curve of Terfenol-D is shown. In Fig. 2.10, magnetic field intensity and magnetic flux density inside the Terfenol-D rod has been shown. In Fig. 2.11, the magnetic flux density in the whole space is shown and in Fig. 2.12, the magnetic flux density distribution in the cross-section of the Terfenol-D rod is shown.
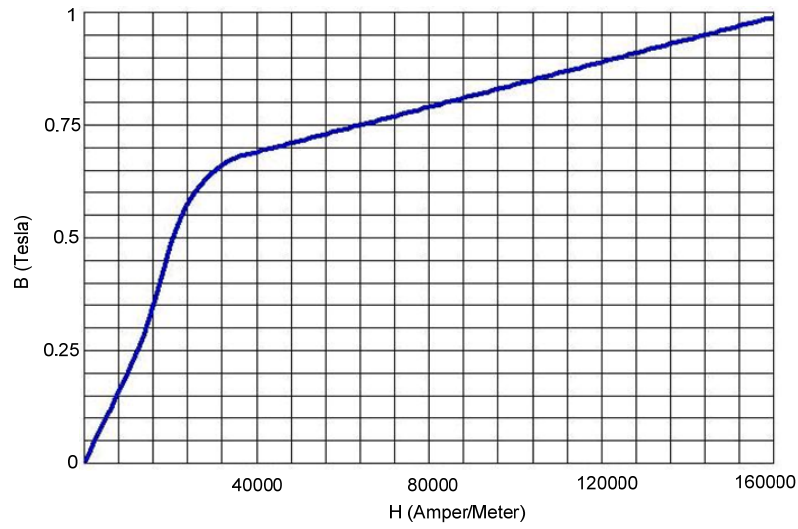
Fig. 2.9. Nonlinear B-H curve of Terfenol-D.
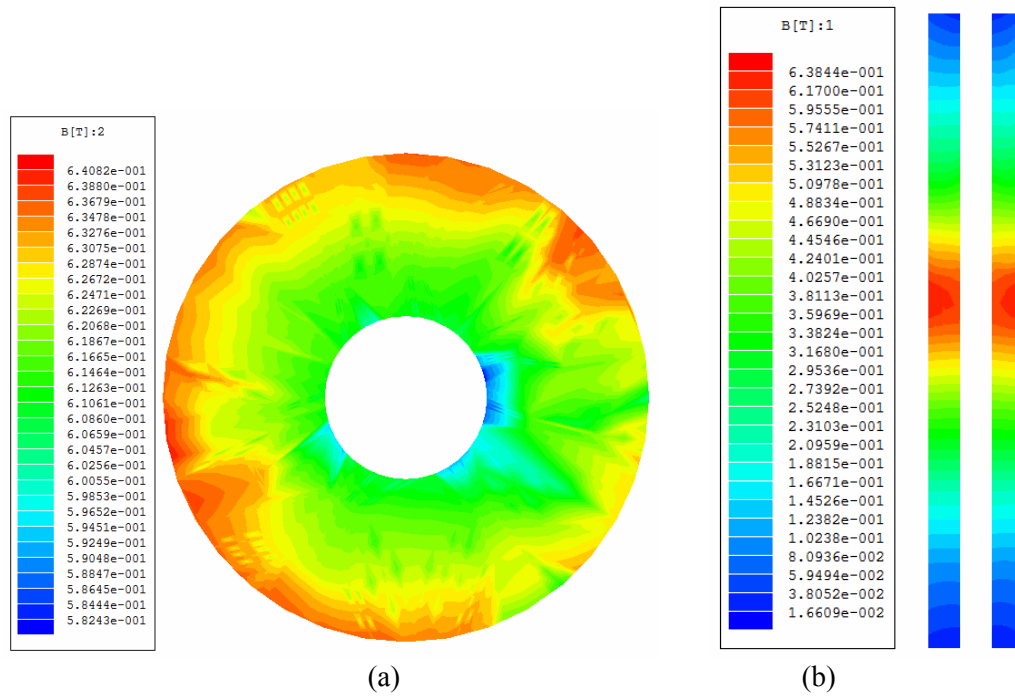


Fig. 2.10. Magnetic flux density distribution (a) in cross-section of the Terfenol-D rod (b) throughout the length of Terfenol-D rod.

As seen in Fig. 2.10, by employing this configuration we may reach the required amount of magnetization inside the Terfenol-D rod. However, lack of magnetic field concentration in the Terfenol-D rod is the main drawback that may cause two problems:

- Increased power consumption which could be disadvantageous.

- Decreased surface contact between the Terfenol-D rod and the squeezing tube would generate high stresses in the contact areas which will consequently induce high radial strains in the Terfenol-D rod and could lead to malfunction of the magnetostrictive linear motor.

### 2.3.1    Sensitivity Analysis

To see how the stator tube diameter increase would affect the magnetic flux density inside the active material, a sensitivity analysis was performed. In this analysis the outer diameter of stator tube was increased gradually and an FEA was done. The stator diameter was increased from 45 mm to 60 mm and the magnetic flux density distribution was calculated. As seen in Fig. 2.11, increasing the stator diameter by 20 mm will lead to around 15% drop in peak magnetic flux density in the Terfenol-D rod.

### 2.4 Tubular Configuration with Internal Coil

As shown in Figure 2-12, this configuration is the same as last one but here the coils are placed inside the hollow Terfneol-D rod and the rest of motor structure remains unchanged. Using this kind of configuration we may achieve the most compact design.
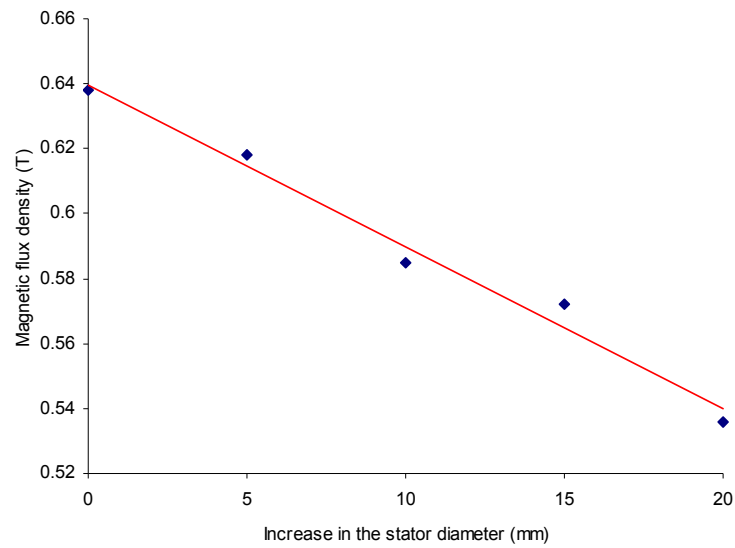
Fig. 2.11. Magnetic flux density inside the Terfenol-D rod versus increase in the stator diameter.
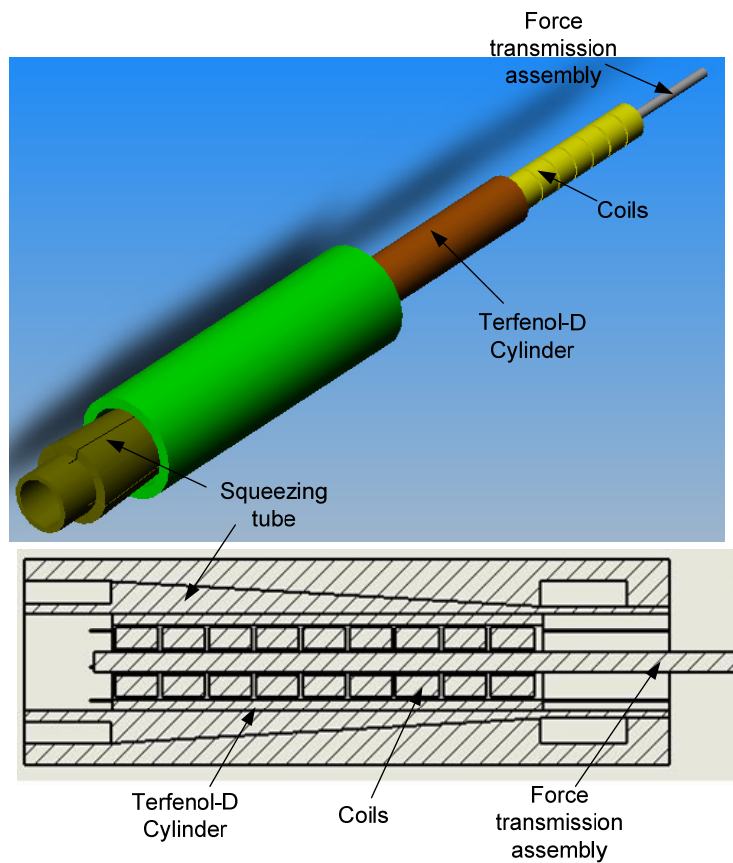


Fig. 2.12. Tubular configuration with internal coil.

For the sake of simplicity some details were omitted and the overall geometries of such a configuration as shown in Table 2.2 were used for FEA of the motor. In Fig. 2.13, magnetic flux density distribution through cross-section of the Terfenol-D rod is shown.

Table 2.2. General dimensions used for FEA in tubular configuration, internal coil.

| Component | Material | Electrical Properties | Geometry Specification |
|---|---|---|---|
| Shaft | Stainless Steel | $\mu_r = 1.0$ <br> $\sigma = 1.1 \times 10^6$ S/m | D = 9 mm <br> L = 200 mm |
| Active element | Terfenol-D | Nonlinear B-H curve specified in Fig. 2.9 | ID = 34 mm <br> OD = 45 mm <br> L = 200 mm |
| Stator tube | Brass | $\mu_r = 1.0$ <br> $\sigma = 1.5 \times 10^7$ S/m | ID = 45 mm <br> OD = 55 mm <br> L = 200 mm |
| Coil | Copper | $\mu_r = 0.9999$ <br> $\sigma = 5.8 \times 10^7$ S/m | ID = 12 mm <br> OD = 32 mm <br> L = 20 mm |
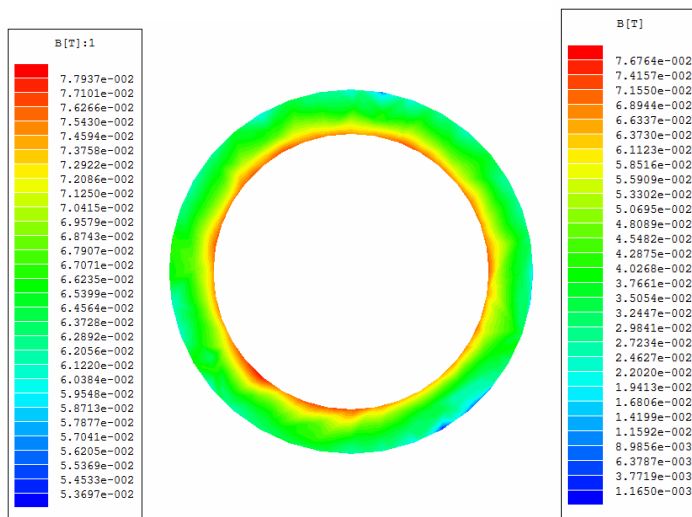


Fig. 2.13. (a) Magnetic flux density distribution through cross-section of the Terfenol-D rod (b) Magnetic flux density distribution inside the Terfenol-D rod.

As it is seen in Fig. 2.13, we could achieve concentrated magnetic field in tubular configuration with internal coil. However, the magnetic flux density would be quite low, which necessitates the consumption of much more power in the linear motor.

## 2.5 Tubular Configuration with Back Iron

To overcome the shortcomings of past two configurations, the tubular design with back iron could be considered. The squeezing mechanism would be the same as the past cases with this difference that here some slots have been considered inside the squeezing tube to accommodate the coils.
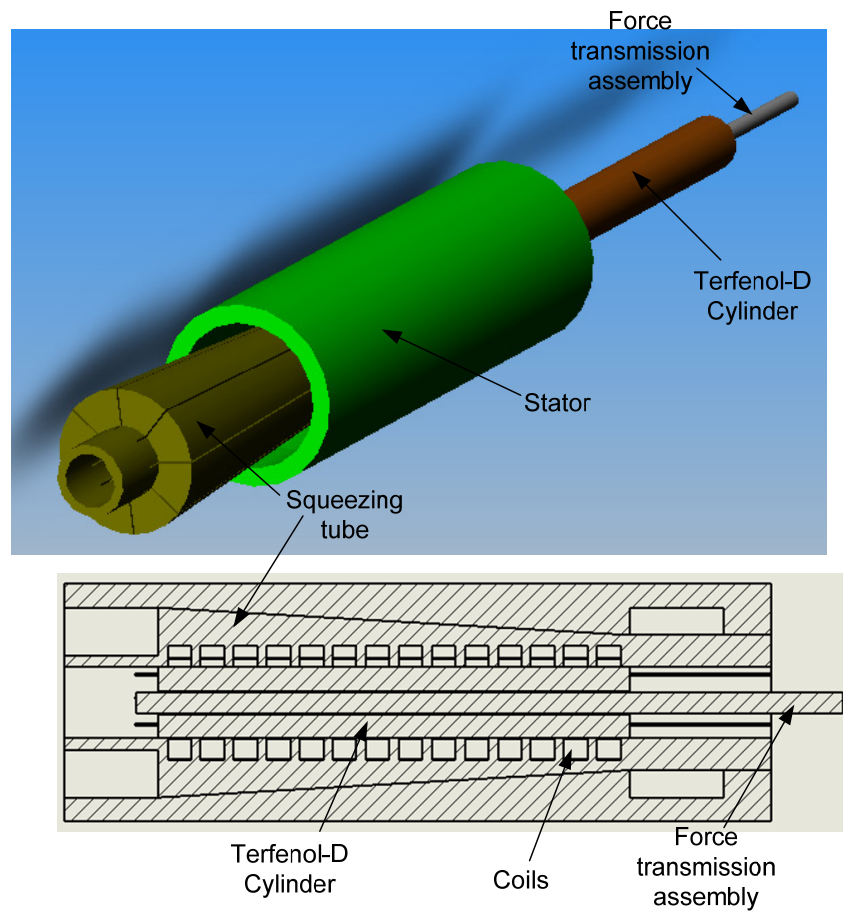


Fig. 2.14. Tubular configuration with back iron.

Due to the specific geometry of this actuator, its manufacture and assembly would be challenging which could make its production quite costly. The FEA of this motor was carried out using the overall dimensions of the motor as mentioned in Table 2.3. In Fig. 2.15, magnetic flux density inside the Terfenol-D rod is shown. It is seen that by using tubular configuration with back iron, we could theoretically overcome the magnetic field concentration problem. However, this would lead to an overwhelming complex geometry of the linear motor which would increase the manufacturing costs.

Table 2.3. General dimensions used for FEA in tubular configuration with back iron.

| Component | Material | Electrical Properties | Geometry Specification |
|---|---|---|---|
| Shaft | Stainless Steel | $\mu_r = 1.0$<br>$\sigma = 1.1 \times 10^6$ S/m | D = 9 mm<br>L = 200 mm |
| Active element | Terfenol-D | Nonlinear B-H curve specified in Fig. 2.9 | ID = 10 mm<br>OD = 30 mm<br>L = 200 mm |
| Stator tube | Iron | $\mu_r = 4000$<br>$\sigma = 1.03 \times 10^7$ S/m | ID = 30 mm<br>OD = 60 mm<br>L = 200 mm |
| Coil | Copper | $\mu_r = 0.9999$<br>$\sigma = 5.8 \times 10^7$ S/m | ID = 30 mm<br>OD = 45 mm<br>L = 7 mm |
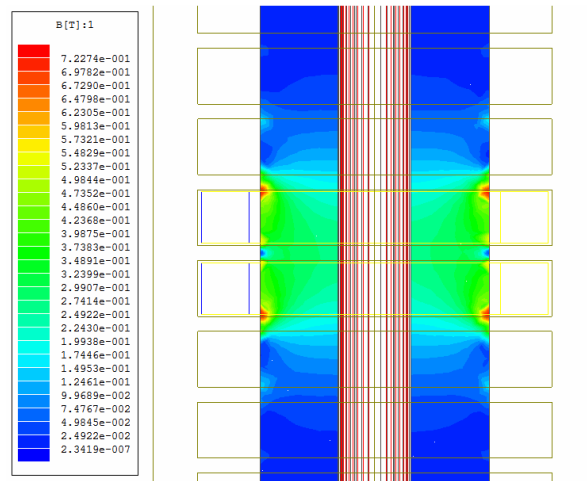


Fig. 2.15. Magnetic flux density distribution inside the Terfenol-D rod.

## 2.6 Flat Configuration, Two Sets of Coils

In this configuration, the Terfenol-D slab is sandwiched between a pair of wound stators (Fig. 2.16). Each stator has slots which should be wound manually. The stator can be manufactured using the iron laminations and then stacking them together. Production and assembly of this actuator is quite easy, and the main drawback is its extensive dimensions due to use of two sets of coils. The general features of the flat configuration with two sets of coils have been brought in Table 2.4.
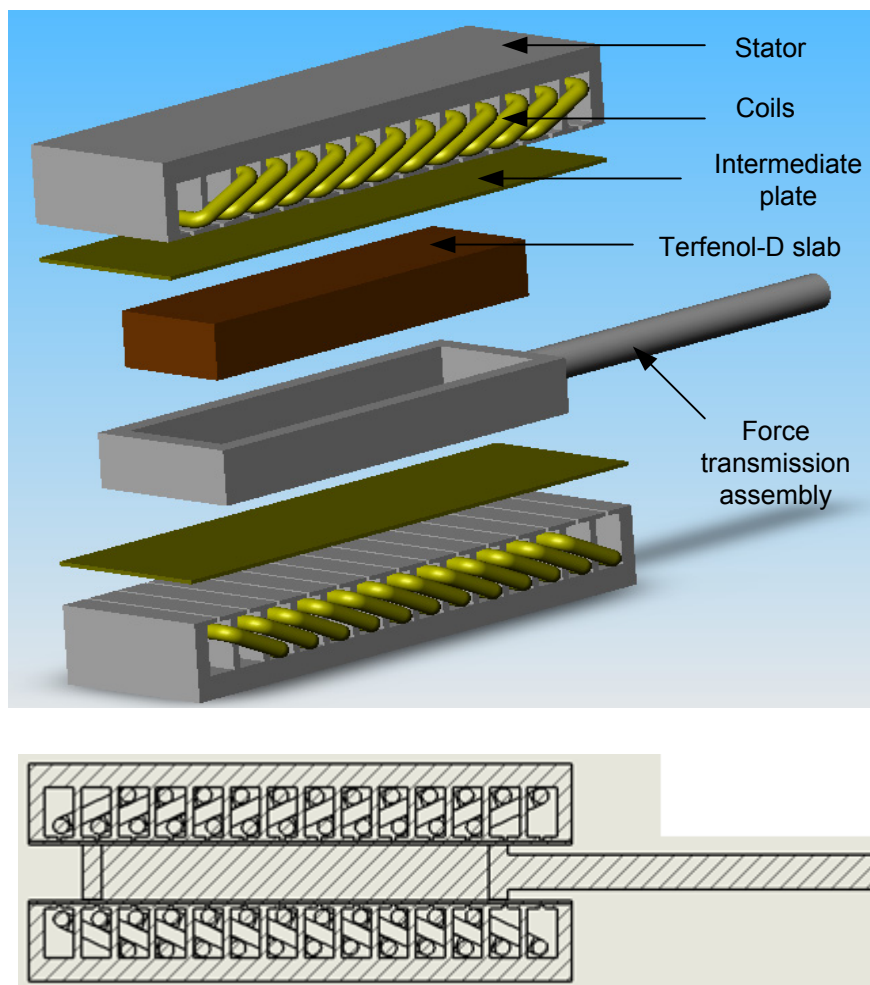


Fig. 2.16. Flat configuration with two sets of coils.

Table 2.4. General dimensions used for FEA in flat configuration with two sets of coils.

| Component | Material | Electrical Properties | Geometry Specification |
|---|---|---|---|
| Shaft | Stainless Steel | $\mu_r = 1.0$ <br> $\sigma = 1.1\times10^6$ S/m | D = 10 mm <br> L = 200 mm |
| Active element | Terfenol-D | Nonlinear B-H curve specified in Fig. 2.9 | Width = 28mm <br> Thickness = 14.3 mm <br> L = 200 mm |
| Stator | Iron | $\mu_r = 4000$ <br> $\sigma = 1.03\times10^7$ S/m | ID = 30 mm <br> OD = 60 mm <br> L = 200 mm |
| Coil | Copper | $\mu_r = 0.9999$ <br> $\sigma = 5.8\times10^7$ S/m | N = 120 turns <br> $i_A = 3$ A <br> $i_B = 1.5$ A |

In Fig. 2.17, the magnetic flux density distribution in cross-section of the Terfenol-D slab is shown. It is seen that in flat configuration with two sets of coils, we have a concentrated magnetic field, which leads to a low power consumption. As stated earlier due to use of two sets of coils, the actuator size will increase.
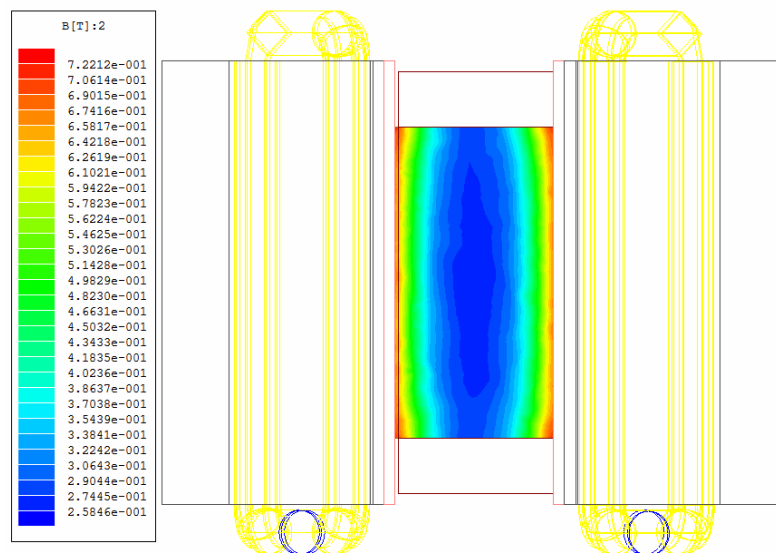


Fig. 2.17. Magnetic flux density distribution in cross-section of the Terfenol-D slab.

**2.7 Flat Configuration, Single Set of Coils**

In this configuration, the coils encircle the Terfenol-D slab and the stators should be of open-slot type to allow the pre-made coils put inside the slots. The manufacture and assembly of this linear motor is very easy. Since the slots are of open type, it could be constructed by a milling machine or lamination assembly. Since there is only one set of coils, this motor would be more compact in comparison with the last flat configuration. In Fig. 2.18, various parts of this configuration has been shown.
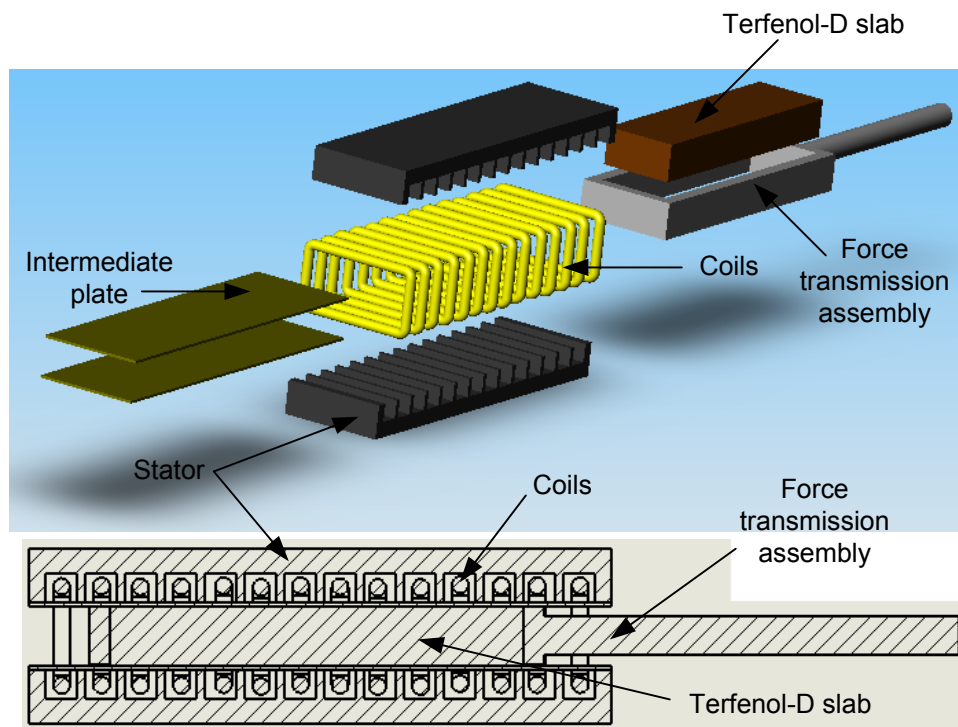


Fig. 2.18. Flat configuration with single set of coils.

The overall dimension of the motor is shown in Table 2.5. As seen in Figures 2.19, in flat configuration with single set of coils, we could still maintain the magnetic field

concentration with even higher intensity in comparison with the last case. Implementation of coils in a single set makes the size of the stator more compact.

Table 2.5. General dimensions used for FEA in flat configuration with single set of coils.

| Component | Material | Electrical Properties | Geometry Specification |
|---|---|---|---|
| Shaft | Stainless Steel | $\mu_r = 1.0$<br>$\sigma = 1.1\times10^6$ S/m | D = 10 mm |
| Active element | Terfenol-D | Nonlinear B-H curve specified in Fig. 2.9 | Width = 28mm<br>Thickness = 14.3 mm<br>L = 200 mm |
| Stator | Iron | $\mu_r = 4000$<br>$\sigma = 1.03\times10^7$ S/m | ID = 30 mm<br>OD = 60 mm<br>L = 200 mm |
| Coil | Copper | $\mu_r = 0.9999$<br>$\sigma = 5.8\times10^7$ S/m | N = 277 turns<br>i = 2.2 A |
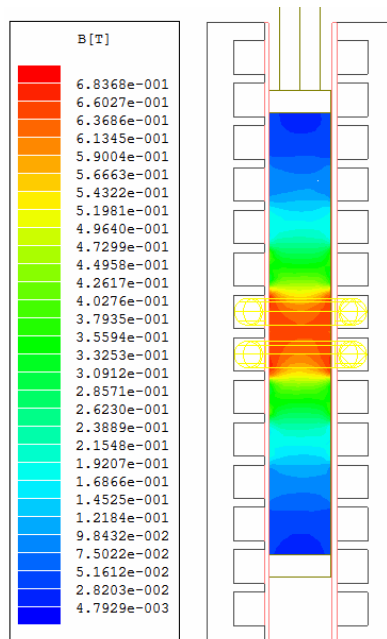


Fig. 2.19. Magnetic flux density distribution in the Terfenol-D slab.

**2.8 Conceptual Design Summary**

So far we reviewed various configurations for a linear magnetostrictive actuator. In Table 2.6 all different configurations and their pros and cons are summarized. These design configurations are compared by taking into account design considerations such as erogonomics, ease of manufacture, assembly, etc. In Table 2.7 summarizes the comparison results. In all three different tubular configurations, there is one thing in common, which is a wedge-based mechanism to deliver the squeezing force. Despite the possibility of generating ample friction force between the Terfenol-D rod and the squeezing tube, any defect in the manufacture of the motor could lead to an uneven distribution of radial force and the resulting stress distribution could not be controlled by adjusting a single-axial force which is applied using a compressed spring. On the other hand, in both flat configurations, the squeezing force could be applied in sufficient number of points to make sure that an even distribution of squeezing pressure is attainable in all sections of the Terfenol-D slab in a controllable manner.

Since the development of a successful prototype requires that we verify the impact of all different variables that play significant roles in generating the needed force, it is recommended to proceed the prototype development phase with implementing a magnetostrictive linear motor in flat configuration based on all aforementioned facts. This will allow us to establish the relations between different variables and verify the force-generating capability which is the ultimate objective of the project. Considering the similarities between the tubular and flat configurations, the research findings could be generalized to the tubular design after completion of the first phase of project under the condition that we have a fine solution to deliver an evenly distributed squeezing force.

Table 2.6. Pros and cons of design configurations.

| Configuration | Advantages | Disadvantages |
|---|---|---|
| **Tubular Configuration, External Coil, without Back Iron** | - Compact geometry<br><br>- Low number of components<br><br>- Easy assembly | - Lack of magnetic-field concentration<br><br>- Low surface contact<br><br>- High power consumption |
| **Tubular Configuration, External Coil, with Back Iron** | - Compact geometry<br><br>- Low number of components<br><br>- Concentrated magnetic field<br><br>- Low power consumption | - Complicated Geometry<br><br>- High manufacturing cost<br><br>- Assembly difficulties |
| **Tubular Configuration, Internal Coil** | - Compact geometry<br><br>- Low number of components<br><br>- Concentrated magnetic field | - Low magnetic flux density<br><br>- High power consumption |
| **Flat Configuration, Two Sets of Coils** | -Concentrated magnetic field<br><br>-Low power consumption<br><br>-Low manufacturing costs | - Large geometry<br><br>- Number of components |
| **Flat Configuration, Single Set of Coils** | - Compact geometry<br>- Concentrated magnetic field<br>- Low power consumption<br>- Low manufacturing costs | - Number of components |

Table 2.7. Comparison of design configurations.

| | Geometry | Ergonomics | Manufacturing | Assembly | Power Consumption | Magnetic Field Concentration |
|---|---|---|---|---|---|---|
| **Cylindrical Design, External Coil w/o back iron** | Good | Very Good | Fair | Excellent | Fair | Poor |
| **Cylindrical Design, External Coil with back iron** | Very Good | Good | Poor | Poor | Good | Excellent |
| **Cylindrical Design, Internal Coil** | Excellent | Excellent | Fair | Good | Poor | Good |
| **Flat Design, Single Set of Coils** | Good | Fair | Excellent | Very Good | Excellent | Very Good |
| **Flat Design, Double Sided Coils** | Poor | Poor | Very Good | Very Good | Very Good | Good |

# CHAPTER III

# ELECTROMAGNETIC DESIGN

In the previous chapter, several configurations for the linear magnetostrictive actuator were suggested, and a comparison between them was presented. Based on various parameters such as geometry, ergonomics, manufacturing, assembly, power consumption, and magnetic field concentration, the flat design with single set of coils was chosen. In this chapter the electromagnetic design for this configuration will be performed. First, the working principle of the linear magnetostrictive actuator will be discussed. It will be followed by design issues in magnetic circuit. Finally, actuator windings and power electronics will be discussed.

## 3.1 Working Principle

The working principle of the linear magnetostrictive actuator is illustrated in Fig. 3.1. The main idea is to generate a traveling magnetic field inside the active element while keeping it under pressure. The active element is initially at rest in a tight fit inside a channel. A magnetic field could be generated by the means of coils surrounding the active element. Two stators as shown are incorporated to enhance the magnetic flux density inside the active element. Now if we move this magnetic field to the right, as it comes to interaction with the active element, it makes that portion of active element elongate along the magnetic field lines. Since the volume of the active element is constant, this elongation will result in cross-sectional contraction of active element which releases the active element from its tight fit with the channel. As the magnetic field moves to the right, the neighboring portion of the active element expands while the last portion goes back to its original place and locks against

the channel. When the magnetic field has passed completely through the active element length, the active element has moved to the left. By repeating this process over and over, peristaltic motion is generated resulting in overall displacement of the active element.
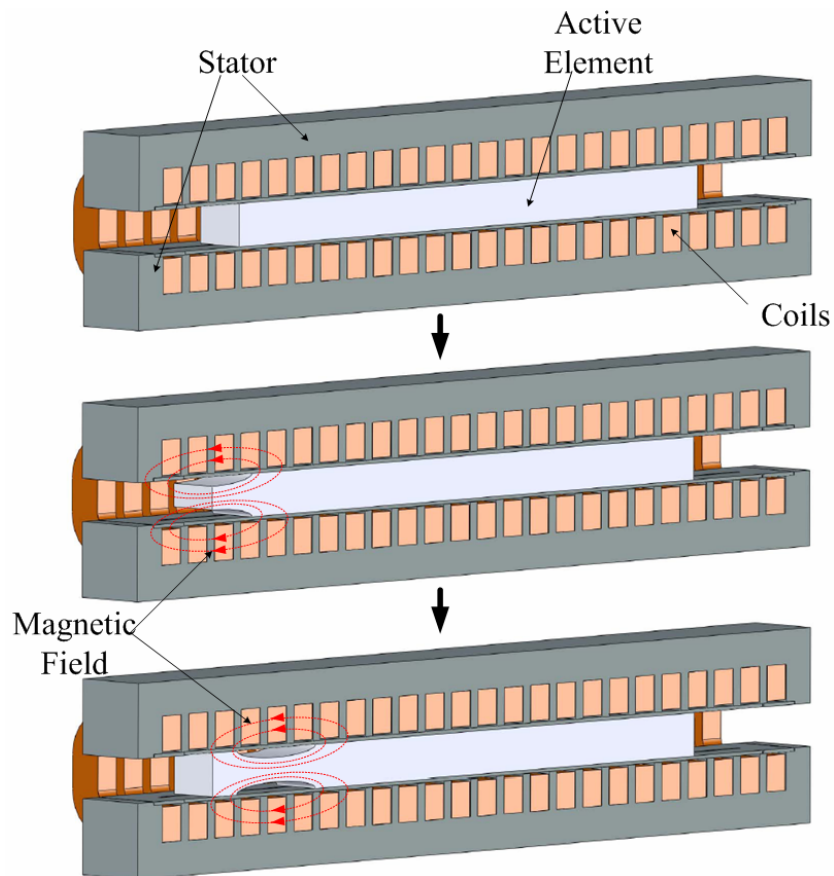


Fig. 3.1. Working principle of the linear magnetostrictive actuator. By generating a traveling magnetic field through the active element, peristaltic motion is generated which results in overall displacement of the active element in the opposite direction of the traveling magnetic field [20].

The magnetostrictive strain has a direct impact on the speed and force capacity of the linear magnetostrictive actuator. Hence, the main issue of the magnetic circuit design is to direct the magnetic flux as much as possible through the active element. By doing this, we would be able to lower the power requirements as well as to increase the force capacity. The

main objective of the power electronics is to generate the required traveling magnetic field by directing the specified currents to coils.

## 3.2 Magnetic Circuit Design

### 3.2.1 Terfenol-D Slab

The Terfenol-D slab experiences strains from two distinct sources in the direction of motion. One is the magnetic-field-induced strain and the other is mechanical strain which acts against the former. Their interaction determines the speed of the motor. To insure the proper operation of the motor we consider the magnetic-field-induced strain to be three times mechanical strain:

$$\varepsilon_{mag} = 3\varepsilon_{mech} \ .$$

In the preliminary design it was observed that the magnetic flux density of magnitude 0.67 T is obtainable in the cross-section of the Terfenol-D slab. Using the magnetostriction curves, this amount of magnetic flux density would result in 1000-ppm strain. Now using the above relation, the cross-sectional area of Terfenol-D slab will be calculated as

$$1000 \times 10^{-6} = 3 \times \frac{F}{EA} = 3 \times \frac{4000}{30 \times 10^{9} \times A} \ \Rightarrow A = 400 \text{ mm}^2$$

To analyze the impact of the Terfenol-D slab thickness on the magnetic flux density inside the active material, the FEA was run for different thicknesses of the active element while the cross-sectional area was kept constant. As seen in Fig. 3.2, from magnetic design point of view, using a thinner active material will result in an even higher magnetic flux density. However, the thickness of the active material determines the distance between two stators which has to be used to accommodate the force transmission assembly as well as the

Terfenol-D slab. So the limiting factor in decreasing the Terfenol-D slab thickness would be the minimum required space for the force transmission assembly.

As it will be seen in following chapter, the thickness of force transmission assembly will be 11 mm. Hence, the thickness of the Terfneol-D slab was chosen as 12.7 mm to have a clearance between the force transmission assembly and the stationary parts such as the inconel plate which will be discussed soon. Considering the magnetostrictive strains on the order of hundredths to tenths of millimeter, in magnetostrictive devices the Terfenol-D slab surfaces should be as smooth as possible to avoid the malfunction of the linear magnetostrictive actuator. Manufacture of Terfenol-D slab was contracted to Etrema Inc., and a surface roughness of 6 μm was achieved. Due to the crystalline nature of Terfenol-D, obtaining better figures for surface roughness is impossible with the current technology.



(a)                        (b)
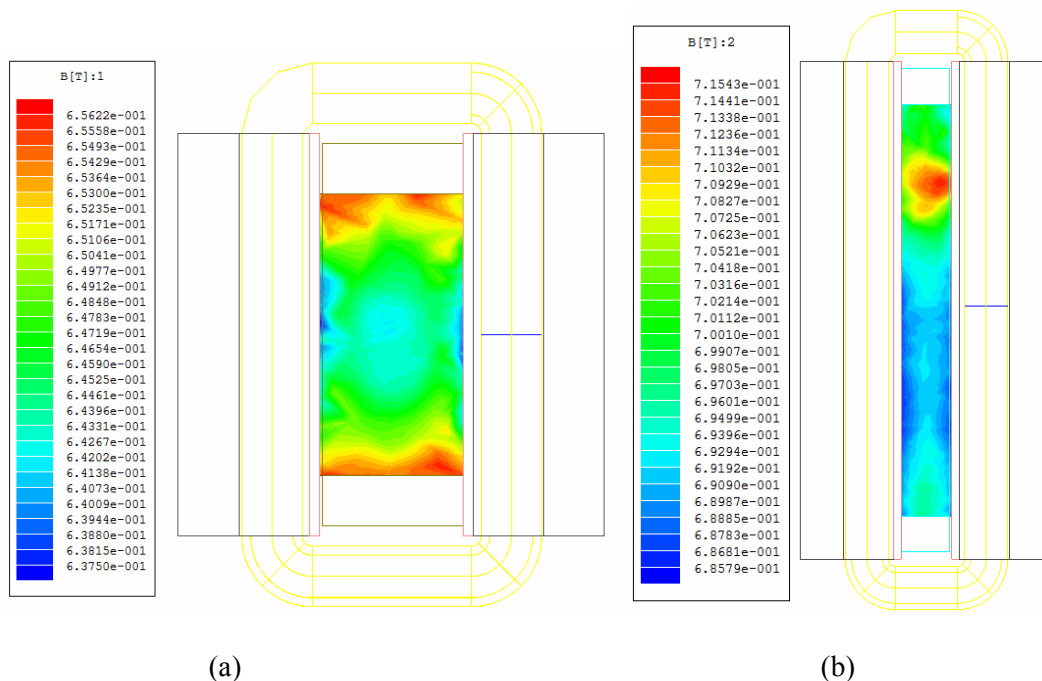
Fig. 3.2. Magnetic flux density in Terfenol-D slab with (a) Terfenol-D cross section of 28 mm × 14.3 mm and (b) the Terfenol-D cross-section of 57 mm × 7 mm under the same excitation conditions.

The dimensions of the Terfenol-D slab are illustrated in Fig. 3.3. A photograph of the Terfenol-D slab is shown in Fig. 3.4.
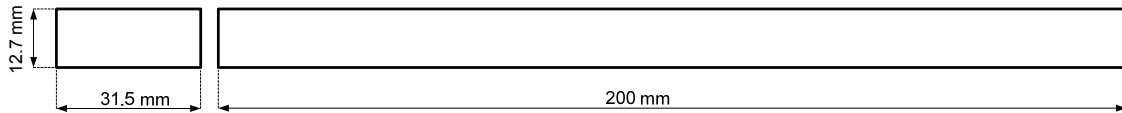


Fig. 3.3. Terfenol-D slab dimensions.
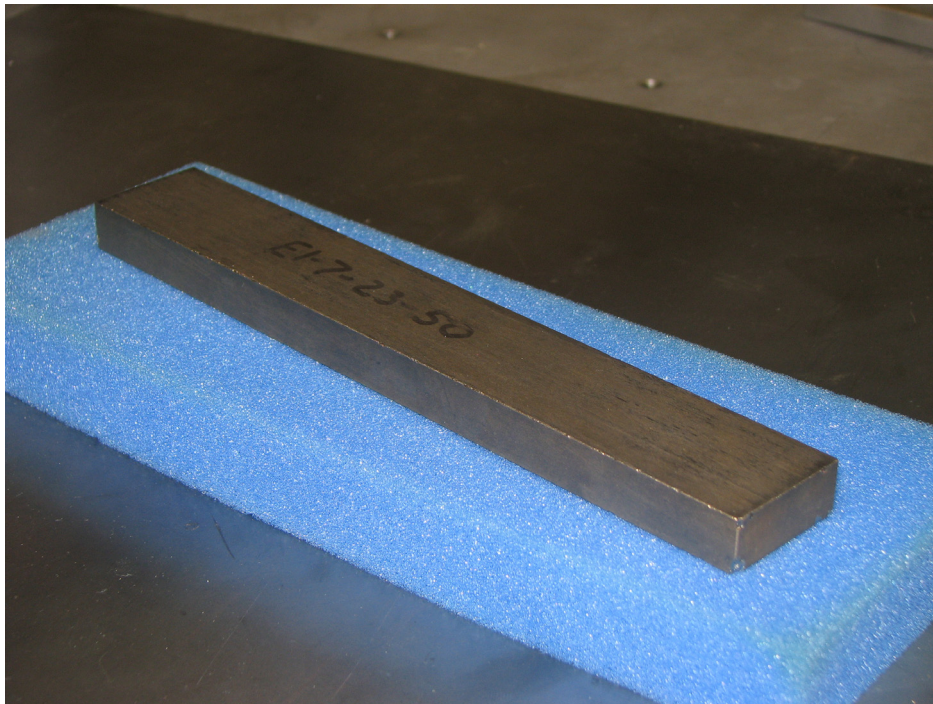


Fig. 3.4. Terfenol-D slab.

### 3.2.2  Stator

The magnetostrictive strain has a direct impact on the speed and force capacity of the linear magnetostrictive actuator. Hence, the main issue of the magnetic circuit design is to

direct the magnetic flux as much as possible through the active element. By doing this we will be able to lower the power requirements as well as to increase the force capacity. In our design, back iron is employed, and the stator material has a direct impact on the performance of the actuator. In the preliminary design, the stator material was assumed to be linear with a relative permeability of 4000.

Here the nonlinear B-H curves of different alloys are employed, and their impact on Terfenol-D magnetization is observed. Based on the market availability, the nonlinear magnetic properties of the following three alloys were considered and the FEA was performed:

- Cold rolled lamination steel (LTV type 7, 50 Hz)

- Nickel-Iron Alloy 49, 60 Hz

- Nickel-Iron Alloy HyMu 80, 60 Hz

In Figs. 3.5−3.7 the magnetic flux density distributions inside the Terfenol-D slab is shown for the abovementioned stator materials.

It is seen that the peak magnetic flux density is slightly less than when we use the linear B-H curve for the stator. Besides, it is observed that using the high-permeability materials like Nickel-Iron Alloys will not contribute to the higher magnetic flux density inside the Terfenol-D slab. For instance an unnoticeable increase in magnetic flux density is seen and taking into account the high prices of Nickel-Iron Alloys in comparison with Cold Rolled Motor Lamination Steel (CRML), it is reasonable to choose CRML as the stator material.

The eddy-current analysis was also carried out for a three-phase excitation case with frequencies as low as 0.1 Hz up to 60 Hz. The eddy-current analysis in Maxwell software only allows linear materials. Hence, iron with relative permeability of 4000 was considered

as the stator material. After performing FEA, the core losses were evaluated by integrating the ohmic losses over the volume of stator and Tefenol-D slab. The core losses due to eddy current have been listed in Table 3.1.

Table 3.1. Core losses in different excitation frequencies.

| Frequency (Hz) | Core Losses (W) | |
|---|---|---|
| | Stator | Terfenol |
| 0.1 | $1.636 \times 10^{-5}$ | $2.6 \times 10^{-6}$ |
| 5 | 0.022 | 0.0067 |
| 10 | 0.066 | 0.026 |
| 20 | 0.194 | 0.096 |
| 30 | 0.318 | 0.2 |
| 60 | 0.44 | 0.71 |
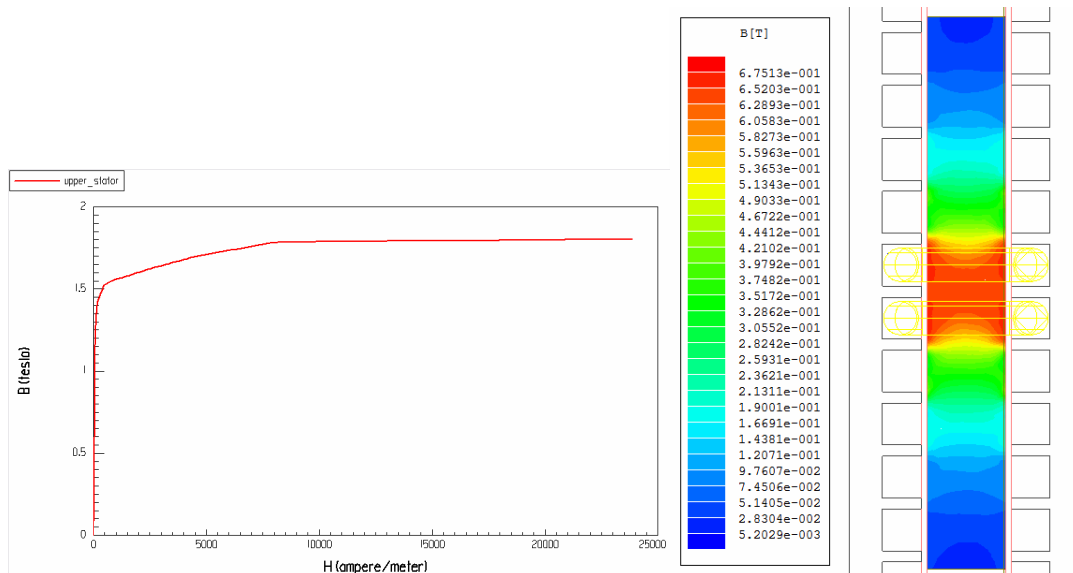


Fig. 3.5. The nonlinear B-H curve of cold rolled lamination steel and (b) the distribution of the magnetic flux density in the Terfenol-D slab.
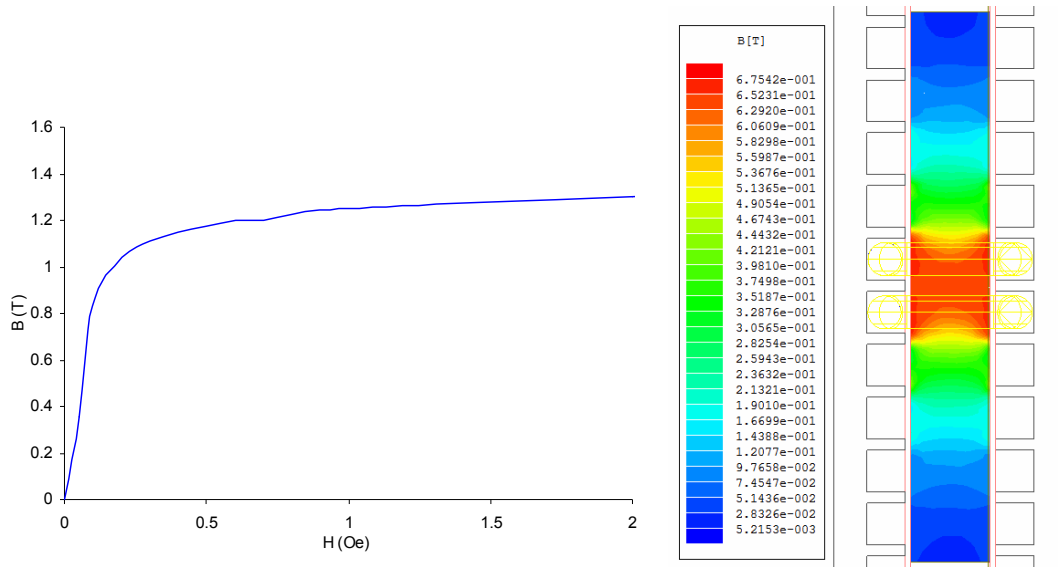
Fig. 3.6. The nonlinear B-H curve of Nickel-Iron Alloy 49 and the distribution of the magnetic flux density.
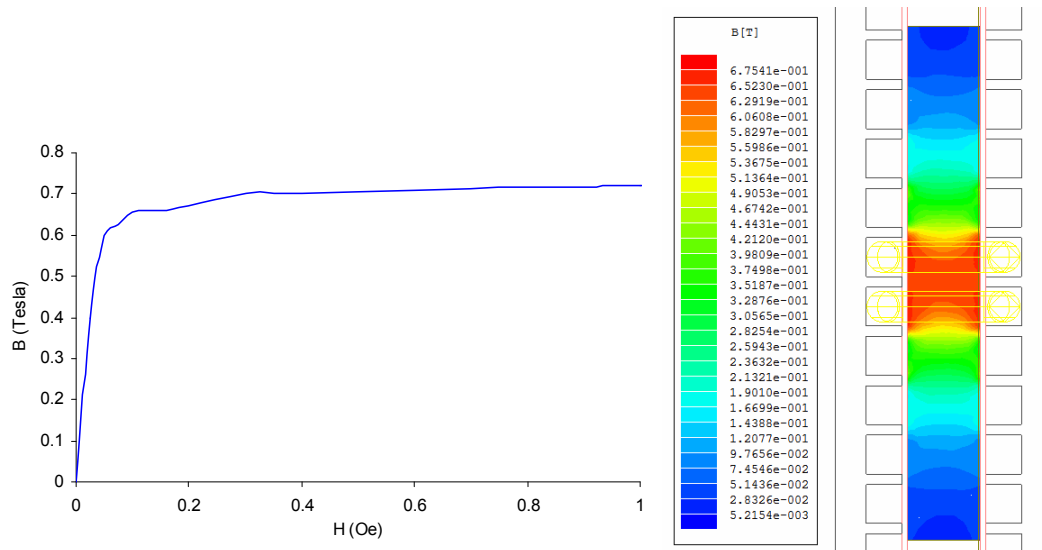


Fig. 3.7. The nonlinear B-H curve of Nickel-Iron Alloy Hymu 80 and the distribution of the magnetic flux density in the Terfenol-D slab.

We consider three different methods for manufacturing the stators here.

**Laminated Stators**

The conventional manufacturing method for the stators is to cut the stator laminations by using laser cut or press die and then assemble them to a stack of laminations. One typical problem found in linear applications is the ability to produce a flat stack and the laminations tend to bow depending on the size and exact geometry. Since none of manufactures were able to guarantee the level of flatness they may deliver, and on the other hand the flatness of the stator plays a crucial role in the actuator performance, I decided to consider other options for manufacture of the stators.

**Composite Stators**

Another method is to produce the stators from magnetic composites. Nevertheless, this method needs additional tools such as press dies which makes it uneconomical.

**Machined Stators**

Finally the last method I considered was to machine the stator out of a solid bar. Considering the open-slot geometry of the stator in our design, the machining process is straightforward. Besides, this method allows creating tapped holes in the stator body without the risk of damaging the stator.

Due to the low core losses in the actuator, the need for laminated stators could be potentially eliminated. Hence, considering the benefits of machining method over other manufacturing methods, I decided to machine the stators out of solid bar. Among, three different stator materials we considered earlier in this chapter,  the Nickel-Iron 49 alloy bars

were only available in the market. We purchased two solid bars of Nickel-Iron alloy 49 from Ed Fagan Inc. [21]. The detailed design and machining process of the stators are described in the next chapter.

## 3.3 Winding Structure

From the FEA in the preliminary design, it is known that we have to flow an overall current of 600 A-turns in each of three adjacent coils to generate around 0.6-T magnetic flux density inside the Terfenol-D slab. In order to At first we intended to use AWG#27 but due to the high costs of winding the coils, the AWG#24 was opted. Using this wire size we have 273 turns in each coil. Due to the open-slot geometry of the stators, it is possible to use prefabricated coils. The required tools were manufactured and the coils were wound by WireWinders [22]. The wire arrangement in the coil is shown in Fig. 3.8.
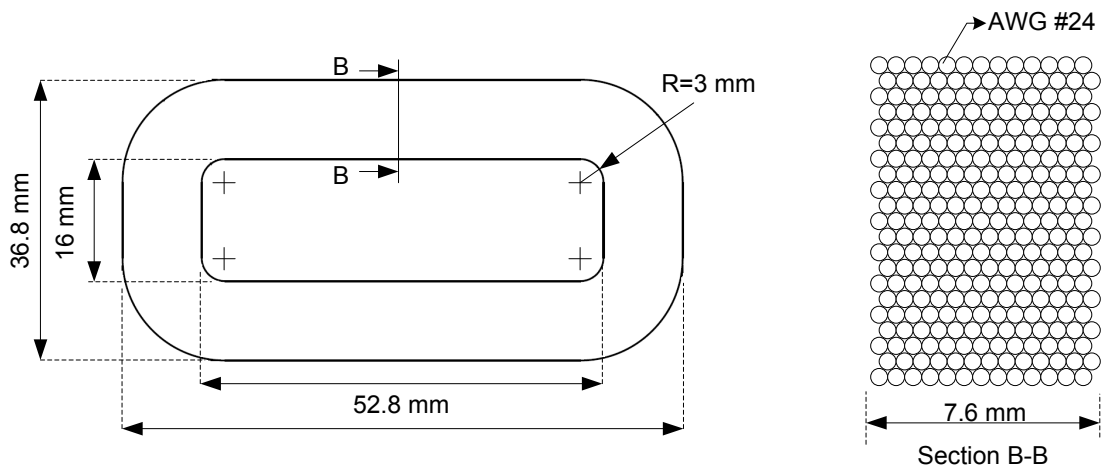


Fig. 3.8. wire arrangement in the coil.

Then the length of wire in each coil is around 47.5 m. According to the American wire gauge (AWG) standard, the resistance of this length of wire would be 4 Ω, and our measurements using RCL meter showed that the resistance and the inductance of each coil will be 4.28 Ω and 9.7 mH, respectively.

## 3.4  Power Electronics

As mentioned earlier, the proposed design enables us to operate the linear magnetostrictive actuator in various configurations including three-phase conventional operation and local multi-phase operation. Here, we focus on the local three-phase operation. The objective of power electronics here is to direct the required current to three adjacent coils and then move it to either side depending on the motor's motion direction. The coil arrangement and the local three-phase excitation sequence are shown in Fig. 3.9.
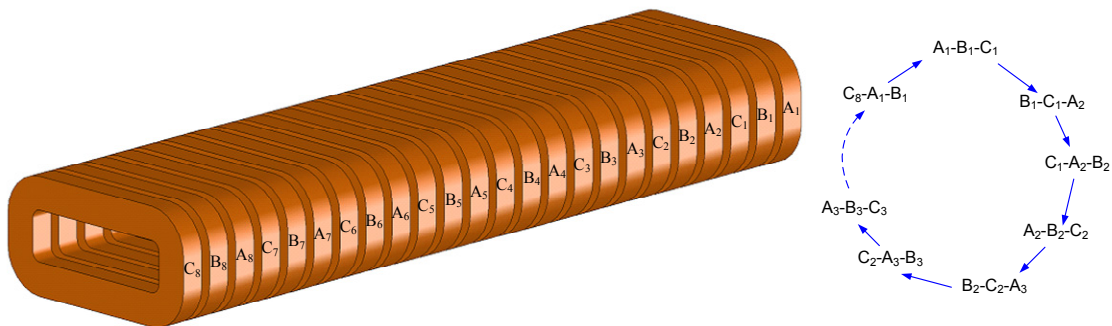


Fig. 3.9. Coil arrangement and excitation sequence in linear magnetostrictive actuator.

### 3.4.1  Power MOSFET

MOSFET is a type of field-effect transistor (FET) with three terminals, drain (D), source (S), and gate (G) which is controlled by gate voltage. A MOSFET uses a metal plate

as the gate terminal and it is insulated from the p- or n-type silicon substrate by a thin layer of oxide (see Fig. 3.10). By applying gate voltage $V_G$ to the gate plate, an electrostatic field induces reverse charges at the gate and the substrate. The charges at the substrate initiate transistor type characteristics by forming either an n-type channel or a p-type channel [7].
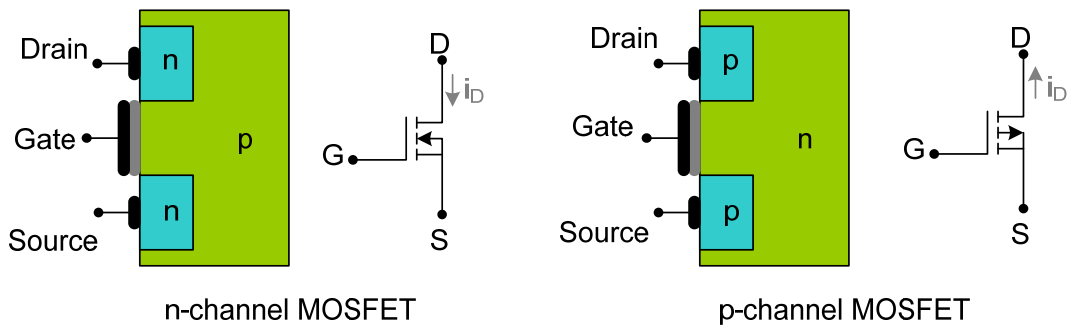


Fig. 3.10 Metal-oxide-semiconductor (MOS) field effect transistor (FET).
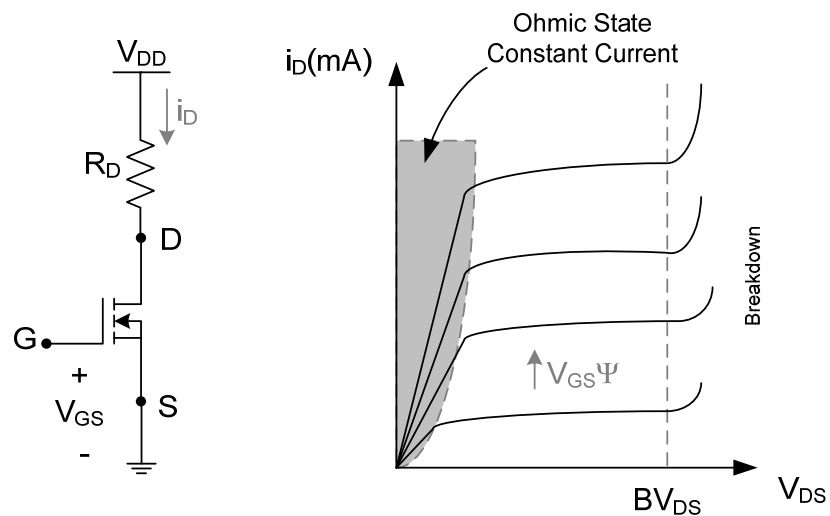


Fig. 3.11. Enhancement mode MOSFET characteristic.

For most of power amplification and modulation applications, MOSFETs are operated in the enhancement mode. The characteristic of enhancement mode is shown in Fig. 3.11. and three regions could be detected as below [7]:

a) Cutoff: When the voltage across the gate and the source, $V_{GS}$ is less than the threshold voltage, $V_T$, the MOSFET is in the cutoff region and there is negligible current flow through the drain (D) terminal, i.e.,

$$\begin{cases} V_{GS} < V_T \\ i_G = 0 \end{cases} \Rightarrow \begin{cases} i_D \approx 0 \\ V_{DS} \approx V_{DD} \end{cases}$$

where, typically, $V_T \approx$ 1–2 V.

b) Active Region: When the $V_{GS} > V_T$, the MOSFET is in the active region, where

$$V_{GS} > V_T \text{ and } \begin{cases} i_D \propto (V_{GS} - V_T)^2 \\ V_{DS} > V_{GS} - V_T \end{cases}$$

In this mode, the transistor works like a voltage-controlled current amplifier, where the drain current $i_D$ is proportional to square of the difference between the gate-source voltage and the threshold voltage. The drain current is controlled by the gate-source voltage $V_{GS}$.

c) Ohmic State: When $V_{GS}$ is large enough, the MOSFET is in saturation where

$$V_{GS} \gg V_T \text{ and } \begin{cases} i_D = V_{DD}/R_D \\ V_{DS} \approx i_D.R_{ON} \end{cases}$$

In this mode, the transistor can be viewed as a closed switch between the terminals D and S with a voltage controlled resistance $R_{ON}$.

The transistor can be operated as a voltage-controlled switch by controlling the gate voltage of MOSFET as seen in Fig. 3.12. That operates between the cutoff (point A) and the Ohmic (point B) region. Large input impedance of MOSFET in comparison with BJT, simplifies the driver circuit because the gate current is negligible. This also implies that a

MOSFET is much more efficient than BJTs and it can be operated at much higher switching frequencies (20 to 200 kHz). Power MOSFETs can carry drain currents up to several hundreds of amperes and $V_{DS}$ up to around 500 V. Field effect is one of the key reasons why MOSFET has better switching performance than BJT. However, static field is also one of its main failure modes. MOSFETs are very sensitive to static voltage. Since the oxide insulating the gate and the substrate is only a thin film (in the order of a fraction to a few micrometer), high static voltage can easily break down the oxide insulation. A typical gate breakdown voltage is about 50 V. Therefore, static electricity control or insulation is very important when handling MOSFET devices.
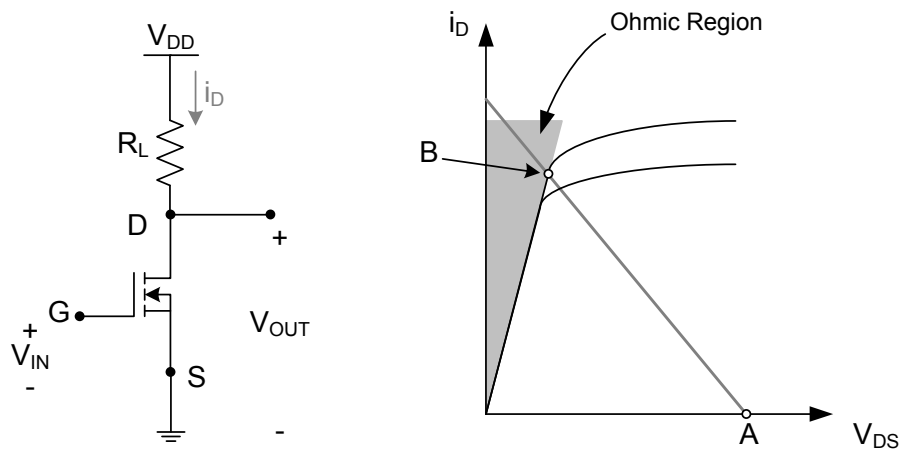


Fig. 3.12. MOSFET as a voltage controlled switch.

In order to direct the current to three adjacent coils in the linear magnetostrictive actuator, we decided to use MOSFETs as voltage-controlled switches. The switching boards are discussed below.

**3.4.2    Switching Boards**

As shown in Fig. 3.9, in local three-phase excitation, we have to direct the required current to three adjacent coils and then move it to either side depending on the motor's motion direction. To achieve this goal we designed and implemented three switching boards (Fig. 3.13), each including eight power MOSFETs (model IRF3315Pbf by International Rectifier), eight MOSFET drivers (model TC4420 by Microchip), eight flyback diodes (model MUR405 by ON Semiconductor), three inverters and one 3-line-to-8-line decoder. There is a dedicated power supply (model E3644A by Agilent) for each phase which also monitors its voltage and current. A schematic diagram of different layers of the electronic system including the digital circuit and power electronics for a single phase is shown in Fig. 3.14. The switching frequency of the Power MOSFETs is controlled using the digital inputs/outputs (I/Os) of a digital-signal-processing (DSP) board (model DS1104 by dSPACE).

**3.5  Instrumentation Structure**

Key components of this mechatronic system are shown in Fig. 3.15. The whole system is controlled by a PC which is interfaced with the hardware using a digital-signal-processing board (DSP). The switching frequency of the Power MOSFETs are controlled by digital I/Os of DSP board which makes the actuator move in the required direction. A laser sensor is employed to monitor the position of the actuator. It provides a voltage which is sent to the A/D channels of DSP board and then can be read in the software and the corrective action is taken. Different components of the instrumentation structure will be discussed here.
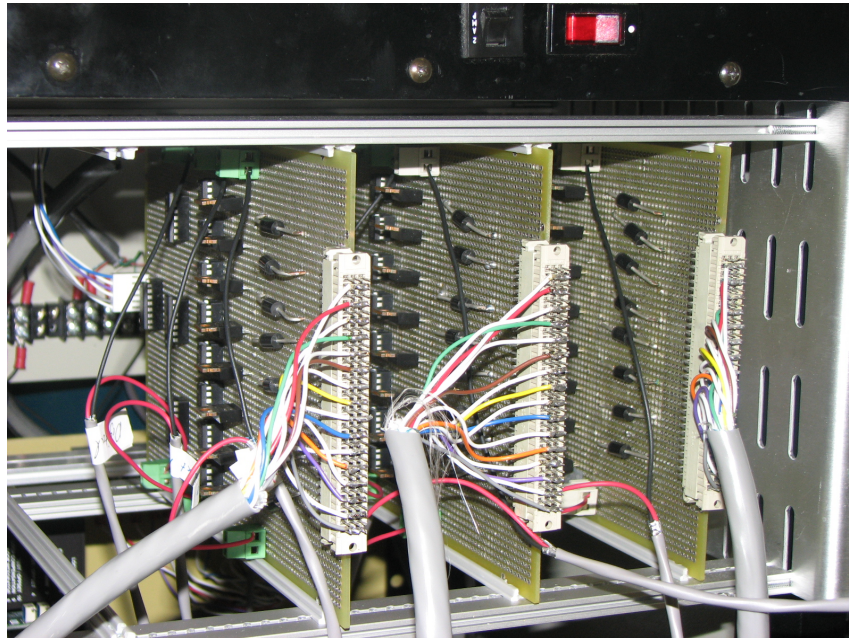
Fig. 3.13.  Switching boards [23].
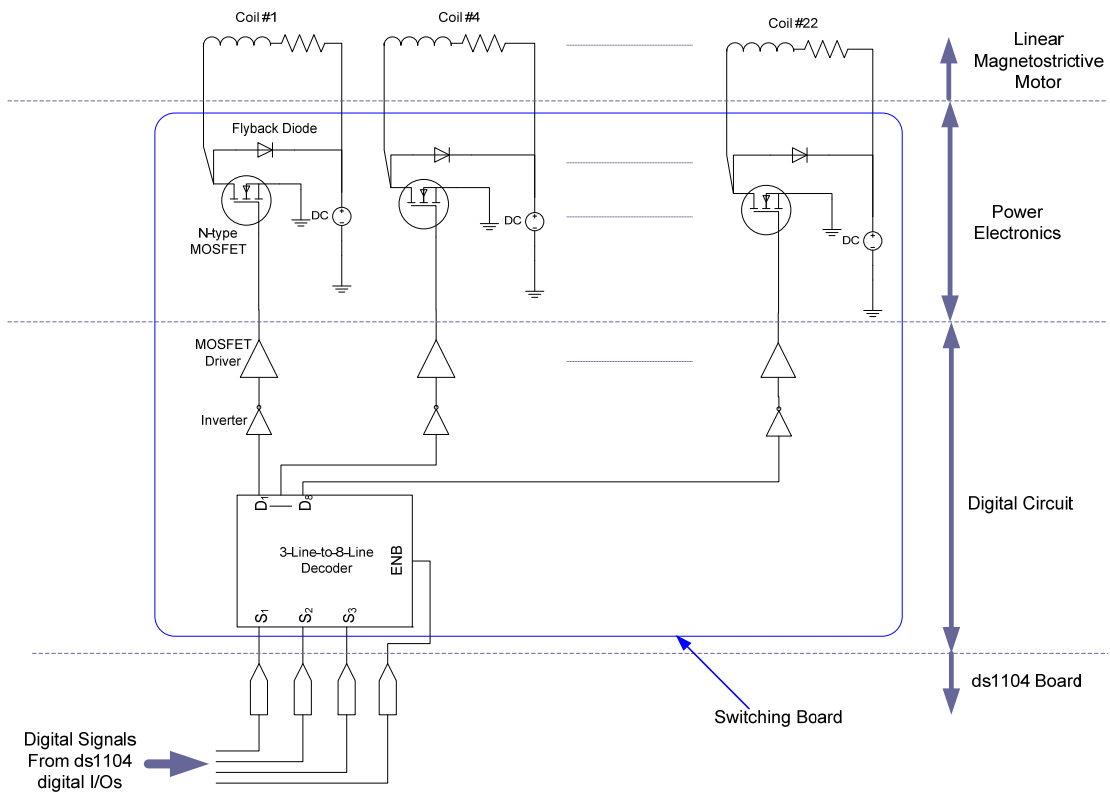

Fig. 3.14.  Schematic diagram of digital circuit and power electronics for a single phase [20].
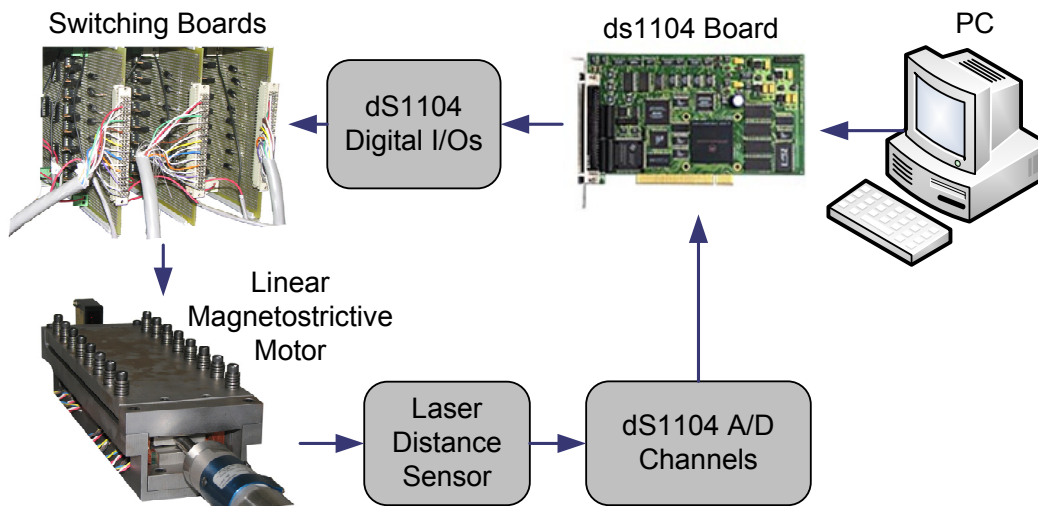
Fig. 3.15. Different components of the mechatronic system [20].

### 3.5.1 DS1104 Board

To implement the real-time control, the dSPACE DS1104 DSP board [24] was used (Fig. 3.16). This DSP board is a 32-bit 250-MHz floating point DSP, with eight analog-to-digital (A/D) channels, eight digital-to-analog (D/A) channels, and twenty digital I/O channels.

### 3.5.2 Software

As it will be seen later, the control system monitors the position, implements the relay controller, produces switching sequences for switching boards, and performs current monitoring and sensorless control. It is designed in Simulink® and then the model code be generated using Real-Time Workshop®. Hence, the real-time model could be automatically compiled and downloaded to the DSP board which minimizes the implementation time.

The user interface was designed and implemented using ControlDesk which is the experiment software that provides an environment in which the user could monitor different signals and issue the required control commands. The user interface environment is shown if Fig. 3.17. Here, The actuator can be controlled manually by user or automatically through this interface. Besides, the closed-loop control can be performed using the laser sensor or the position estimation algorithm. All different system variables such as position, coil currents, and errors can be plotted in this interface and saved as a MATLAB figure for further processing.

The Simulink® block diagrams are presented in Appendix B.
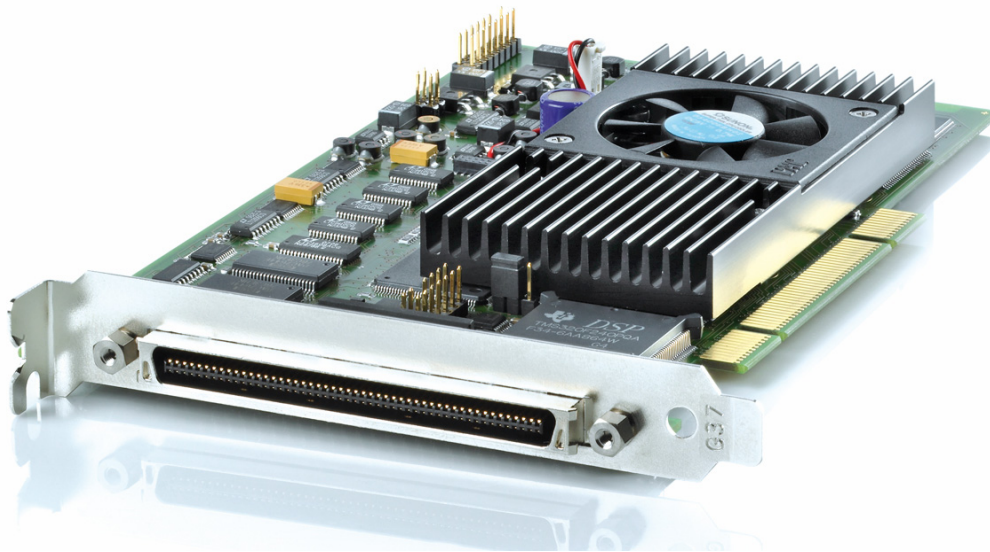


Fig. 3.16. dS1104 R&D board [24].
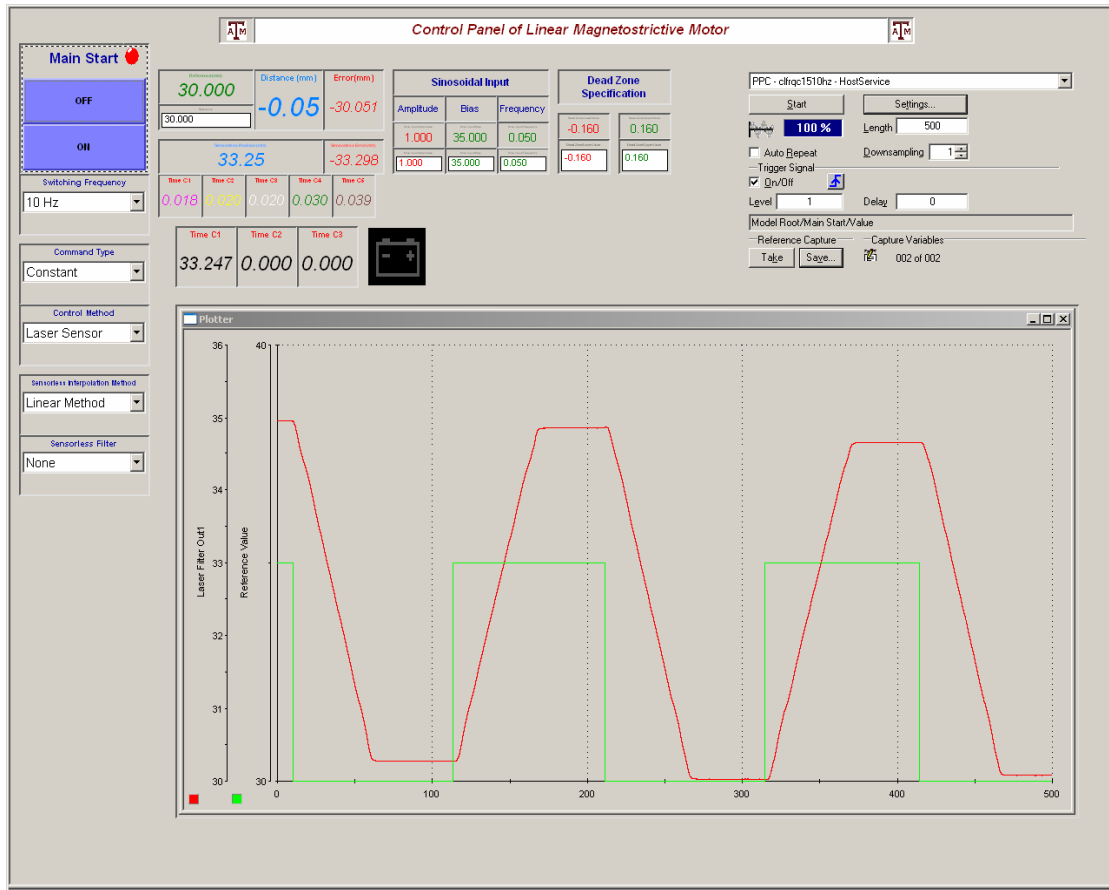
Fig. 3.17. User interface control panel.

### 3.5.3 Sensors

The motor shaft position is monitored with a laser distance sensor (model OADM 20I6460/S14F by Baumer Electric [25]) which has a resolution of 5 μm and measuring distance range from 30 mm to 130 mm (Fig. 3.18). The voltage supply is 12 V and the output voltage varies between 0 and 10 VDC. The output voltage is sent to A/D channel of DSP board and is displayed in user interface control panel. Laser sensor connection diagram is shown in Fig. 3.19. The load could also be monitored using a load cell (LCB400 by Futek [26]).

Fig. 3.18. Laser distance sensor [25].



Fig. 3.19. Laser sensor connection diagram [25].

CHAPTER IV

MECHANICAL DESIGN AND ASSEMBLY

One feature which distinguishes this type of linear magnetostrictive actuator with the conventional actuators is that it is subjected to a normal squeezing force as well as the external load. Hence, different components of the linear magnetostrictive actuator should be designed so that they could stand these two loads with minimum deflection. On the other hand, in magnetostrictive devices, the resulting strains are on the order of hundredths to tenths of millimeters. Therefore special attention must be paid tolerances in the construction. There is a need to manufacture or machine the magnetostrictive transmission parts with a tolerance level within couple or tens of micrometers to achieve performance. It is also important that all surfaces that transmit force and strain are flat and smooth. The smoothness requirement is normally within a couple of micrometers [27]. In this chapter, the detailed description of the mechanical design, fabrication, and assembly issues are presented.

**4.1 Force Transmission Assembly**

The induced magnetic strain and force would be transmitted to the load using the force transmission assembly (Fig. 4.1). Since Terfenol-D is very weak in tension, the transmission assembly has been designed to keep the Terfenol-D slab under compression. The spring washers shown in Fig. 4.1 maintain the contact between the pillow pieces and the Terfenol-D slab. These pillow pieces could slide on the force transmission shaft and spring rod.
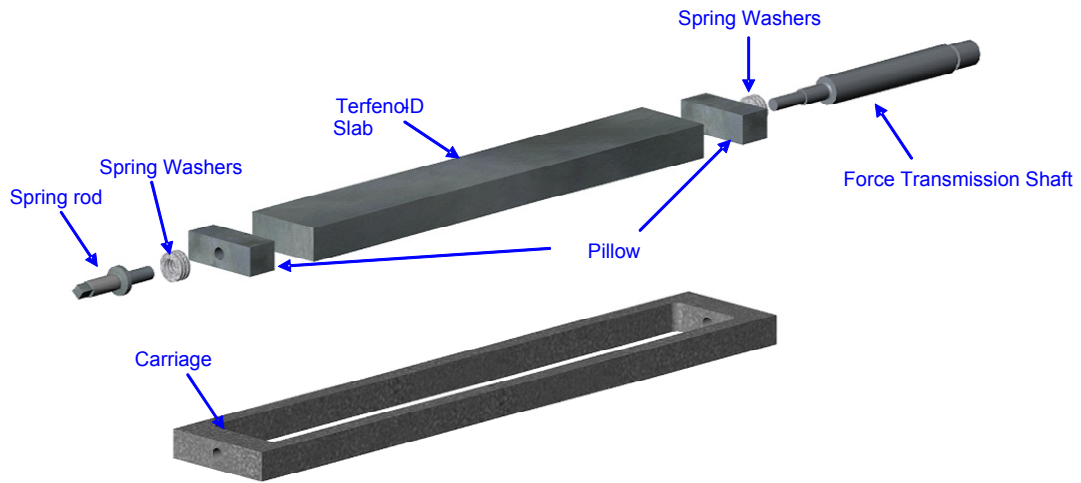
Fig. 4.1. Force-transmission assembly.

The generated force by the Terfenol-D slab would be transmitted to the output shaft through the carriage (Fig. 4.2) which encircles the slab.
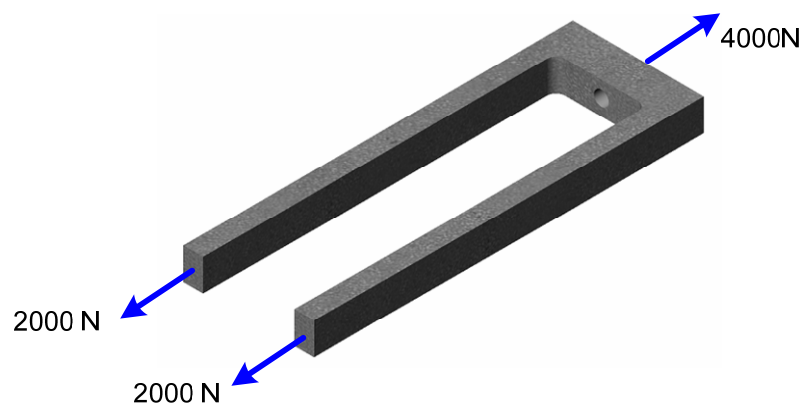


Fig. 4.2 Carriage cross-section.

To direct as much magnetic flux as possible through the Terfenol-D slab, the carriage should be made out of a non-magnetic metal. In this regard, stainless-steel grade 303 was chosen which has a yield strength of 240 MPa. Considering the maximum generated force by motor as 4000 N, and a safety factor of 2, the cross-sectional area of the carriage would be computed as

$$\sigma = \frac{F}{A} \Rightarrow 240 \times 10^6 = \frac{2 \times 2000}{A} \Rightarrow A \approx 17 \text{ mm}^2 \tag{4.1}$$

The 4000-N generated force will be transmitted to the output shaft which should be screwed into the tapped hole created in the carriage. Considering a thread length of engagement equal to 12.7 mm for the threads, the shear area of the thread would be 98 mm$^2$ which results in shear strength of the thread equal to a 23.5-kN axial force for the ¼-20 UNC 2B thread size with a safety factor of 6. The drawing of this carriage with dimensions and tolerances is shown in Fig. A.4.

The total blocking force supported by the actuator would be 4000 N which is transmitted through the force-transmission shaft (Fig. 4.3). This shaft is not required to be nonmagnetic, so stainless steel 440C with a yield strength of 420 MPa was chosen.

Considering the safety factor of 2, the shaft diameter is computed as

$$\sigma = \frac{4000}{\pi d^2 \big/ 4} = \frac{420 \times 10^6}{2} \Rightarrow d \approx 5 \text{ mm}. \tag{4.2}$$
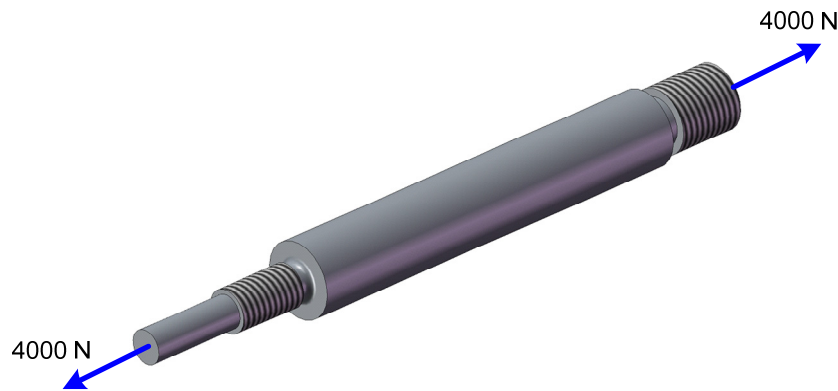
Fig. 4.3. Force-transmission shaft.

The other issue which has to be taken into account is the buckling. Considering the length of shaft of 100 mm, the shaft diameter to avoid buckling is computed as

$$P_{cr} = \frac{4\pi^2 EI}{l^2} \Rightarrow I = \frac{\pi d^4}{64} = \frac{l^2 P_{cr}}{4\pi^2 E} = \frac{0.1^2 \times 2 \times 4000}{4 \times \pi^2 \times 210 \times 10^9} \Rightarrow d \approx 4 \text{ mm.} \tag{4.3}$$

Thus, using any shaft diameter bigger than 5mm could meet mechanical strength requirements.

One end of the shaft is threaded into ¼-28 UNF 2A and screwed into the carriage. The other end is threaded into size 3/8-16 UNC 2A and is connected to the load interface which will be discussed later. The drawing of the force-transmission shaft with dimensions and tolerances is presented in Fig. A.16.

As shown in Fig. 4.4, the spring rod is a small shaft which is threaded at one end and screwed into the carriage. Its square end allows us to adjust the spring washers' preloads. It is made out of stainless steel 440C, so the minimum diameter of 5 mm is required to ensure the safe loading. The thread is ¼-20 UNC 2A and the thread length should be more than 10 mm to avoid the thread stripping. The drawing of the spring rod with dimensions and tolerances is illustrated in Fig. A.17.
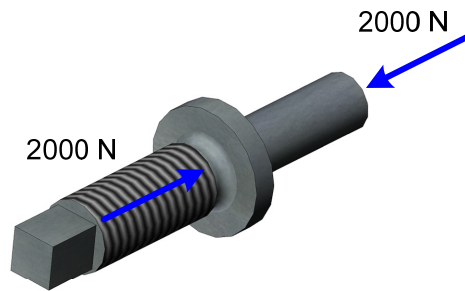
Fig. 4.4. Spring rod.

## 4.2 Stator

In the design of the stator (Fig. 4.5), its mechanical strength as well as magnetic properties has to be taken into account. From the magnetic circuit design, we saw earlier in Section 2-1 that using high-relative-permeability alloys such as Nickel-Iron Alloys will not contribute much to the level of magnetization in the Terfenol-D slab. A good material candidate for the stator is cold rolled motor lamination steel which is readily available in the market. The steel laminations should be cut according to the stator geometry by laser or die cutting, and then they could be stacked together to produce the assembled stator. In this process, due to the use of thin sheets of steel, when they are cut they would be experiencing some buckling. Thus, it would be difficult to meet the flatness requirement of the stator which is crucial in our application. On the other hand the eddy-current analysis showed that the core losses would be quite low. Since the motor speed is not of high importance in our application, the excitation frequencies could be as low as 60 Hz. Hence, another option for the stator manufacture could be machining the raw material to the final product. In search for raw material, it would be difficult to find any steel slab with certified magnetic properties such as relative magnetic permeability. Thus, as discussed earlier, although using Nickel-Iron

Alloy 49 does not contribute much to the Terfenol-D slab magnetization but since it is possible to procure this alloy with certified magnetic properties, we chose Nickel-Iron Alloy 49 [21] for the stator material.

From the mechanical strength point of view, each tooth of the stator as its most crucial part will carry two different load. One is the normal squeezing force that causes the normal stress, and the other is the shear load that generates shear stress as well as normal stress due to the bending in the root of the teeth. Here, we assume that the friction force will be equally borne by all teeth and so the total load would be divided by the number of teeth. Besides, the geometry of the teeth has already been determined in the magnetic-circuit design, and here this geometry is examined to see if it could meet the load requirements or some modifications would become necessary.
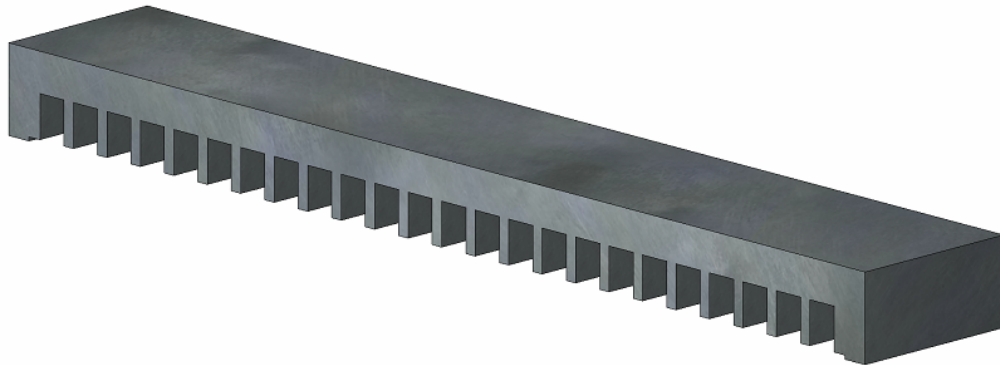


Fig. 4.5. Stator.

The output force of 4000 N is a result of friction force between the Terfenol-D slab and the intermediate plates. Assuming a friction coefficient between the Inconel plate and the Terfenol-D slab as 0.3, the required squeezing force is computed as

$$F_n = \frac{(4000/2)}{0.3} = 6667 \text{ N.} \qquad (4.4)$$

Hence the two loads applied on each teeth (Fig. 4.6) might be written as

$$V = \frac{F_f}{n} = \frac{(4000/2)}{24} = 83 \text{ N} \qquad (4.5)$$

$$F = \frac{F_n}{n} = \frac{6667}{24} = 278 \text{ N.} \qquad (4.6)$$
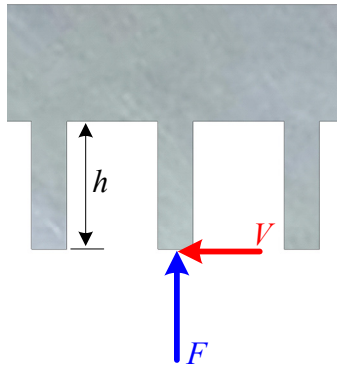


Fig. 4.6. Applied forces on the stator teeth.

The bending momentum in the root of each tooth would be

$$M = V \times h = 83 \times 0.01 = 0.83 \text{ N-m.} \qquad (4.7)$$

Hence the maximum existing normal stress would be calculated as the combination of the effects of normal force and the bending momentum

$$\sigma_x = \frac{M.C}{I} + \frac{F}{A} = \frac{0.83 \times 1.5 \times 10^{-3}}{(1/12) \times 1.78 \times 25.4 \times 10^{-3} \times (3 \times 10^{-3})^3} + \frac{278}{1.78 \times 25.4 \times 3 \times 10^{-6}} = 14 \text{ MPa}, \quad (4.8)$$

and the shear stress is

$$\tau_{xy} = \frac{V}{A} = \frac{83}{1.78 \times 25.4 \times 3 \times 10^{-6}} = 0.6 \text{ MPa}. \quad (4.9)$$

Now using the Mohr's circle, the maximum shear stress in the tooth is calculated as

$$\tau_{max} = 7 \text{ MPa}. \quad (4.10)$$

The yield strength of Nickel-Iron Alloy 49 is 154 MPa, so the current design results in a very high safety factor.

The other determining factor in the mechanical strength of the teeth is the buckling critical load. The tooth could be considered as a column with one end fixed and the other end free and so the critical load would be

$$P_{cr} = \frac{\pi^2 EI}{4l^2} = \frac{\pi^2 \times 210 \times 10^9 \times (1/12 \times 1.78 \times 25.4 \times 10^{-3} \times (3 \times 10^{-3})^3)}{4 \times (10 \times 10^{-3})^2} = 526.5 \text{ kN}, \quad (4.11)$$

which is well above the normal load applied on the tip of each tooth. The tooth deflection due to the load V could be calculated as

$$y_{max} = \frac{Vh^3}{3EI} = \frac{83 \times 0.01^3}{3 \times 210 \times 10^9 \times 1/12 \times 1.78 \times 25.4 \times 10^{-3} \times (3 \times 10^{-3})^3} = 1.3 \times 10^{-6} \text{ m}. \quad (4.12)$$

As it is seen the tooth deflection would not be considerable and it shows that the current structure of the stator is capable of withstanding the applied forces. The stator drawing with dimensions and tolerances is given in Fig. A.19.

In the machining of Nickel-Iron Alloy 49, it is important to control heat buildup. Suggested coolants are Keycool 2000 or Prime Cut. Whatever lubricant is used for machining, it should not contain sulphur. For milling this alloy 2 or 4 flute carbide tool should be employed and the surface speed could vary between 35 and 70 ft/min [21]. As shown in Fig. 4.7, to avoid the teeth damage, two small keys were made to fit exactly in the stator slots and used as supports by placing inside the stator slots.
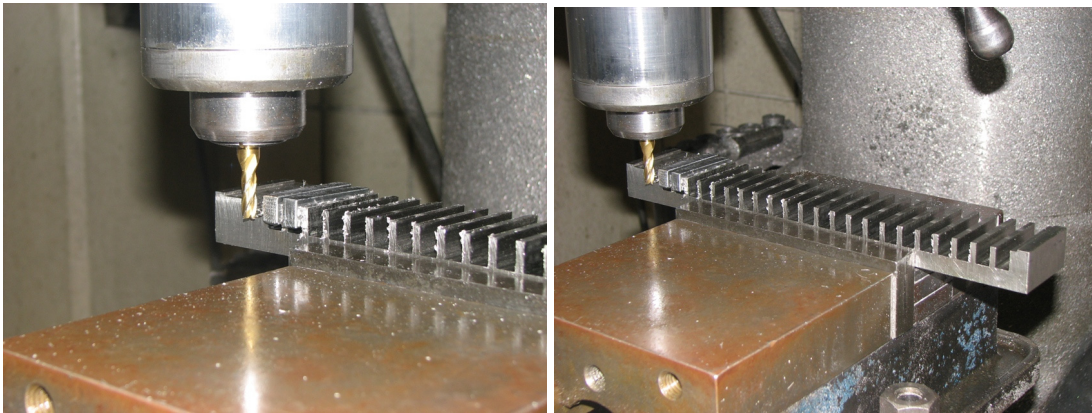


Fig. 4.7. Stator machining.

## 4.3 Inconel Plate

The normal squeezing pressure will be transferred to the Terfenol-D slab through an Inconel plate. To direct maximum magnetic flux through the Terfenol-D slab, the relative permeability of this plate should be as low as possible. On the other hand it should have the high corrosion resistant properties. To meet these two requirements, Inconel 718 alloy was chosen, which is a corrosion resistant alloy with relative permeability close to 1.

**4.4 Housing Assembly**

Housing assembly will provide required space to accommodate the stators, coils, Terfenol-D slab, and force transmission assembly. Besides, it should deliver the required normal force for squeezing the Terfenol-D slab. The generated force by the motor will be transferred to this assembly and it should be strong enough to withstand the resulted stresses. An exploded view of the housing assembly is shown in Fig. 4.8. A pair of housing pins and upper blocks act like fixtures for the stators, and a squeezing plate is pushed against the upper stator using 16 sets of Belleville spring washers. The base plate in the lowest part of assembly would be used to screw the housing assembly to an optical table.
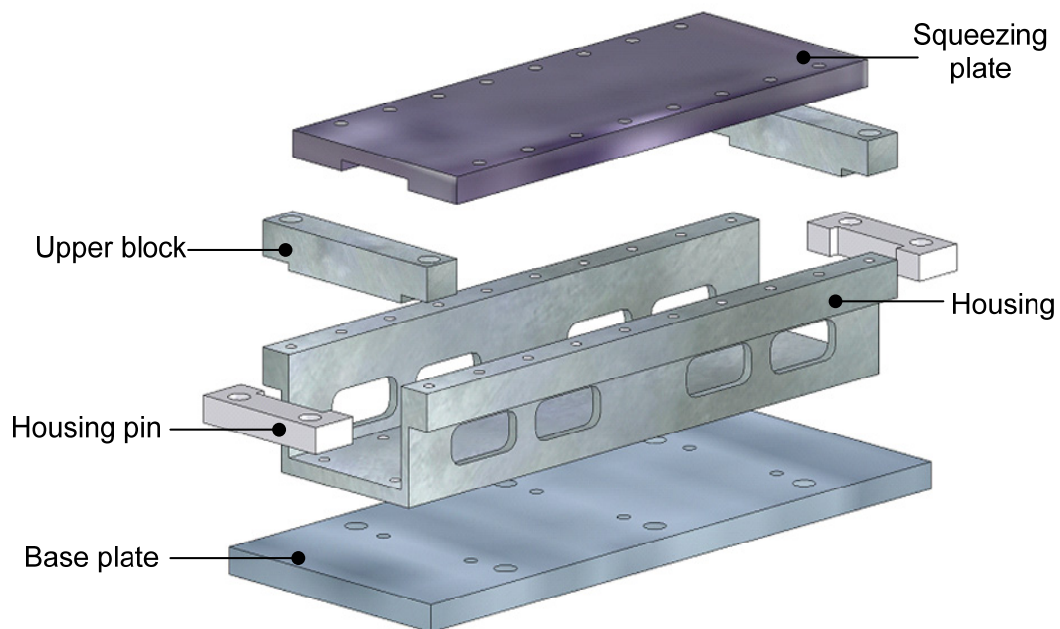


Fig. 4.8. Housing assembly.

The total load applied on the housing would be normal squeezing force which is already calculated as 6667 N. This force would be transmitted to the tapped holes on the top side of the housing through Belleville washers and screws. For having an even distribution of squeezing force throughout the Terfenol-D slab, 16 Belleville washer and screw sets are used, so 16 tapped holes were created in the top side of housing.

The axial force within each screw (Fig. 4.9) considering a safety factor of 2 would be

$$F_s = \frac{F_n \times SF}{16} = \frac{6667 \times 2}{16} = 833 \, \text{N}. \tag{4.13}$$

So the cross-sectional area of the screw should be:

$$A = \frac{F_s}{S_y} = \frac{833}{464 \times 10^6} = 1.79 \, \text{mm}^2 \Rightarrow d \approx 1.5 \, \text{mm}. \tag{4.14}$$

Hence, using sixteen ¼-28 UNF 2A hex-head screws could easily transfer the required normal pressure to the squeezing plate. Here, a fine thread was chosen intentionally to allow fine tuning of the squeezing pressure.
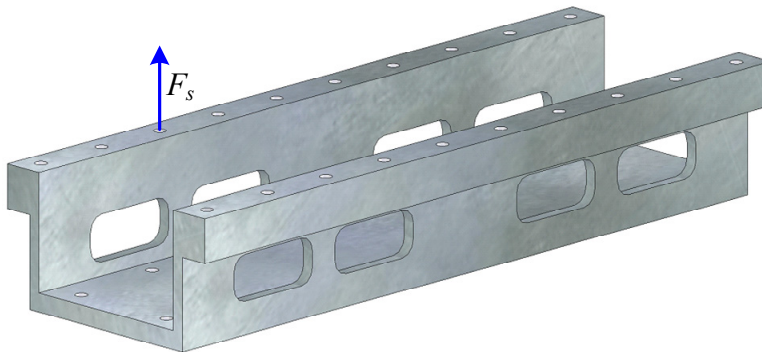


Fig. 4.9. Housing.

Instead of making the housing out of several smaller parts and screwing or brazing them together, the whole housing body would be made (Fig. 4.10) from a solid piece of steel A36. By doing this, the concern over thermal distortion due to brazing or lack of precision in assembly would be removed. The drawings of the housing with dimensions and tolerances are given in Figs. A.7–A.8.



Fig. 4.10. Housing machining.

The housing pin is made out of steel grade A36 and using two ¼-20 UNC 2A hex-head screws connected to the housing body and stops axial and lateral movements of the lower stator. The drawing of the housing pin with dimensions and tolerances is included in Fig. A.6.

The upper block is made from steel grade A36 and using two ¼-20 UNC 2A hex-head screws, is screwed to the housing body, and stops only axial movements of the upper stator. The drawing of the upper block with dimensions and tolerances is shown in Fig. A.22.

The maximum bending momentum will take place in the middle of the squeezing plate accompanied by a shear load (Fig. 4.11)

$$V = 3333 \ \text{N} \tag{4.15}$$

$$M = 3333 \times 94/2 \times 10^{-3} = 157 \ \text{N-m} . \tag{4.16}$$

Thus, the resulting shear and normal stresses would be

$$\tau = \frac{V}{A} = \frac{3333}{8 \times 280 \times 10^{-6}} = 1.5 \ \text{MPa} \tag{4.17}$$

$$\sigma = \frac{M.C}{I} = \frac{157 \times 4 \times 10^{-3}}{1/12 \times 280 \times 10^{-3} \times (8 \times 10^{-3})^3} = 52 \ \text{MPa}. \tag{4.18}$$
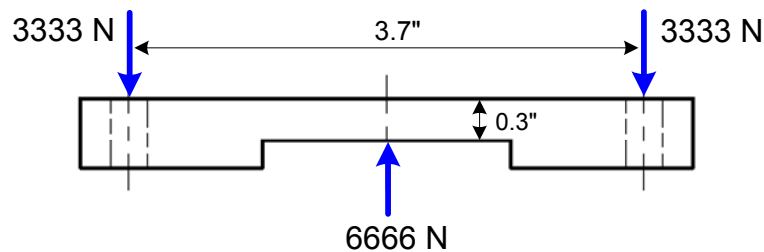


Fig. 4.11. Exerted forces on squeezing plate.

Using the Mohr's circle, the maximum shear stress would be 26 MPa. Hence using steel A36 with the yield strength of 250 MPa, the mechanical strength requirements could be easily met. The drawing of the squeezing plate with dimensions and tolerances is given in Fig. A.18.

**4.5  Base Plate**

The base plate is used as an interface between the housing and the optical table. Since no threaded holes have been considered on the base plate, general-purpose aluminum grade 6061 was used as the material for this part. The drawing of the base plate with dimensions and tolerances is shown if Fig. A.3.

In Fig. 4.12, an exploded view of the linear magnetostrictive actuator is shown.
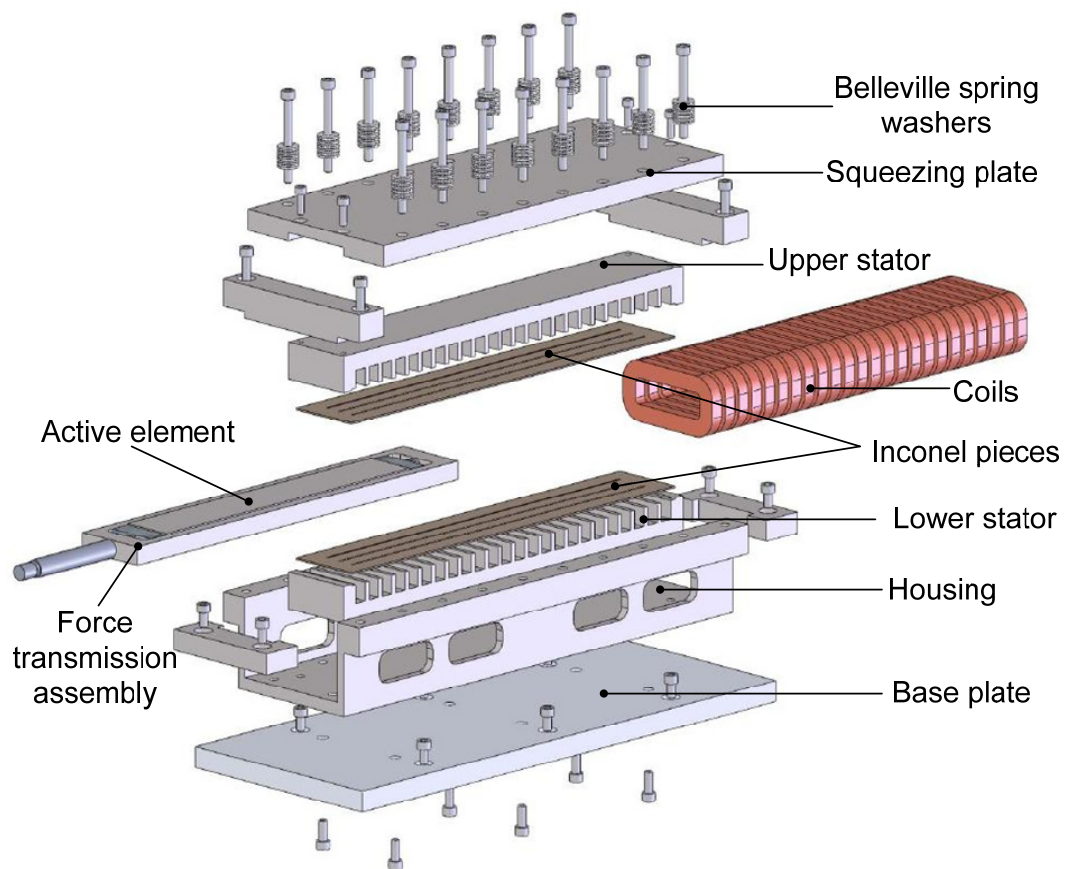
Fig. 4.12. Exploded view of the linear magnetostrictive actuator [20].

## 4.6 Troubleshooting

Right after the assembly and during the first tests, it was noticed that the Terfenol-D slab was stuck and actuator was unable to generate any movement after applying the squeezing force. By thorough examination of the actuator, the stator bending was turned out to be the source of problem. The photographs that illustrate this curvature measurement and the obtained bending profile are shown in Fig. 4.13. Interestingly, it was observed that both lower and upper stators share the same bending profile.
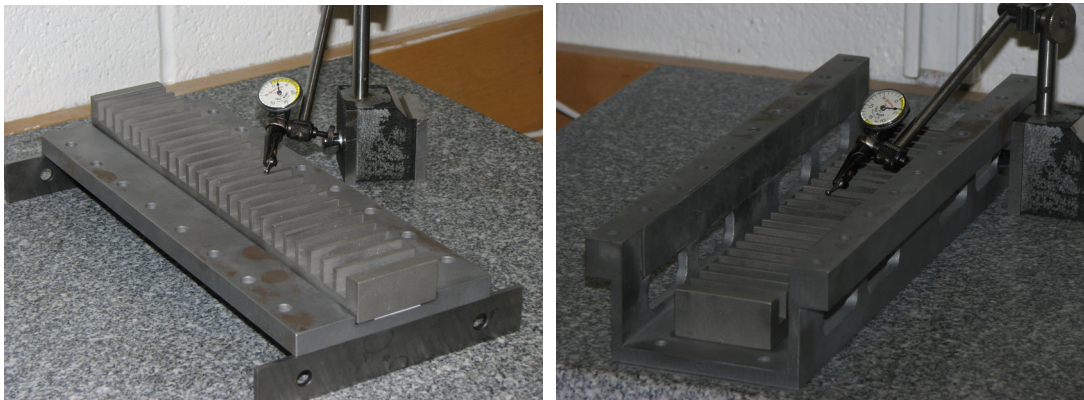


(a)
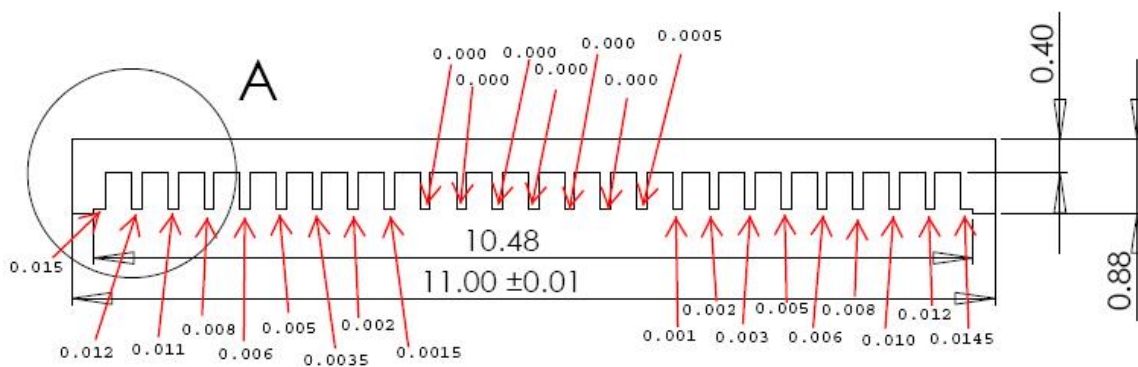


(b)

Fig. 4.13. (a) Stator bending measurements were done for both upper and lower stators. (b) Stator bending profile.

To deal with this problem the following options were considered:

- machining the stators

- applying compensating forces

Since we had a little room for further machining the teeth of stators and yet machining could damage the teeth, this option was ruled out. To apply the compensating forces to bend the stators back to their flat position, we could have applied a vertical force in the middle of the stator while two ends were sitting against the machine press bed. Again here, there was the risk of overloading the stator and damage could occur. Finally it was decided to use a pair of bolts in each end of the stator to pull it back to its flat position (Fig. 4.14). For this purpose two tapped holes with the size of 8-32 UNF were made at each end of stators after the actuator disassembly. Four holes were drilled in squeezing plate and four in housing and then they were counterbored to provide space for the head of the hex-head screws.
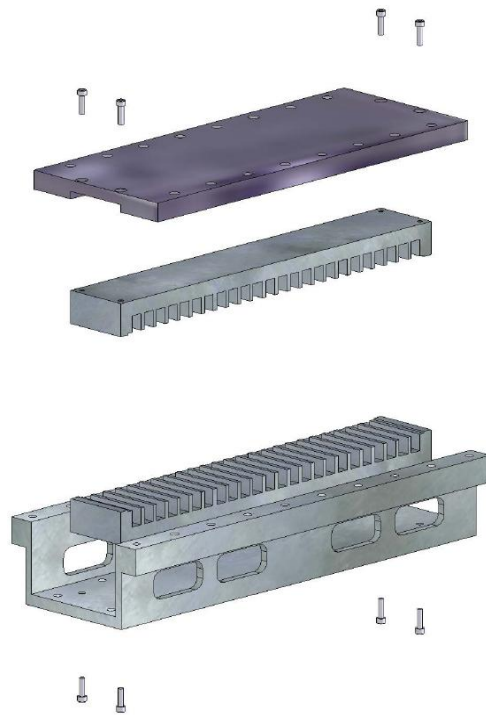
Fig. 4.14. Stator adjustment methodology.

The stators were then bolted to the housing and the squeezing plate. Required adjustment was preformed using thin shims and the bending profile was measured with the results shown in Fig. 4.15. As it is seen, there would be now an outward bending which will not cause any malfunction in the operation of the actuator. Then, the actuator was assembled, and tests showed that the Terfenol-D would move and generate force as predicted after applying the squeezing force. Fig. 4.16 shows the assembled actuator and the incorporated bolts in upper stator.
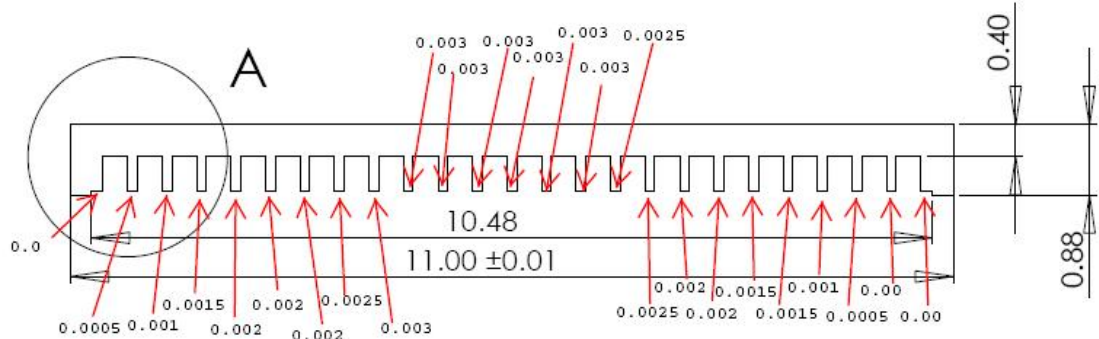


Fig. 4.15. Stator bending profile after adjustment.
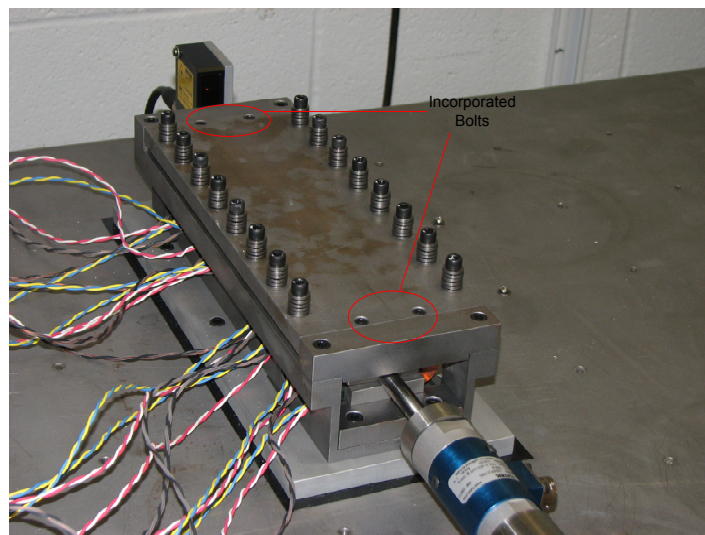


Fig. 4.16. Assembled actuator after adjustment.

# CHAPTER V

# MODELING AND CONTROL

So far, we designed, fabricated and assembled the linear magnetostrictive actuator. In this chapter the modeling and control of the actuator will be discussed. First, various linear model of magnetostrictive materials and the magnetomechanical coupling are reviewd. Then, finite element modeling of the magnetostrictive actuator is presented using ATILA software [9]. An empirical approach to modeling is then pursued by performing tests on the actuator and its correlation with the FE model is studied. Eventually, a closed-loop controller of the linear magnetostrictive actuator is implemented using relay control.

## 5.1 Linear Model

Linear models can be used to describe the behavior of magnetostrictive materials in moderate excitations. Here, we assume that magnetostrictive materials do not exhibit any hysteresis. To develop the linear model, first we look at the magnetomechanical coupling in magnetostrictive materials.

## 5.1.1 Magnetomechanical Coupling

Applying magnetic field to magnetostrictive materials results in mechanical strain in addition to strains originated form mechanical stresses. On the other hand, their magnetization changes as a result of changes in mechanical stresses in addition to the changes resulted from variation in magnetic field. This property is called magnetomechanical coupling which can be described by [27]

$$S = S(T,H)$$
$$B = B(T,H)$$
<div align="right">(5.1)</div>

where $S$ is the mechanical strain, $T$ is the mechanical stress, $H$ is the applied magnetic field,

and $B$ is the magnetization.

By differentiating the previous equations, we will have [27]

$$dS_i = \left.\frac{\partial S_i}{\partial T_j}\right|_H dT_j + \left.\frac{\partial S_i}{\partial H_k}\right|_T dH_k \ , i = 1,...,6$$

$$dB_i = \left.\frac{\partial B_m}{\partial T_j}\right|_H dT_j + \left.\frac{\partial B_m}{\partial H_k}\right|_T dH_k \ , m = 1,2,3$$
<div align="right">(5.2)</div>

We denote constants of compliances and permeabilities as

$$\left.\frac{\partial S_i}{\partial T_j}\right|_H = s_{ij}{}^H \ , \ elastic\ compliances\ at\ cons.H$$

$$\left.\frac{\partial B_m}{\partial H_k}\right|_T = \mu_{mk}{}^T \ , \ magnetic\ permeabilities\ at\ cons.T$$
<div align="right">(5.3)</div>

Then the linearized constitutive equations for small variations in $dT$ and $dH$ can be

formulated as

$$S_i = s_{ij}{}^H T_j + d_{ki} H_k \ , i = 1,...,6$$

$$B_m = d_{mj} T_j + \mu_{mk}{}^T H_k \ , m = 1,2,3$$
<div align="right">(5.4)</div>

For a polycrystalline ferromagnetic material with $x_3$ chosen as the direction of the magnetic

polarization (magnetic bias) and prestress (mechanical bias), Eq. 5.4. turn out to be [27]

$$\begin{bmatrix} S_1 \\ S_2 \\ S_3 \\ S_4 \\ S_5 \\ S_6 \end{bmatrix} = \begin{bmatrix} s_{11}^H & s_{12}^H & s_{13}^H & 0 & 0 & 0 \\ s_{12}^H & s_{11}^H & s_{13}^H & 0 & 0 & 0 \\ s_{13}^H & s_{13}^H & s_{33}^H & 0 & 0 & 0 \\ 0 & 0 & 0 & s_{44}^H & 0 & 0 \\ 0 & 0 & 0 & 0 & s_{44}^H & 0 \\ 0 & 0 & 0 & 0 & 0 & s_{66}^H \end{bmatrix} \cdot \begin{bmatrix} T_1 \\ T_2 \\ T_3 \\ T_4 \\ T_5 \\ T_6 \end{bmatrix} + \begin{bmatrix} 0 & 0 & d_{31} \\ 0 & 0 & d_{31} \\ 0 & 0 & d_{33} \\ 0 & d_{15} & 0 \\ d_{15} & 0 & 0 \\ 0 & 0 & 0 \end{bmatrix} \cdot \begin{bmatrix} H_1 \\ H_2 \\ H_3 \end{bmatrix} \tag{5.5}$$

$$\begin{bmatrix} B_1 \\ B_2 \\ B_3 \end{bmatrix} = \begin{bmatrix} 0 & 0 & 0 & 0 & d_{15} & 0 \\ 0 & 0 & 0 & d_{15} & 0 & 0 \\ d_{31} & d_{31} & d_{33} & 0 & 0 & 0 \end{bmatrix} \cdot \begin{bmatrix} T_1 \\ T_2 \\ T_3 \\ T_4 \\ T_5 \\ T_6 \end{bmatrix} + \begin{bmatrix} \mu_{11}^T & 0 & 0 \\ 0 & \mu_{11}^T & 0 \\ 0 & 0 & \mu_{33}^T \end{bmatrix} \cdot \begin{bmatrix} H_1 \\ H_2 \\ H_3 \end{bmatrix} \tag{5.6}$$

### 5.1.2 Finite Element Modeling

The FE modeling of the magnetostrictive material could be performed by a variational formulation for the equations associated to the electromechanical coupling [28]. For this purpose, ATILA which is a finite element code was employed. The FE model is based on the following assumptions.

a) Magnetization and magnetostriction are not rate dependent which means the rate of applying magnetic field or mechanical stress doesn't have impact on magnetization or magnetostriction levels.

b) The sources are described by finite number of excitation currents.

c) The material behavior is linear and nonhysteretic.

d) The system energy is conservative.

There is also a material database in ATILA where the magnetostrictive material can be specified. For 3-D FE model of the linear magnetostrictive actuator, we require to have numerical values of all nonzero elements in the material matrixes in (5.5) and (5.6). The numerical values of these constants for a magnetostrictive material are listed in Table 5.1.

Table 5.1. Numerical values of magnetostrictive constants [27].

| Constant | Value |
|----------|-------|
| $s_{11}^H$ | $12.5 \times 10^{-11}$ |
| $s_{12}^H$ | $-1.8 \times 10^{-12}$ |
| $s_{13}^H$ | $-1.7 \times 10^{-11}$ |
| $s_{33}^H$ | $4.0 \times 10^{-11}$ |
| $s_{44}^H$ | $1.8 \times 10^{-10}$ |
| $s_{66}^H$ | $5.4 \times 10^{-11}$ |
| $s_{11}^B$ | $3.5 \times 10^{-11}$ |
| $s_{12}^B$ | $-1.3 \times 10^{-11}$ |
| $s_{13}^B$ | $-8.4 \times 10^{-12}$ |
| $s_{33}^B$ | $2.1 \times 10^{-11}$ |
| $s_{44}^B$ | $1.2 \times 10^{-10}$ |
| $s_{66}^B$ | - |
| $d_{31}$ | $-5.3 \times 10^{-9}$ |
| $d_{15}$ | $2.8 \times 10^{-8}$ |
| $d_{33}$ | $1.1 \times 10^{-8}$ |
| $\mu_{11}^T$ | $1.3 \times 10^{-5}$ |
| $\mu_{33}^T$ | $5.3 \times 10^{-6}$ |
| $\mu_{11}^B$ | $5.7 \times 10^{-6}$ |
| $\mu_{33}^B$ | $2.7 \times 10^{-6}$ |

To perform the FEA analysis of the linear magnetostrictive actuator, its geometry was modeled in GiD preprocessor [29] and then ATILA was used to solve the magneto-mechanical coupling in the active element. The simulation results for the local three-phase excitation of the linear magnetostrictive actuator are shown in Fig. 5.1. As the magnetic field comes to interact with the active element, it results in radial contraction of that portion and consequently the longitudinal extension of the active element. Then, the magnetic field is moved to the other end which results in overall displacement of the active element.
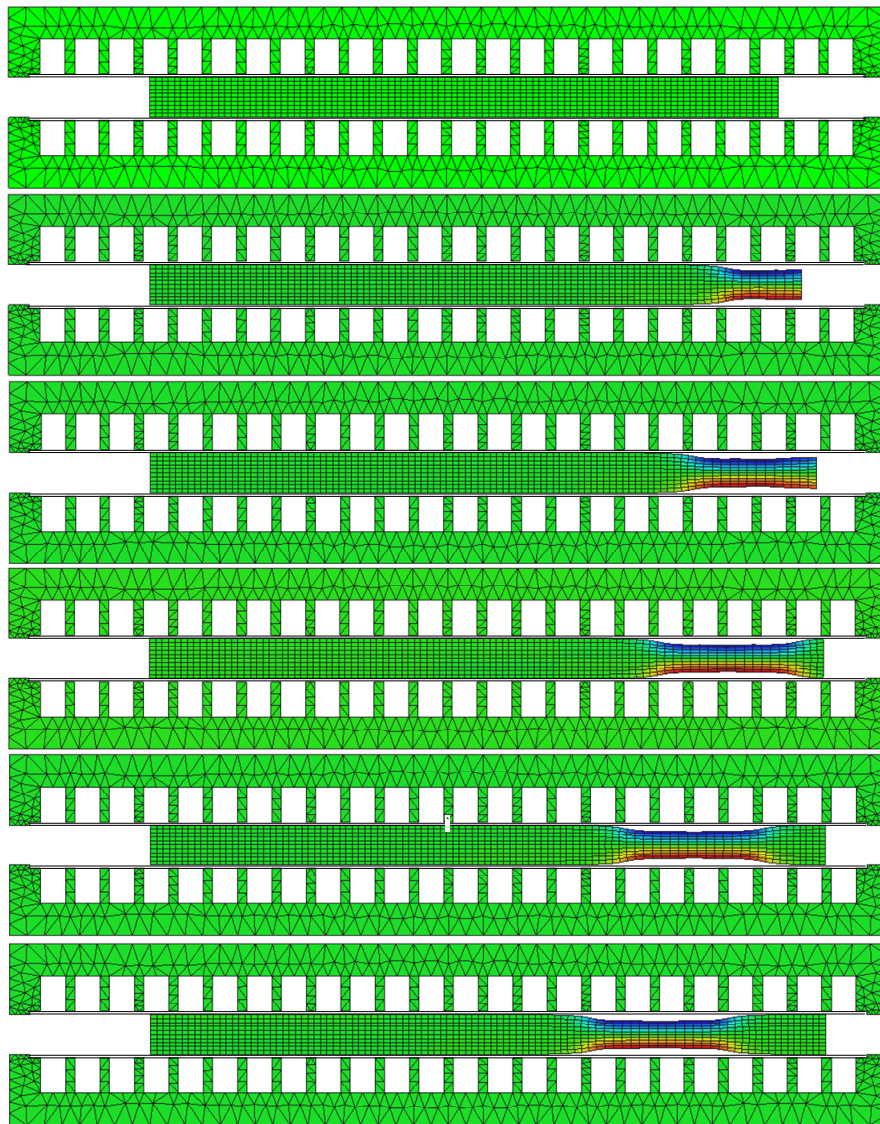
Fig. 5.1. FEA analysis of the linear magnetostrictive actuator in local three-phase excitation mode (The displacement is magnified with a factor of one million). Three adjacent coils are excited from right with $i = 2.5$ A in each coil [30].

## 5.2 Empirical Model

It was shown that the speed of a linear magnetostrictive actuator is a function of the peak magnetostrictive strain, mechanical stress, and operation frequency [15]. For the linear

magnetostrictive actuator under local multi-phase operation, the modified relationship

between the motor speed and design parameters is given by:

$$v = N f p (\varepsilon_{max} - \frac{F}{EA_T})$$

(5.7)

where

$N$  Number of phases (3)

$f$  Local multi-phase operation frequency (Hz)

$p$  Slot pitch (10.9 mm)

$\varepsilon_{max}$  Peak magnetostrictive strain under no-load condition

$F$  External load (N)

$E$  Young's modulus of Terfenol-D (35 GPa)

$A_T$  Cross-sectional area of the Terfenol-D slab (400 mm$^2$)

Thus, the speed is proportional to the sum of the opposing strains from two different

origins. One is the magnetostrictive strain denoted by $\varepsilon_{max}$, and the other is mechanical strain

denoted by $F/EA_T$ resulted from the external load applied on the active element. The

magnetostrictive strain is a function of applied magnetic field and could be calculated using

the magnetostriction curve given in [18], [31].

## 5.2.1  Experiment Results

To better understand the behavior of the linear magnetostrictive actuator, numerous

sets of experiments were designed and executed which will be discussed in the following

sections.

**Speed vs. Squeezing Force**

The normal force applied by the squeezing mechanism affects both the speed and the blocking force of the linear magnetostrictive actuator. An increase in squeezing force boosts the friction force between the active element and the inconel pieces resulting in a higher blocking forces. To verify the impact of the squeezing force on the speed of the actuator, it increased from zero to 6000 N, and the speed of the actuator was recorded as shown in Fig. 5.2. By increasing the squeezing force up to around 2000 N, the speed increases and by further raising the squeezing force the speed drops. This phenomenon could be explained in this manner that in the beginning by increasing the squeezing force, the Inconel intermediate plates come to more close contact with the Terfenol-D slab surface. This stops the Terfenol-D slab from slipping and causes a boost in speed. When the squeezing force goes beyond a certain limit, the magneto-mechanical coupling [28] in Terfenol-D causes the magnetization of Terfenol-D slab to decrease which consequently makes the magnetostrictive strains smaller and the actuator speed drops.
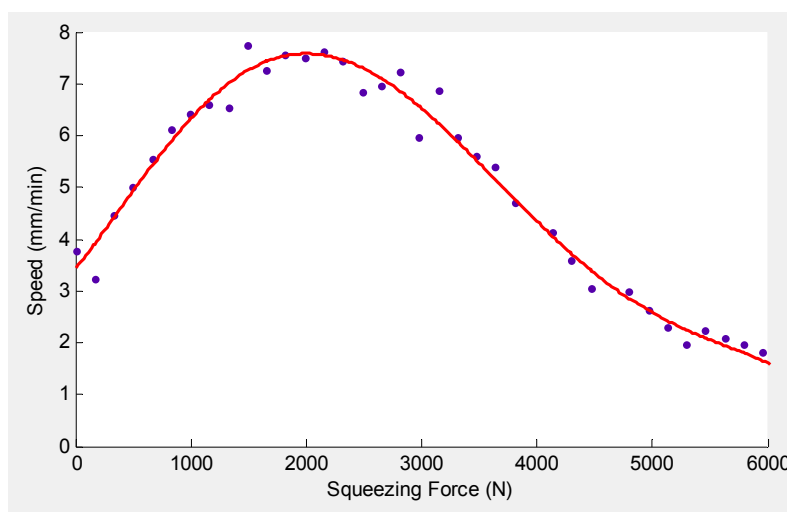


Fig. 5.2. Speed-squeezing force characterization curve at frequency of 10 Hz and phase current of 2.1 A.

**Minimum Current vs. Squeezing Force**

To find the relationship between the minimum current required to make the actuator move and the squeezing force, the frequency and phase current were kept constant at 10 Hz and 2.1 A, and then the squeezing force was increased from zero to 6616 N and the current was recorded. Fig. 5.3 shows the minimum current versus the squeezing force. In the beginning by increasing the squeezing force up to around 2000 N, the minimum current decreases. By further increasing the squeezing force the minimum current increases. This phenomenon has the same explanation as what was discussed in the last part.
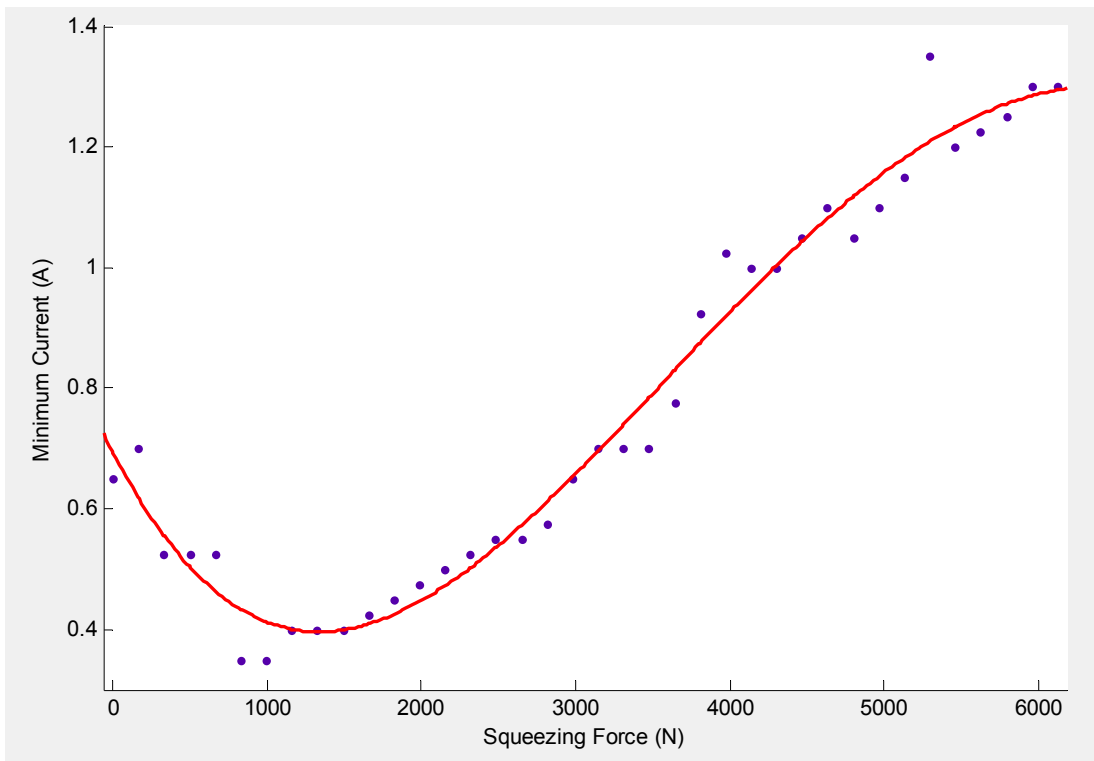


Fig. 5.3. Minimum current versus squeezing force curve at frequency of 10 Hz and phase current of 2.1 A.

**Speed vs. Frequency**

To analyze the relationship between the actuator speed and the operation frequency, the peak phase current was kept at 2 A, the frequency was increased from 1 Hz to 10 Hz, and the actuator speed was recorded. As seen in Fig. 5.4, the speed is a linear function of the operation frequency.
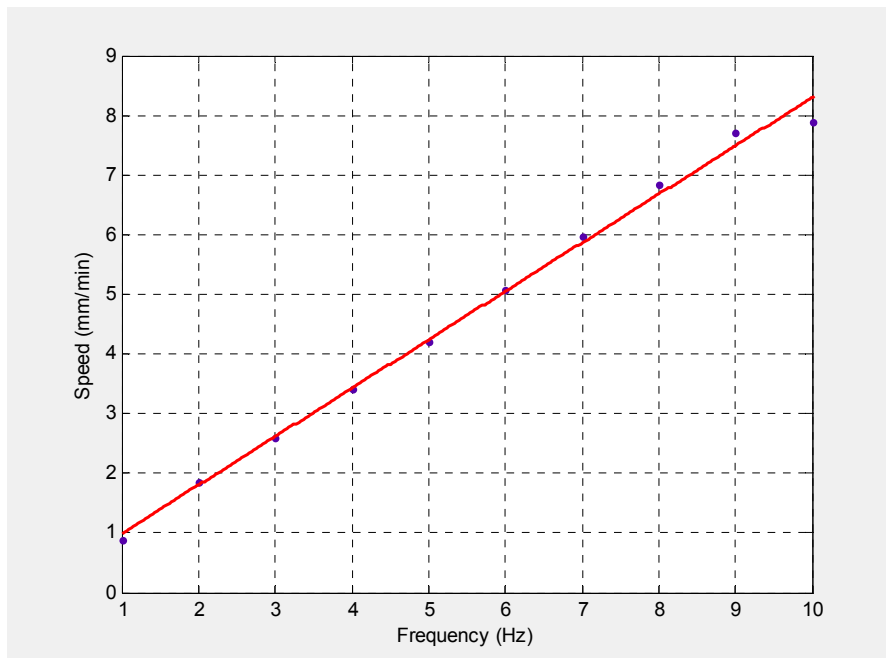


Fig. 5.4. Speed-frequency characterization curve at phase peak current of 2 A.

**Speed vs. Current**

To analyze the relationship between the actuator speed and the phase current, the squeezing force was set to be 2000 N at constant frequency of 10 Hz, and the peak phase current was increased from 0.5 A to 2.9 A. The motion profiles are shown in Fig. 5.5 and the speed-current characterization curve is shown in Fig. 5.6. As seen in low currents, the speed

is speed curve slope is small. In fact, at low currents, the magnetostrictive strains are very small which result in small contraction of the Terfenol-D slab and higher friction forces between Terfenol-D slab and Inconel piece. This causes a drop in the actuator speed at low currents. The speed curve slope in high currents starts to decrease which is due to the saturation in the active element.

**Speed vs. Load**

To find the laod capability of the actuator, we used the friction force between a set of dead weights and the smooth plate fastened to optical table as load. The test setup with dead weights are shown in Fig. 5.7. To find the relationship between the speed and the external load, the load was increased from 50 N to above 410 N, and the corresponding speed was recorded. The results for the experiment at frequency of 5 Hz and phase peak current of 2.75 A are shown in Fig. 5.8. It is seen that this actuator can handle a load of up to 410 N. As seen in Fig. 5.8 by increasing the load the speed drops which is in agreement with (5.7).
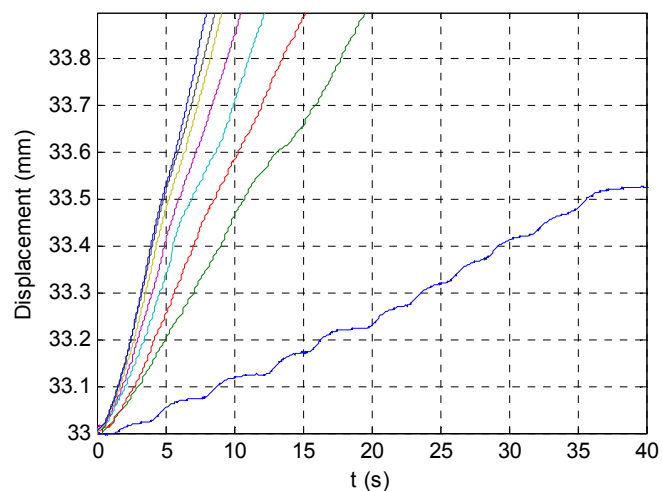


Fig. 5.5. No-load tests of linear magnetostrictive actuator excited at 10 Hz and with varying peak phase currents 0.6, 1.1, 1.35, 1.6, 1.85, 2.1, 2.3, and 2.55 A from the bottom.
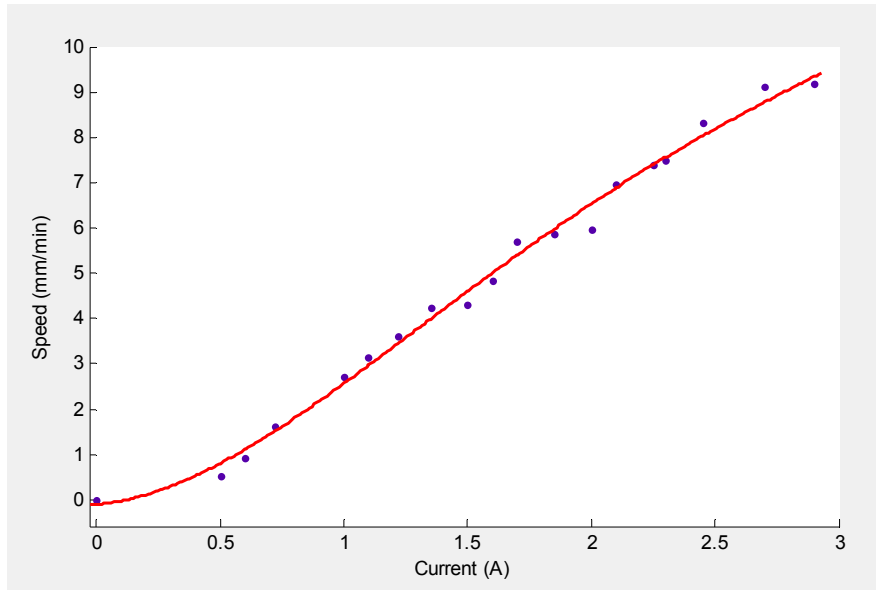
Fig. 5.6. Current-speed characterization curve.
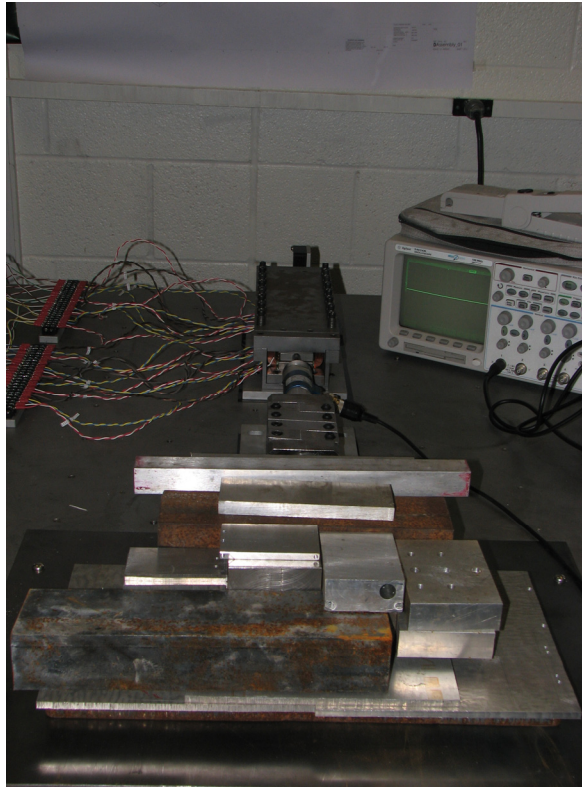


Fig. 5.7. Photograph of test setup with dead weights as load.
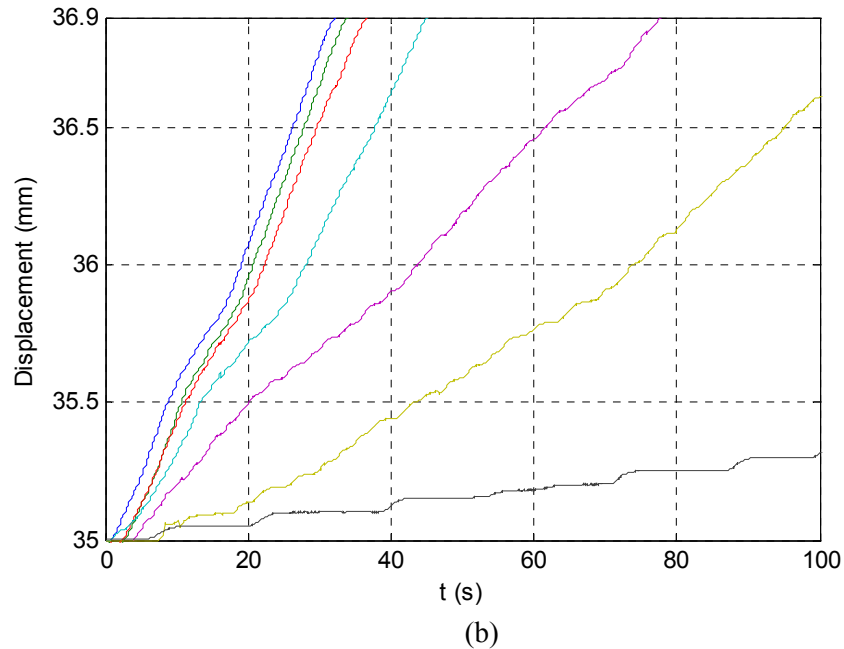
Fig. 5.8. Load tests of the linear magnetostrictive actuator at the peak phase current of 2.75 A and the frequency of 5 Hz with varying loads 50, 100, 150, 200, 250, 300 N, and 410 N from the top.

## 5.3 Modified Empirical Model

To verify the effectiveness of the model described by (5.7), the model-predicted speed was compared with the actual speed of the linear magnetostrictive actuator. To do this, the magnetic field intensity inside the active element was calculated in different currents using FEA. Then, the magnetostriction curve as in [18], [31] was used to calculate the magnetostrictive strain. The results are illustrated in Fig. 5.9. The error between the model-predicted speed and the actual one is associated with the impact of surface roughness of the active element and also the Inconel pieces, which was not included in (5.7), unavoidable misalignments during the assembly, and deformation of stators and the Inconel pieces due to the application of the squeezing force. It is seen that as coil current increases, the error percentage decreases. This is due to the fact that at low currents, the magnetostrictive strains

are very small. This results in very small lateral contraction of the active element which causes the increase in friction force between the active element and the Inconel pieces. This friction force leads to a drop in the speed of the actuator in low currents. However, as the current increases, it boosts the lateral contraction of the active element which enables it to elongate without being opposed by the friction force imposed by the inconel pieces.
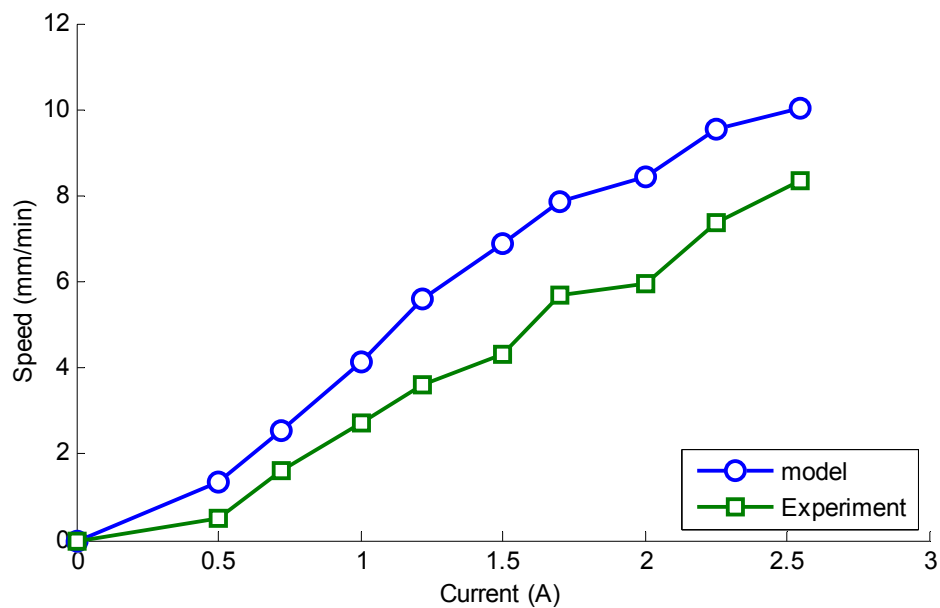


Fig. 5.9. Comparison between the model-predicted speed and the actual speed of linear magnetostrictive actuator.

As it was seen earlier, by increasing the squeezing force up to around 2000 N, the speed increases and then it starts to drop. To incorporate this effect into the model, we define curve $\beta(S)$ as shown in Fig. 5.10. This curve shows the drop in speed as a percentage of the maximum speed. The simple model introduced in (5.7) could now be enhanced to include the impact of squeezing force

$$v = \beta(S)\, N\, f\, p\, (\varepsilon_{max} - \frac{F}{EA_T})\,, \qquad (5.8)$$

where $\beta(S)$ is a function of squeezing force, $S$. Since increasing the squeezing force beyond 4 kN results in very low speed of the actuator which is not technically desirable, the experimental data was truncated above this point and $\beta(S)$ was estimated by a second-order polynomial as

$$\beta(S) = -0.12S^2 + 0.51S + 0.43\,, \qquad (5.9)$$

where $S$ is the squeezing force in kN.
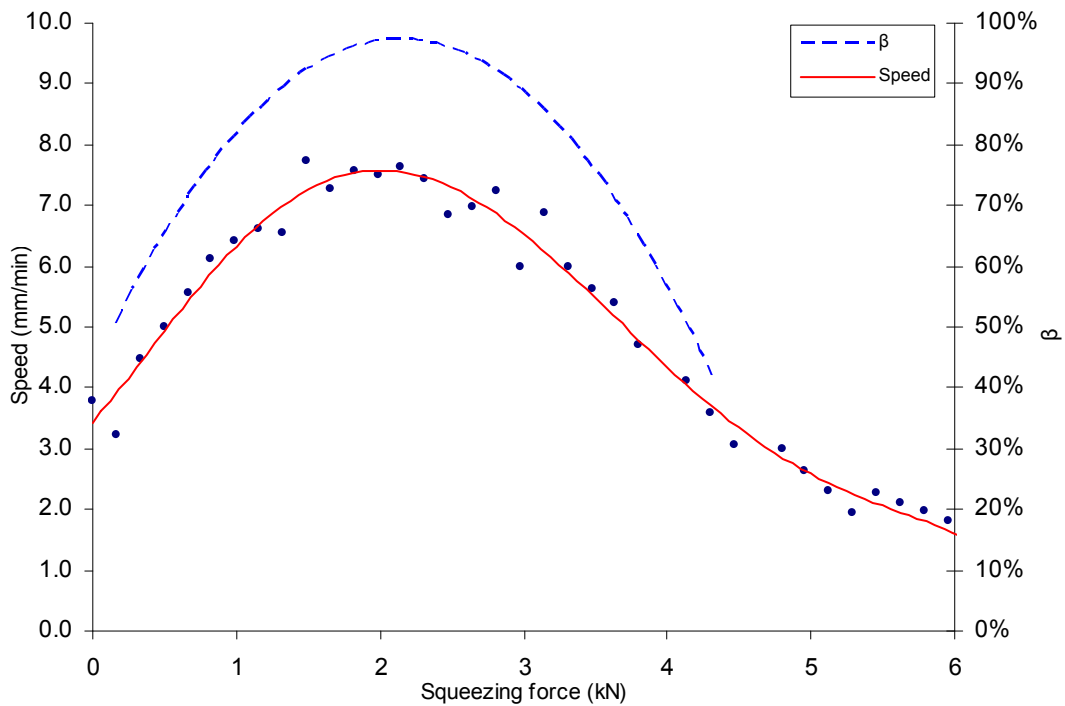


Fig. 5.10. Linear magnetostrictive actuator speed vs. squeezing force.

**5.4 Power Consumption**

The phase currents were measured using Hall-effect-based current transducers (model LA 03-PB from LEM). The output voltages of the current transducers were sent to the channels of the 16-bit A/D converter of the DSP board. The coil current profiles at a phase voltage of 13 V and operation frequencies of 1 and 10 Hz are shown in Fig. 5.11.

The power consumption of the linear magnetostrictive actuator could then be calculated by integrating the current profile and using the following equation.

$$P = N V \left( \frac{1}{T_2 - T_1} \int_{T_1}^{T_2} i(t)\, dt \right), \tag{5.10}$$

where $N$ is the number of coils, $V$ is the phase voltage, and $i(t)$ is the instantaneous current in each coil. The maximum power consumption then is calculated at the phase voltage of 13 V to be 95 W.



Fig. 5.11.  Current profile in coils with phase voltage at 13 V and operation frequencies of 1 and 10 Hz.

**5.5 Closed-Loop Control**

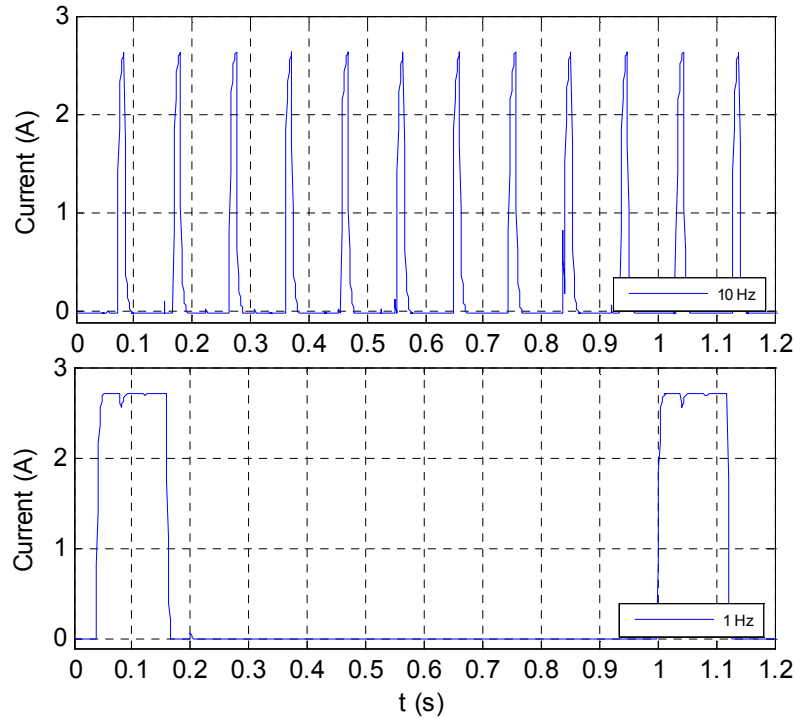We designed and successfully implemented a relay-based control system resulting in the minimum settling time with minimum overshoot. The schematic diagram of the closed-loop control system is shown in Fig. 5.12. The active element's position is monitored using the laser distance sensor and fed back to the controller. Based on the error value, the control signal is generated and sent via the digital I/O channels of the DSP board to the switching boards. Relay controllers have advantages over conventional linear controllers such as simplicity of design and fast response. In addition, unlike conventional linear controllers, a relay controller could be designed even when an exact model of the system is unavailable [32]. The Simulink block diagram of the control system is shown in Fig. B.1.
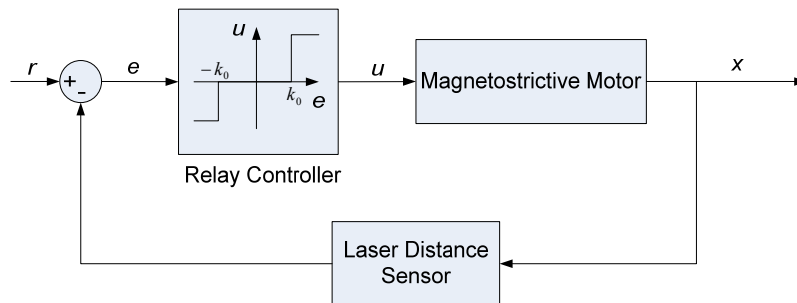


Fig. 5.12. Schematic diagram of the closed-loop control system.

To avoid self-oscillations [32] in the system response, we consider a relay controller with a dead zone defined as

$$u = \Phi(e) = \begin{cases} +1 & e > k_0 \\ 0 & -k_0 < e < k_0 \\ -1 & e < -k_0 \end{cases},$$ (5.11)

where $u$ is the control signal and defines the actuator's movement direction by specifying the switching sequence of the MOSFET switches, and the threshold values, $\pm k_0$, define the dead

zone of the relay element. Due to the low speed of this actuator, to achieve the maximum possible speed, the phase voltage and the operation frequency are set at their maximum values. By doing so, the absolute value of the control signal is always maximized, which makes the motor move in either direction at the maximum speed.

We performed closed-loop tests with various values for $k_0$. As seen in Fig. 5.13, for the threshold value of 0.005 mm, the 1-mm closed-loop step response exhibited self-oscillations. We gradually increased the threshold value, and the self-oscillation frequency decreased as the threshold value increased. Finally, by choosing the threshold value as 0.02 mm, the self-oscillation disappeared. The 1-mm closed-loop step response with the dead-zone threshold value equal to 0.02 mm is shown in Fig. 5.14(a). There is no more oscillation in the response. By further increasing the threshold value we might even remove the overshoot, but the downside would be the increase in steady-state error. Fig. 5.14(b) shows the capability of the designed controller in tracking a sinusoidal reference input with an amplitude of 0.5 mm and frequency of 0.05 rad/s.
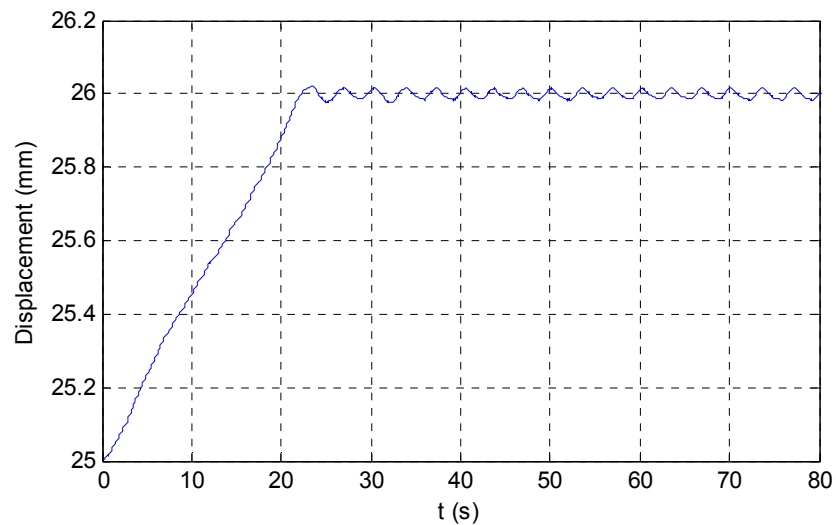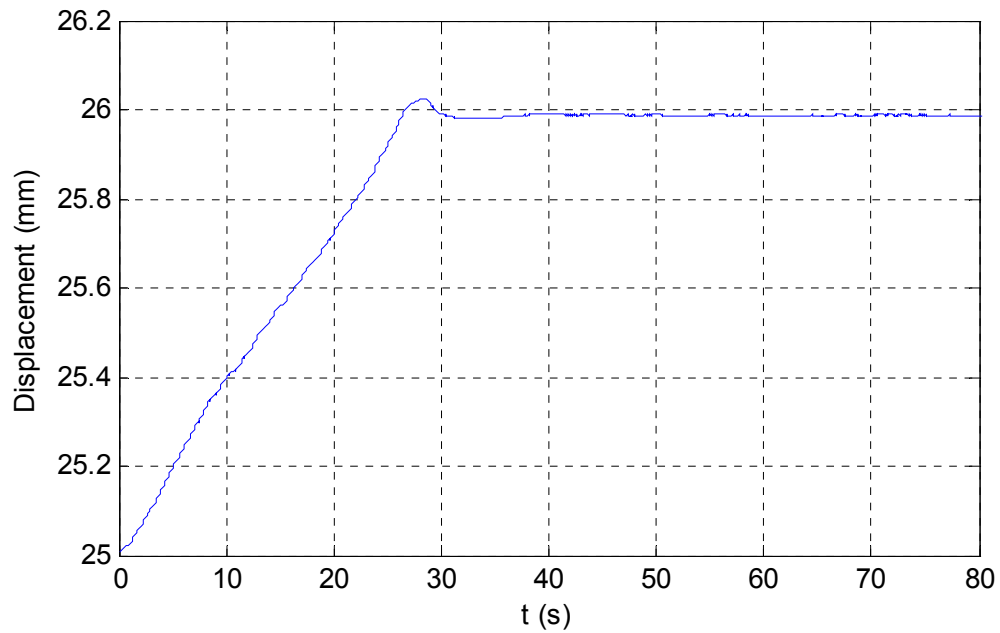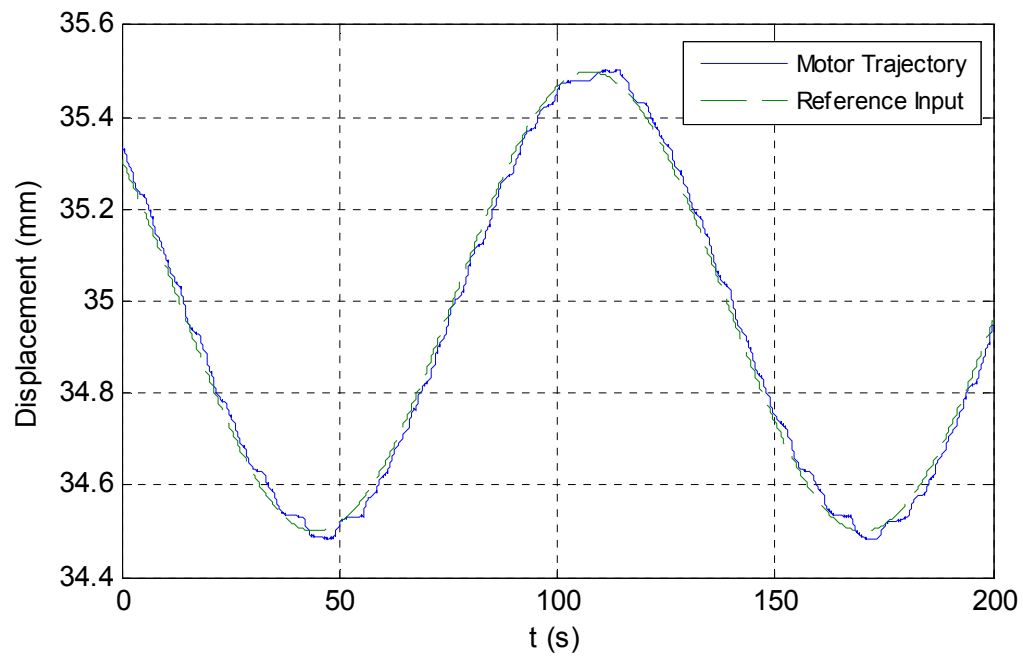


Fig. 5.13. 1-mm closed-loop step response with an excitation frequency at 10 Hz and a phase voltage of 5 V and the dead-zone threshold values of ±0.005 mm.

Fig. 5.14. (a) The same step response with the dead-zone threshold values of ±0.02 mm. (b) Closed-loop response to a sinusoidal reference input with an amplitude of 0.5 mm and frequency of 0.05 rad/s.

# CHAPTER VI

# SENSORLESS CONTROL

Operating electric motors in harsh environments at high temperature and pressure poses a serious challenge in the reliable use of conventional sensors [33]. To overcome this problem, sensorless techniques have been developed where the mechanical position sensors are eliminated by an electronic method [34]. The main idea behind the most of sensorless techniques is to find a fundamental relationship between the motor's position and its magnetic characteristics. By monitoring variables such as the current from either energized or unenergized phases, it is possible to track the changes in the magnetic characteristics of the motor [35]. In the energized-phase methods, the variables from the phases which generate torque or force are employed for position estimation [36]. In most of unenergized-phase techniques, the phase inductance in an unenergized phase is measured and used for position estimation [37]. In these techniques, generally a probing signal has to be injected to the unenergized phases for inductance calculation. Then the relationship between the motor's position and the phase inductance is used to estimate the position.

In this chapter we develop a sensorless method for closed-loop position control of the linear magnetostrictive actuator. Based on an observation which illustrates a direct relationship between the motor's position and the coils' inductances, a fundamental relationship was developed between the motor's position and the coils' current-response pulse widths. Then an algorithm was proposed to estimate the motor's position based on current-response pulse widths.

**6.1 Sensorless Position Estimation**

Most sensorless techniques are based on the development of a fundamental relationship between the motor position and its magnetic characteristics. In search for such a relationship in the linear magnetostrictive actuator, the active element was put in a predefined position and the coils' inductances were measured using an RLC meter. The cross-section of the linear magnetostrictive actuator with the active element put in a predefined position and the coils' inductances measurements are shown in Fig. 6.1.

The inductance of the coils which the active element is completely through is measured above 15 mH. In comparison, the inductances of other coils are around 10 mH. It is apparent that the increase in coils' inductances is due to the relative permeability of Terfenol-D of 3 to 10. This implies that the linear magnetostrictive actuator position can be inferred if we can detect the change in coils' inductances.
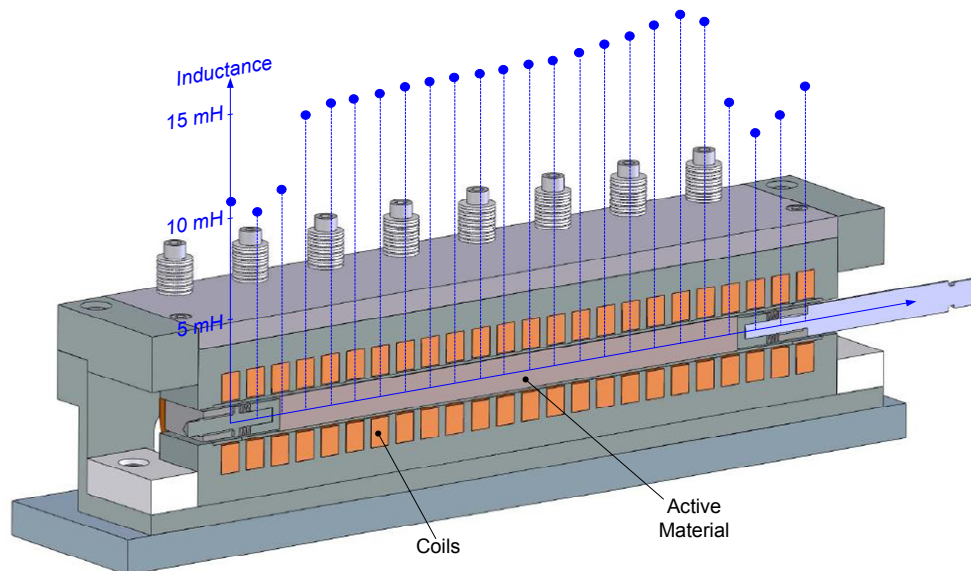


Fig. 6.1. The coils' inductance-measurement results with the active element placed in a predefined position illustrate the fundamental relationship between the motor position and its magnetic characteristics.

The equivalent circuit for a single coil is shown in Fig. 6.2. The terminal voltage for a single coil is written as

$$V = Ri + \frac{d\lambda}{dt}$$

(6.1)

where $R$ is the coil resistance and $\lambda$ is the flux linkage of the magnetic circuit. Since the flux linkage is a function of the coil current and the rotor position, we may rewrite the equation as

$$V = Ri + \frac{\partial\lambda}{\partial i}\frac{di}{dt} + \frac{\partial\lambda}{\partial x}\frac{dx}{dt}$$

(6.2)

where the second and third terms are the transformer voltage and the speed voltage, respectively [38]. Equation (6.2) is rearranged as an expression for the rate of change of the coil current

$$\frac{di}{dt} = \frac{V - Ri - \frac{\partial\lambda}{\partial x}\frac{dx}{dt}}{\frac{\partial\lambda}{\partial i}}.$$

(6.3)

Considering the low speed of the linear magnetostrictive actuator (0.15 mm/s), the speed voltage term can be neglected. In addition, by assuming the system to be an electrically linear system, the flux linkage can be described as

$$\lambda = L(x)i$$

(6.4)

thus,

$$\frac{di}{dt} \approx \frac{V - Ri}{L(x)}.$$

(6.5)

Since the generalized inductance of a coil is a function of position, the rate of change of the coil current is also a function of position.
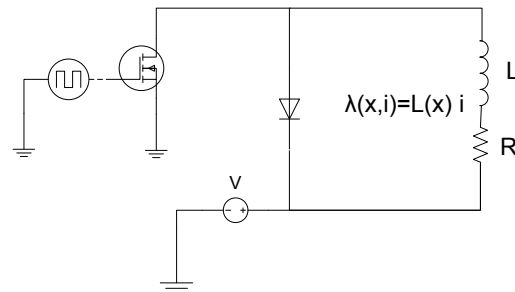
Fig. 6.2. Equivalent circuit of one coil.

The responses of the two coils with different inductance values to a pulse voltage input are shown in Fig. 6.3. As it is seen, by increasing the coil's inductance from 10 mH to 16 mH, the current response pulse width rises from 0.020 s to 0.035 s. Thus, the current-response pulse width can be considered as a representation of magnetic characteristics of the linear magnetostrictive actuator. Hence the fundamental relationship will consist of a relationship between the coils' current pulse width and the motor position.
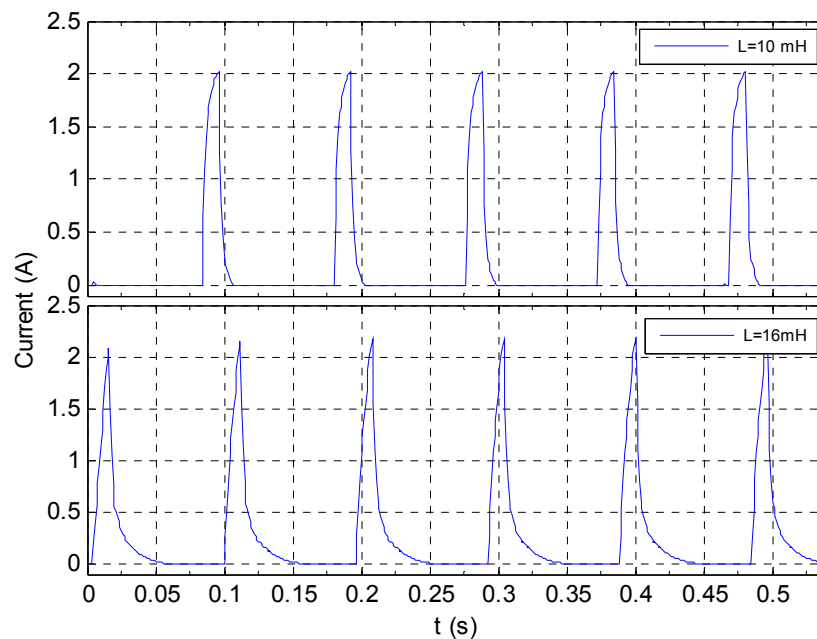


Fig. 6.3.  Actual current in actuator coils with inductances of 10 mH and 16 mH.

To find this fundamental relationship, we changed the active element's position from 15 mm to 40 mm and the current pulse widths of the coils #3, 4, and 5 were recorded with 1-mm increments. To measure the coil current we used Hall-effect-based transducers (model LA 03-PB from LEM). The results are depicted in Fig. 6.4.
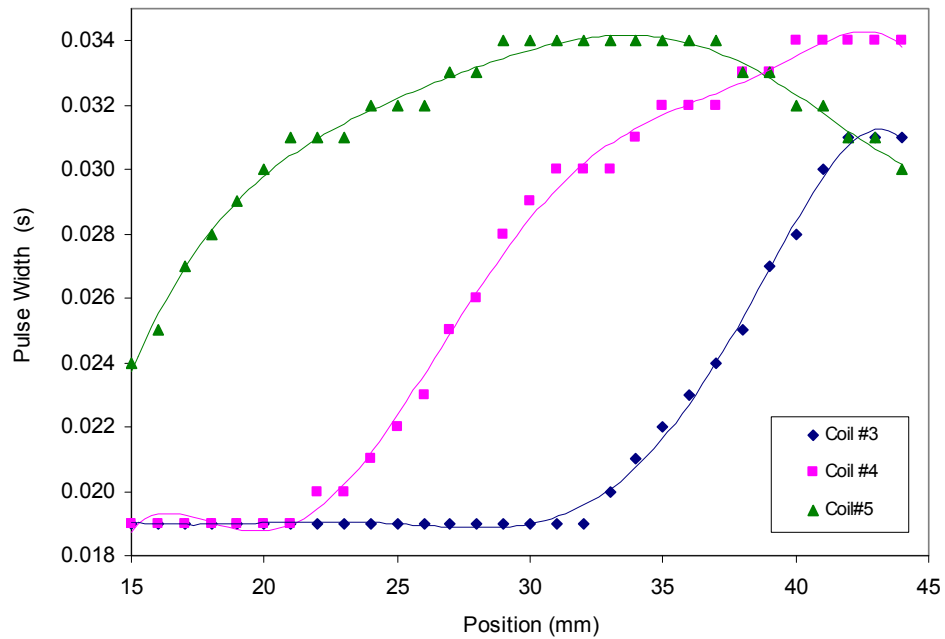


Fig. 6.4. The recorded current-response pulse widths for three coils when the active element's position changes from 15 mm to 45 mm.

For each pulse-width curve as shown in Fig. 6.4, there are three regions. The first is the low magnitude region with the pulse width around 0.020 s (Region I). This region corresponds to the time when the active element is not inside the coil yet. Then there is an increasing region which starts from the time the active element begins entering the coil until it is completely through the coil (Region II).

Finally each curve saturates at the pulse width around 0.032 s, which corresponds to the time when the active element is completely through the coil (Region III). These three regions for one coil are shown in Fig. 6.5.

To derive the fundamental relationship between the active element's position and the current response pulse widths, a linear curve was fitted to the linear region (Region II) of each curve. These three linear sections with corresponding equations are shown in Fig. 6.6.

The position calculation flowchart is shown in Fig. 6.7. The output voltages of current transducers are sent to the analog-to-digital (A/D) converters. The pulse widths of coils' current responses are measured and denoted by $t_3$, $t_4$, and $t_5$ in the flowchart. As shown in the flowchart, the algorithm detects the coil in Region II and then uses the corresponding linear equation to calculate the position.
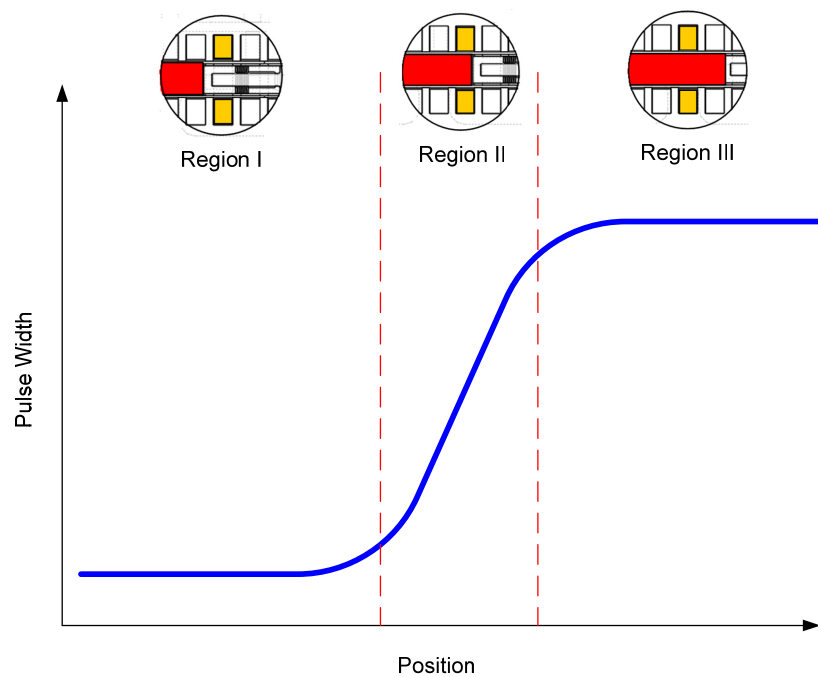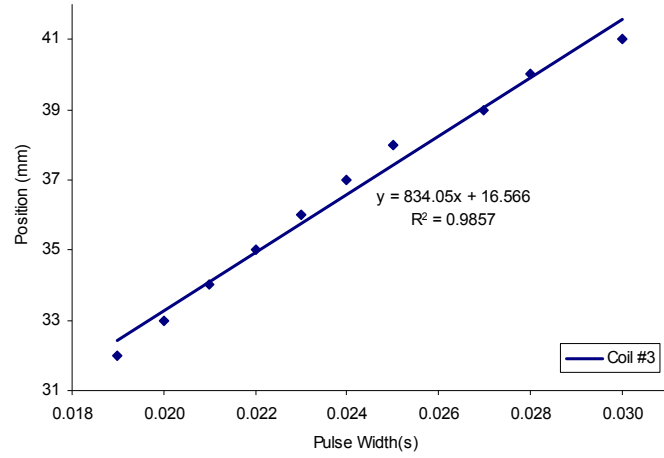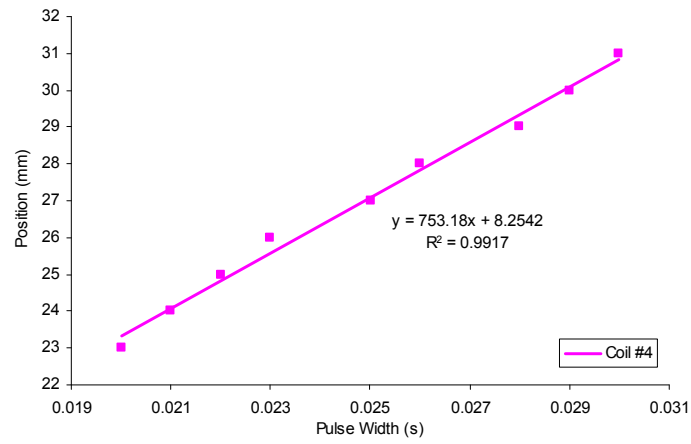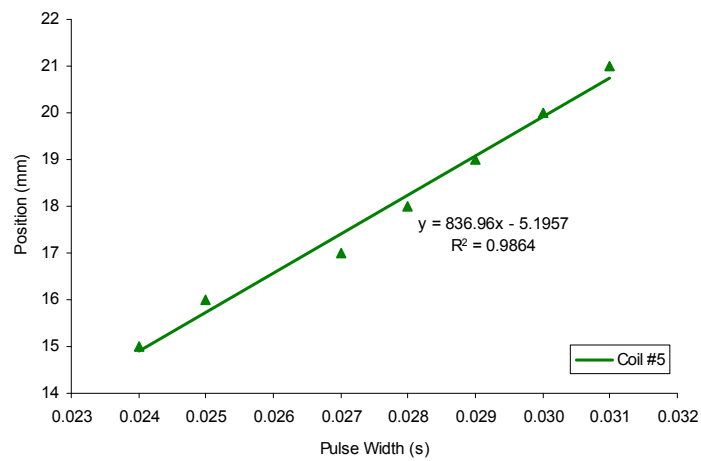


Fig. 6.5. Three regions of a current response pulse width versus position curve.

(a)



(b)



(c)

Fig. 6.6. Linear regions of coils and their corresponding equations of (a) coil #3 (b) coil #4 (c) coil #5.
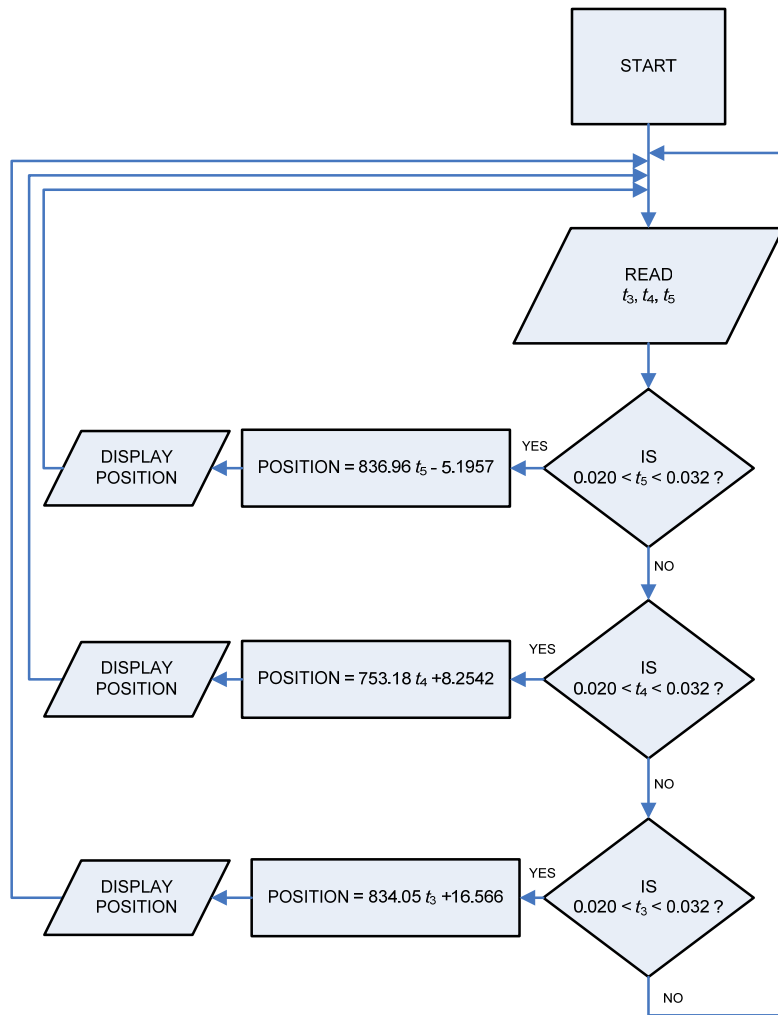
Fig. 6.7. Position estimation flowchart.

To verify the effectiveness of the proposed algorithm to infer the position, the motor position was changed and the measurement from a laser distance sensor was compared with the estimated position. The sensorless position measurement versus the laser distance sensor output and the error are depicted in Fig. 6.8. As it is seen, by employing this methodology we are able to infer the position of the linear magnetostrictive actuator with a ±1-mm maximum error. This error is partially due to the linear approximation we made earlier in developing

the relationship between the current response pulse width and the position. The other factor that contributes to the error in sensorless position calculation is that a minimum change in the active element's position should be made before a change in the current-response pulse width could be detected. The spikes in the inferred position are due to the errors in current sensing but do not much affect the closed-loop performance of the linear magnetostrictive actuator as we will see in the following section.

It was seen that sensorless position estimation was built based on the coil current pulse width measurements as shown in Fig. 6.4. Hence, the repeatability of these measurements play an important role in the effectiveness of the position estimation algorithm. To show the repeatability, three sets of measurements were performed and the results are shown in Fig. 6.9. It is seen that the results are quite repeatable and we may rely on them in estimating the position.
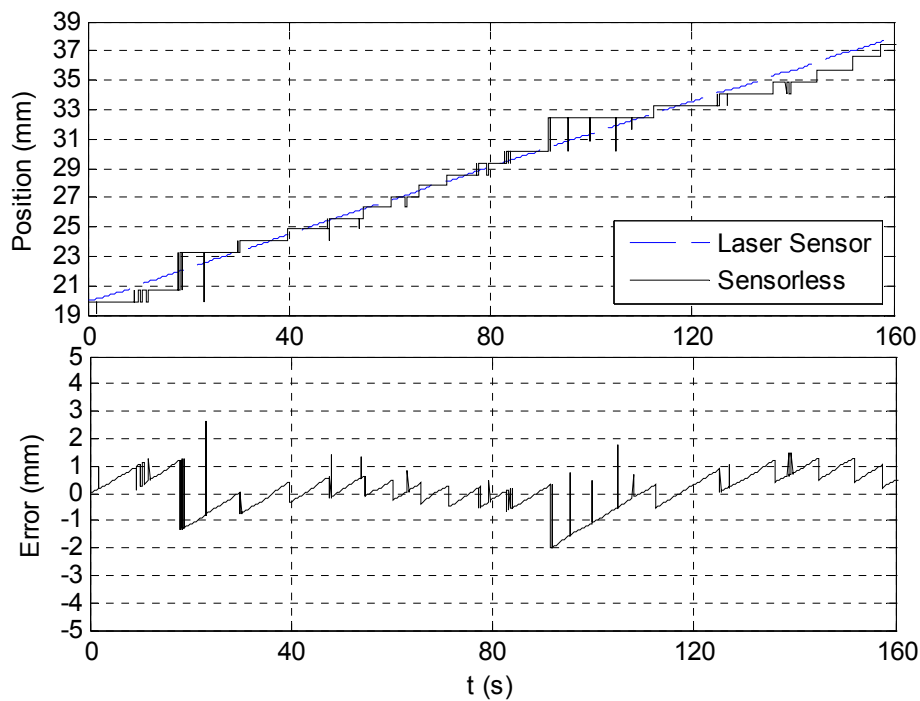


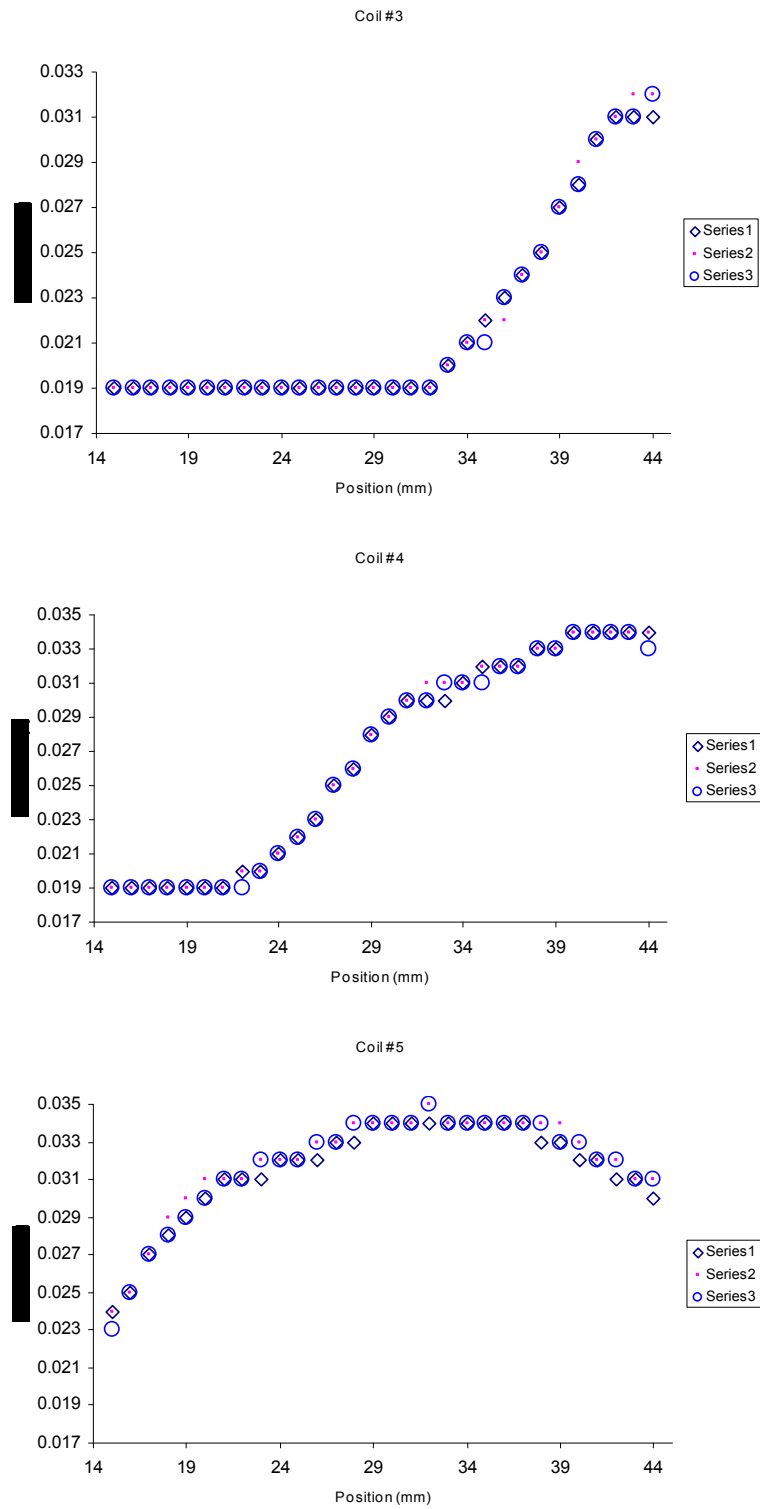Fig. 6.8. Sensorless position estimation error.

Fig. 6.9.  Three sets of current-response pulse widths measurements for coils #3, #4, and #5.

**6.2 Sensorless Closed-Loop Control**

Now the position-estimation algorithm could be used to implement the closed-loop control of the linear magnetostrictive actuator. The photograph of the test setup is shown in Fig. 6.10. The schematic diagram of control and instrumentation is shown in Fig. 6.11.

The coil currents are measured using Hall-effect-based current transducers, and the output voltages are sent to the A/D converters of the DSP board. Then the current pulse widths, $t_3$, $t_4$, and $t_5$ are calculated and sent to the position estimation algorithm. The estimated position is then fed back to a relay controller with a dead zone defined as:

$$u = \Phi(e) = \begin{cases} +1 & e > k_0 \\ 0 & -k_0 < e < k_0 \\ -1 & e < -k_0 \end{cases} \tag{6.6}$$

where, $\pm k_0$ defines the dead zone of the relay element. Since the precision of the position monitoring system is $\pm 1$ mm, a dead-zone threshold value of 1 mm should be picked to avoid the self oscillation [32]. The Simulink block diagram for calculating the current pulse widths and implementing the sensorless position estimation are shown in Figs. B.3–B.7.
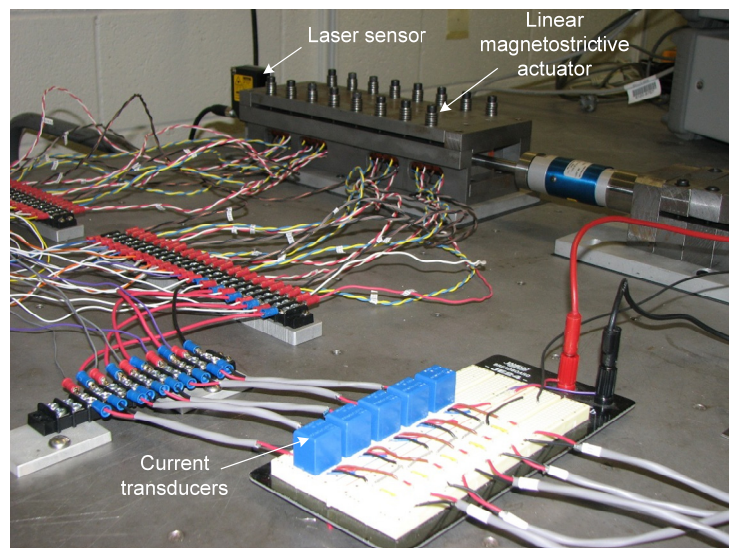


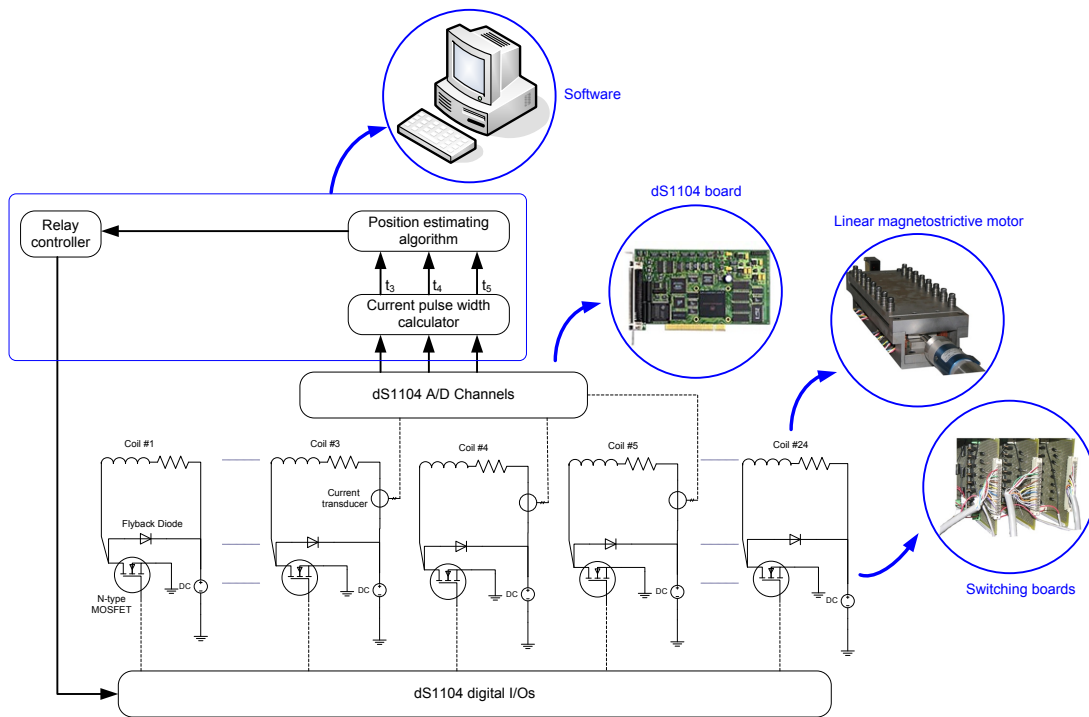Fig. 6.10. Photograph of the test setup.

Fig. 6.11. Schematic control and instrumentation diagram.

Fig. 6.12 depicts a 5-mm closed-loop step response of the linear magnetostrictive actuator with the sensorless position estimator. The steady-state error is only 0.65 mm which is within the ±1-mm maximum error boundary as expected. This relay-based controller is also robust to the spikes present in the estimated position as seen in Fig. 6.8. That lies in the fact that the spikes are of random nature and do not always appear in the same position where the motor operates.

Hence, although in some instances the error signal changes due to spikes, they not much affect the relay control signal output. This control output is always at maximum and makes the motor move in the desired direction at the maximum speed until it reaches the vicinity of the reference input as specified by the dead-zone threshold.

Fig. 6.13 shows the capability of the sensorless control system in tracking a sinusoidal reference input with amplitude of 5 mm and frequency of 0.015 rad/s.
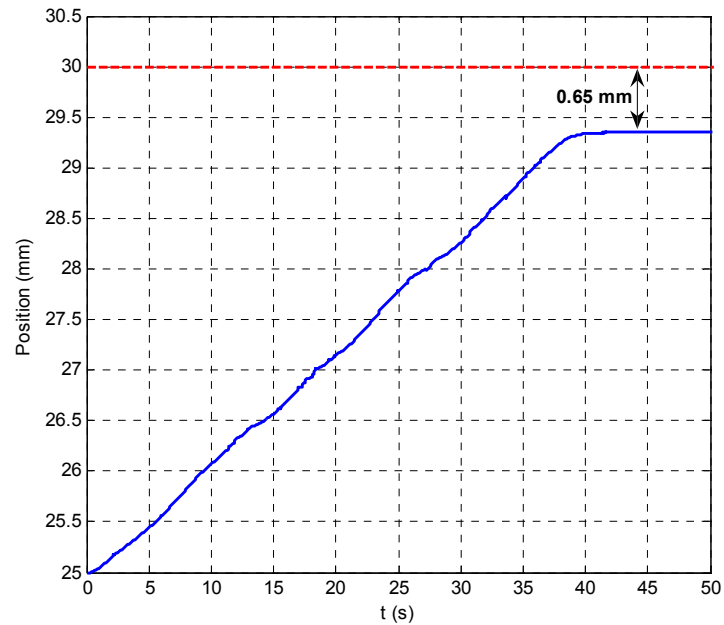


Fig. 6.12. 5-mm step response of the linear magnetostrictive actuator with sensorless control.
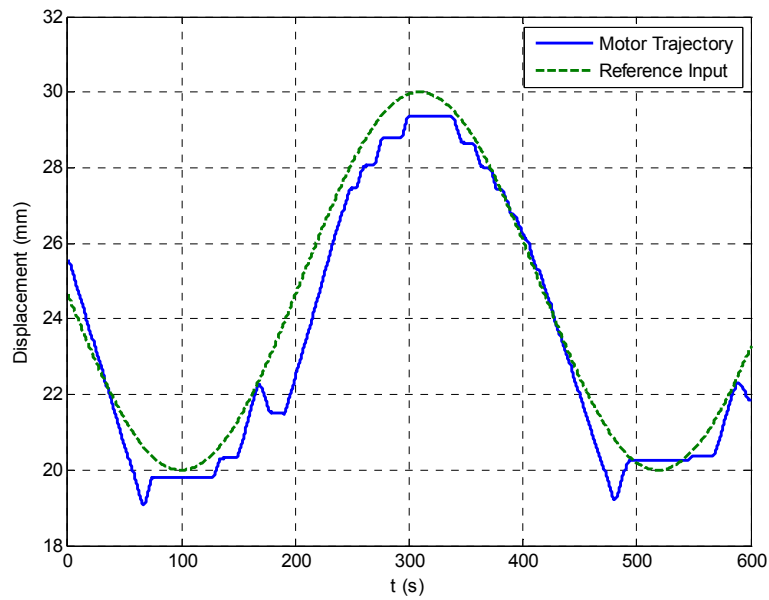


Fig. 6.13. Closed-loop response to a sinusoidal reference input with an amplitude of 5 mm and frequency of 0.015 rad/s.

**6.3 Application**

One of the potential applications of the linear magnetostrictive actuator is to actuate the sliding-sleeve valve (SSV) [39] which is used to establish or cut off the communication between the tubing and the annulus in an oil well [33]. A schematic drawing of sliding-sleeve valve is shown in Fig. 6.14.

By means of the linear magnetostrictive actuator, the sleeve could be shifted to open or close the ports machined in the body of the valve. Using the linear magnetostrictive actuator with sensorless control has two main benefits for this application. First, the power consumption of the motor is quite low and it self brakes when the power is cut off [20] which suit the power supply limitations in down-hole applications. Second, the sensorless position monitoring and control eliminates the need for using conventional sensors in harsh down-hole environment, which adds to the complexity and decreases the reliability of the actuation system.

In the SSV shown in Fig. 6.14, the sleeve can be shifted to five different levels ($L_1$ to $L_5$) to control the fluid flow from zero to maximum. Fig. 6.15 shows the trajectory of the linear magnetostrictive actuator with sensorless control to change the valve status from fully open to fully close. In all five levels the steady-state error is less than 1 mm. Since the distance between two adjacent ports, $\gamma$, is larger than 2 mm, the sleeve could be situated in the area between two ports using the sensorless position estimation.
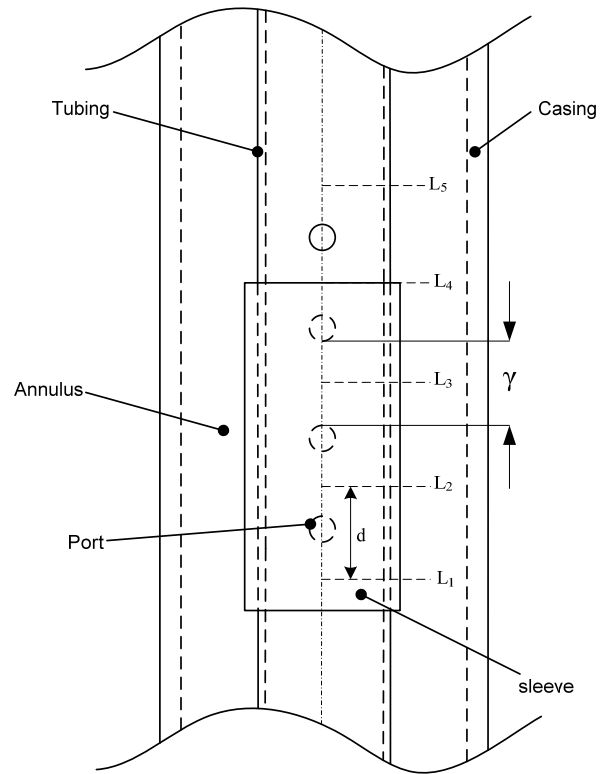
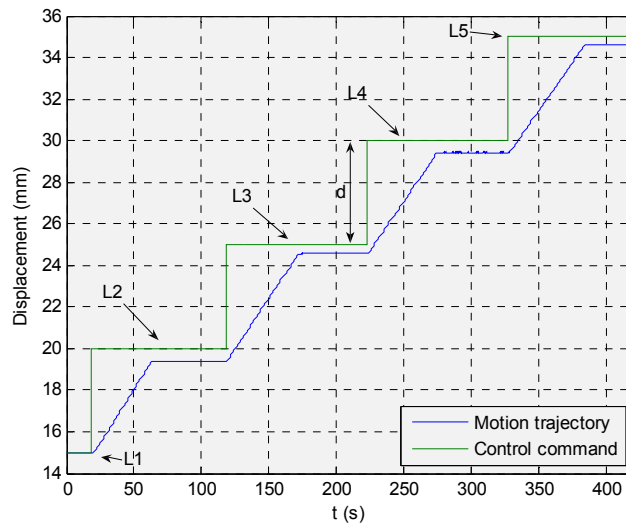Fig. 6.14. Schematic drawing of a sliding-sleeve valve.



Fig. 6.15. Control command to situate the SSV at $L_1$, $L_2$, $L_3$, $L_4$, and $L_5$, and the motor's actual motion trajectory.

## 6.4 Fuzzy-Based Sensorless Position Estimation

In the previous section we used a linear approximation of the fundamental relationship to estimate the position. To establish the fundamental relationship, a nonlinear mapping such as $\Psi$ from the current pulse widths of three coils to the position should be created such as

$$\Psi(t_3, t_4, t_5) = x \tag{6.7}$$

where $t_3$, $t_4$, and $t_5$ are the current pulse widths of coils #3, #4, and #5 respectively and $x$ is the position. As it is seen in Fig. 6.4, $\Psi(0.0225, 0.0322, 0.0341) = 36$ mm.

In search for a tool to model this nonlinear mapping, we face Fuzzy systems and neural networks which are among most popular intelligent systems [40]–[42]. Since fuzzy systems have the capability to approximate any continuous function [43], this allows the abovementioned nonlinear mapping to be modeled using a fuzzy model. Besides, fuzzy models are known for their robustness in the sense that they are less susceptible to changes in system parameters or noise [44]. If available, a mathematical model or a look-up table could also be used to create this mapping. However, the computation-intensive methods have the disadvantage of being slow and the look-up tables need a large memory size to achieve high accuracy, and interpolations would be also necessary [45].

### 6.4.1  Adaptive Neuro-Fuzzy Inference System (ANFIS)

ANFIS [46] is a class of adaptive networks that functions as a fuzzy inference system [47]. Since its advent, ANFIS has been extensively used in a wide variety of applications such as modeling, signal processing, and control [48]. In [49], ANFIS was employed to estimate the rotor position of a switched reluctance motor. In [50], the phase

inductance of a switched reluctance motor was estimated using ANFIS. However, it is the first time that ANFIS is employed to implement the sensorless position estimation of the linear magnetostrictive actuator.

In Fig. 6.16, ANFIS architecture for a simple Sugeno fuzzy model with two inputs $x_1$ and $x_2$ and one output f is shown. For this Sugeno fuzzy model, two fuzzy if-then rules are as the following.

Rule 1: If $x_1$ is $A_1$ and $x_2$ is $B_1$, then $f_1 = \alpha_1 x_1 + \beta_1 x_2 + \gamma_1$          (6.8)

Rule 2: If $x_1$ is $A_2$ and $x_2$ is $B_2$, then $f_2 = \alpha_2 x_1 + \beta_2 x_2 + \gamma_2$          (6.9)
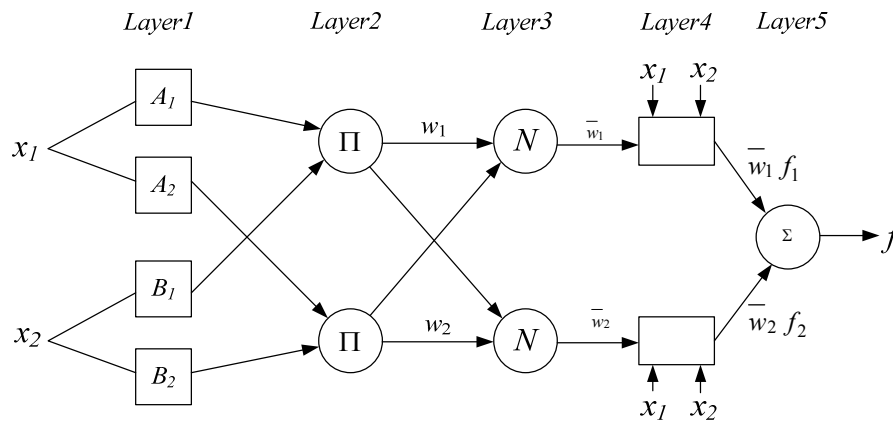


Fig. 6.16. Architecture of ANFIS for a fuzzy model with two inputs and one output [46].

Fuzzification of the inputs to the fuzzy model is performed in the first layer and the outputs would be the degree of membership of each of the inputs with respect to a fuzzy set. The outputs of the adaptive nodes in this layer could be described by

$$O_{1,i} = \mu_{A_i}(x_1) \qquad for\ i = 1,\ 2$$
$$O_{1,i} = \mu_{B_{i-2}}(x_2) \qquad for\ i = 3,\ 4$$

(6.10)

where $x_1$ and $x_2$ are the inputs to node $i$, and $A_i$ and $B_{i-2}$ are the fuzzy sets described by linguistic labels. The membership functions for $A_i$ or $B_{i-2}$ can be any appropriate parameterized ones such as the generalized bell (or Gaussian) membership function. In this paper, the Gaussian membership function is used which is given by

$$\mu_{A_i}(x) = e^{-\frac{(x-c_i)^2}{2\sigma_i^2}},$$

(6.11)

where $x$ is the input to fuzzy system, and $c_i$ and $\sigma_i$ are the parameters of the membership function and referred to as premise parameters.

The second layer determines the firing strength of each rule. Each node in this layer acts as a fuzzy AND operator. If the algebraic product is used for the AND operator, the node output in the second layer will be

$$O_{2,i} = w_i = \mu_{A_i}(x_1)\,\mu_{B_i}(x_2), \quad i = 1, 2.$$

(6.12)

Normalization of firing strengths calculated in Layer 3 is done in the fourth layer and the output of each node in this layer could be described by

$$O_{3,i} = \overline{w_i} = \frac{w_i}{w_1 + w_2}, \ i = 1, 2.$$

(6.13)

The output of the nodes in the fourth layer is a linear combination of the inputs multiplied by the normalized firing strength:

$$O_{4,i} = \overline{w_i} f_i = \overline{w_i}(\alpha_i x_1 + \beta_i x_2 + \gamma_i),$$

(6.14)

where $\{\alpha_i, \beta_i, \gamma_i\}$ are called the consequent parameters.

Finally the outputs of the fourth layer are added in the fifth layer to generate the output of the fuzzy system.

Identification of the premise and consequent parameters is carried out using a hybrid learning algorithm. It consists of two steps where first the consequent parameters are identified by the least-square method in the forward pass while keeping the premise parameters fixed. Then in the backward pass, the layer-two parameters are modified using gradient descent while the consequent parameters are held fixed.

### 6.4.2  Application of ANFIS for Sensorless Position Estimation

In this section, the ANFIS is employed to model the fundamental relationship between the current pulse widths and the actuator position. The first step in training the ANFIS is to collect the data. For this purpose, we used 30 sets of data which obtained earlier as shown in Fig. 6.4. The ANFIS architecture is illustrated in Fig. 6.17. There are three inputs to the ANFIS, $t_3$, $t_4$, and $t_5$, which are the current pulse widths of coils #3, #4 and #5. The input space of each variable was divided to three regions represented by three membership functions. Hence the number of rules in the fuzzy system will be 27. The Gaussian membership function was used for input variables which is specified by two variables as described by (6.11). Hence, the total number of parameters in the ANFIS which should be identified are 126, of which 18 ($9 \times 2$) are the premise parameters and 108 ($27 \times 4$) are the consequent parameters. The ANFIS training was performed using a hybrid optimization method, a combination of least-squares and backpropagation gradient descent method. The optimization process continues until the training error is less than the specified error tolerance or when the maximum number of epochs is reached. Here the error tolerance was set to zero to make sure that minimum error will be reached and the number of epochs was 100. In Fig. 6.18, membership functions for each input are depicted. In Fig. 6.19, the mapping surfaces of the ANFIS model are depicted.
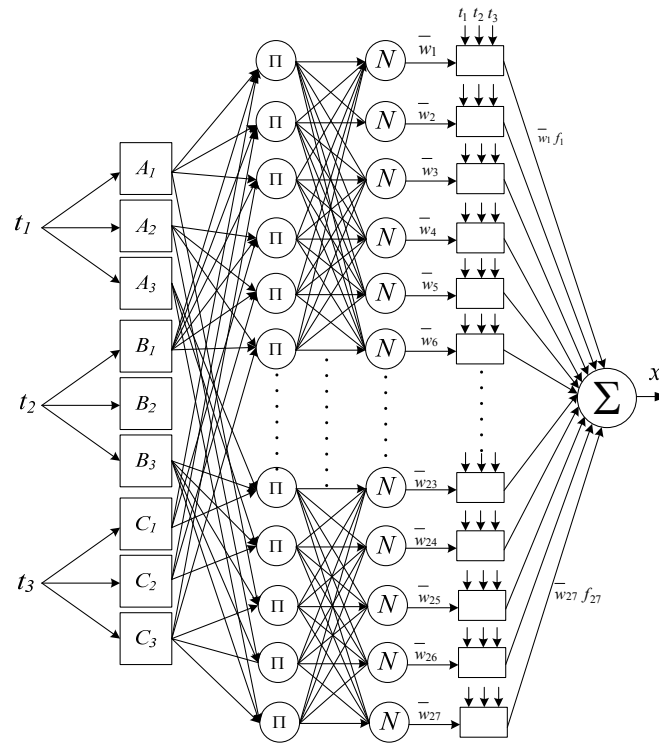
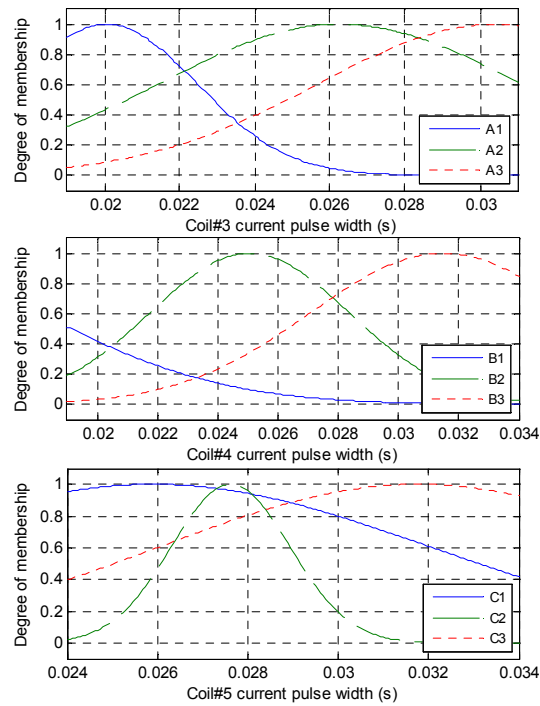Fig. 6.17. Proposed ANFIS architecture for position estimation.



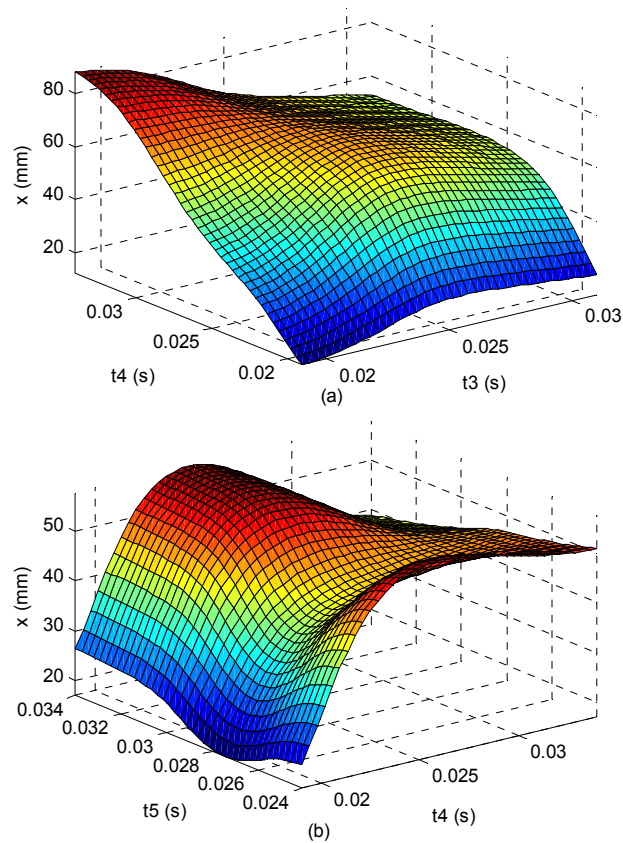Fig. 6.18. Membership functions for three inputs to the ANFIS.

Fig. 6.19. Mapping surface of ANFIS model for fundamental relationship when (a) $t_5 = 0.02$ s (b) $t_3 = 0.03$ s.

To verify the effectiveness of the ANFIS model to estimate the position, the actuator position was changed and the measurement from a laser distance sensor was compared with the ANFIS-based actuator position. The sensorless position measurement versus the laser distance sensor output and the error are depicted in Fig. 6.20. As it is seen by employing this methodology we are able to estimate the position of the linear magnetostrictive actuator with a ±0.5 mm maximum error. This error is due to the fact that a minimum change in the active element's position should be made before a change in the current response pulse width could be detected. The spikes in the ANFIS estimated position are due to the errors in current

sensing but do not affect the closed-loop performance of the linear magnetostrictive actuator as we will see in the following section.
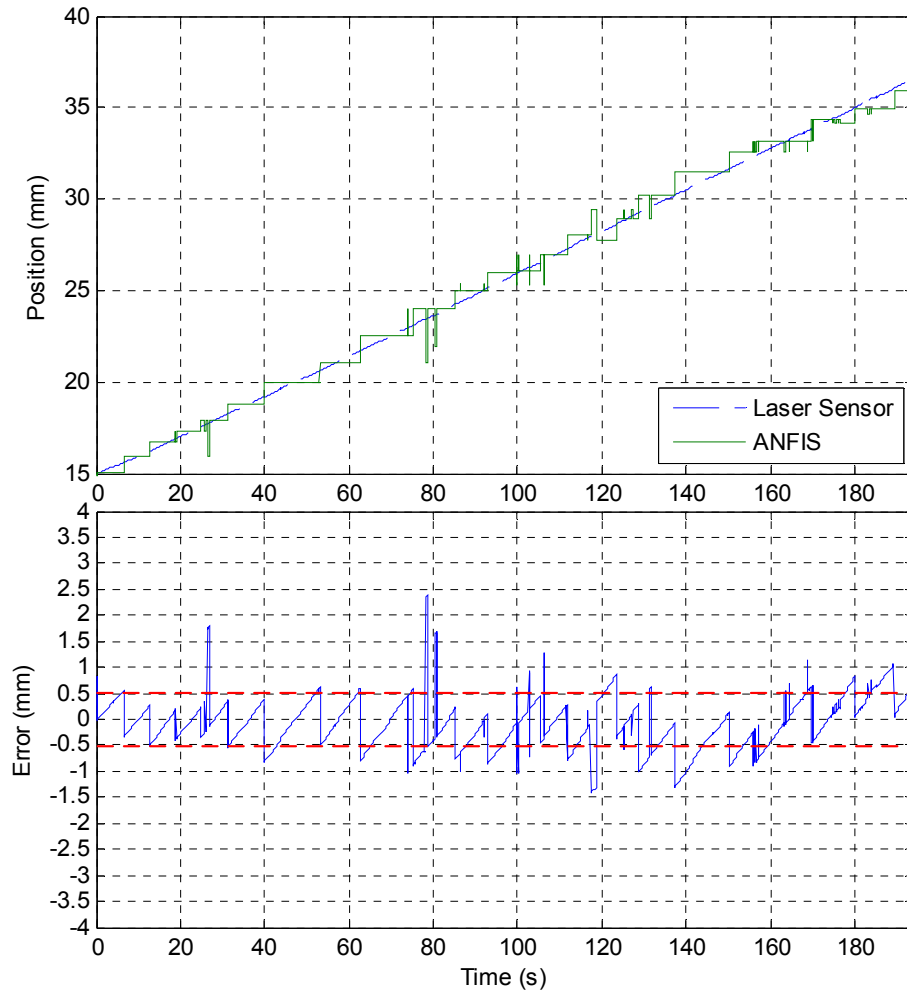


Fig. 6.20. Neuro-fuzzy based sensorless position estimation error.

### 6.4.3 Fuzzy-Based Sensorless Control

Now the ANFIS-based position estimation algorithm could be used to implement the closed-loop control of the linear magnetostrictive actuator. The schematic diagram of control and instrumentation is shown in Fig. 6.21.

Fig. 6.22 depicts a 5-mm closed-loop step response of the linear magnetostrictive actuator with the ANFIS-based position estimator. It is seen that the steady-state error is 0.1 mm which is within ±0.5 mm as expected. This relay-based controller is also robust to the spikes present in the estimated position. That lies in the fact that the spikes are of random nature and do not always appear in the same position where actuator is operating.

Hence, although in some instances the error signal changes due to spikes, this does not affect the control signal output from the relay controller which is always maximum and makes the actuator move in the desired direction at the maximum speed until it reaches the vicinity of reference input as specified by the dead-zone threshold. Fig. 6.23 shows the capability of the sensorless control system in tracking a square-wave reference input.
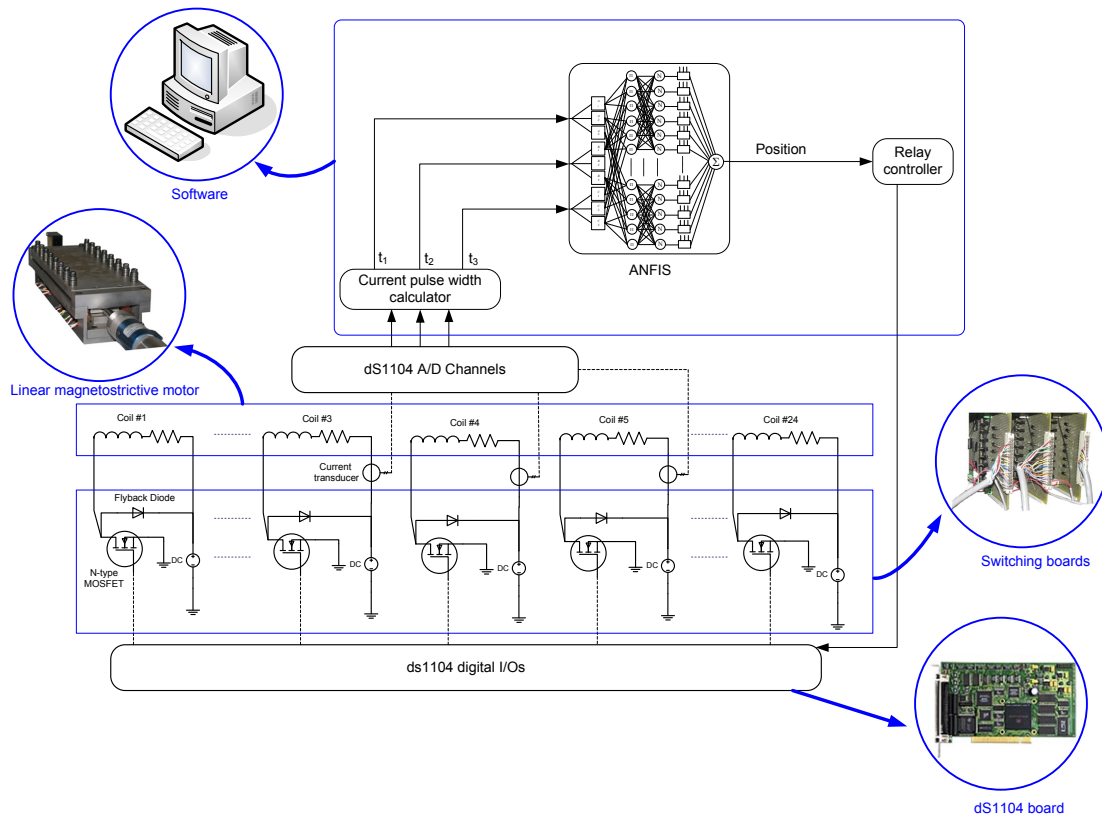


Fig. 6.21. Schematic control and instrumentation diagram.
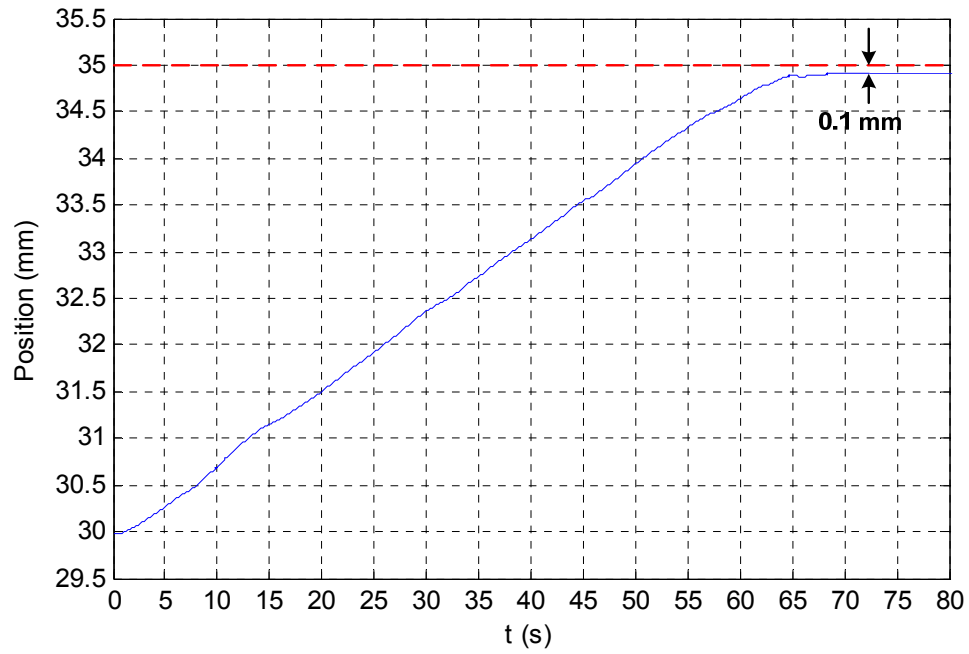
Fig. 6.22. 5-mm step response of the linear magnetostrictive actuator with ANFIS-based sensorless control.
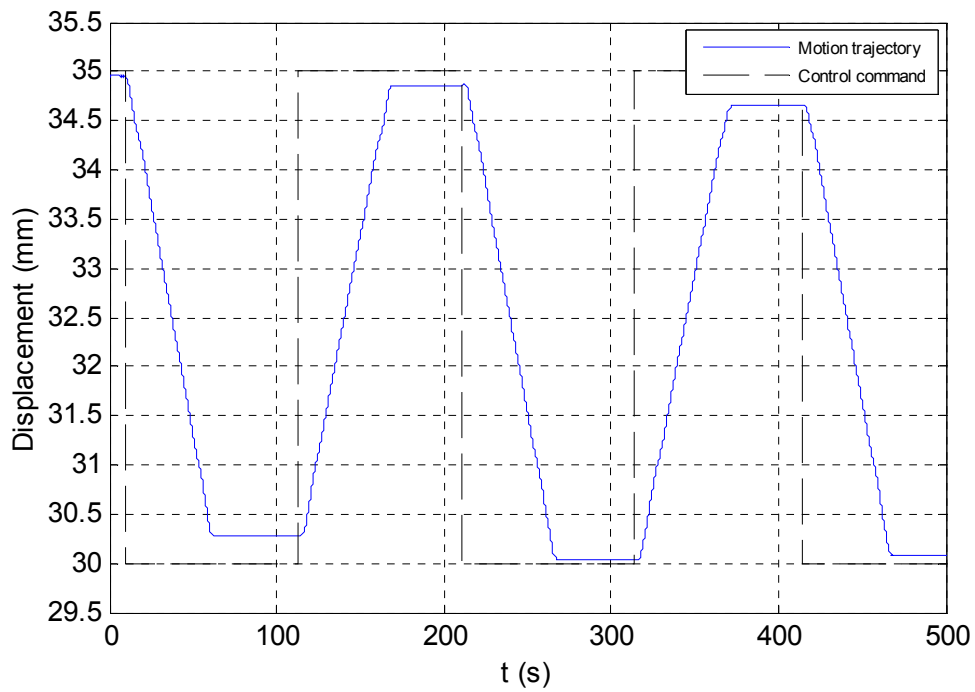


Fig. 6.23. Closed-loop response of the actuator to a square-wave control command.

# CHAPTER VII

# CONCLUSIONS AND SUGGESTIONS FOR FUTURE WORK

In this chapter the achievements of this research are summarized and suggestions for future work are provided to improve the performance of linear magnetostrictive actuator.

## 7.1 Conclusions

In response to the demand for new actuators in applications where conventional actuators face serious limitations, we successfully developed a novel low-power linear magnetostrictive actuator. The actuator design was chosen among five differenct configurations in conceptual design stage. FEA was extensively used to design and optimize its magnetic circuit. Our design allowed the flexibility to operate it in various configurations depending on the type of applications. A local three-phase operation mode was developed in response to the requirements in the applications where power consumption is a limiting factor. The power electronics was developed for this novel linear actuation system, and an effective relay-based controller was designed and implemented. The linear magnetostrictive actuator in the local three-phase operation mode demonstrated its force-generating capability of 410 N and travel range of 45 mm with power consumption of 95 W. The relay-based closed-loop control of the linear magnetostrictive actuator resulted in the positioning precision of 20 μm.

A novel sensorless control methodology was also successfully designed and implemented for this linear magnetostrictive actuator. First, the relationship between the inductance change in motor coils and the rotor position was measured. Based on this measurement with multiple sets of experiments, a fundamental relationship between the

coils' current-response pulse widths and the motor position was established. This fundamental relationship was modeled using two approaches. First, the fundamental relationship was approximated by linear equations and an algorithm was developed to estimate the position. The proposed method demonstrated a maximum position-estimation error band of $\pm 1$ mm. The sensorless closed-loop control of the linear magnetostrictive actuator was successfully performed by feeding the inferred position back to a relay controller. In the second approach, the fundamental relationship was modeled using adaptive neuro-fuzzy inference system. This method illustrated a position estimation capability of $\pm 0.5$ mm. Eventually, the closed-loop control of the linear magnetostrictive actuator was carried out by using the ANFIS-based estimated position.

The combination of the unique features of this class of actuator, i.e. self-braking and low-power consumption, combined with this newly-developed sensorless control scheme is a promising alternative in applications where conventional methods of actuation and sensing are proved incapable due to technical or reliability issues.

## 7.2 Suggestions for Future Work

Even though I tried to meet all objectives and in most of cases the actuator performance was satisfactory, there are still some aspects of this actuator which are remained unexplored. Based on that, I list the suggested future works as

- The unique design of this actuator gives us this flexibility to operate the actuator in various configurations. Nevertheless, the main focus of this research was on local-three phase excitation of the actuator. In future, other configurations can also be tried to reach the optimum operation mode of this actuator.

- In closed-loop control, I designed a relay controller which was effective in meeting our requirements but it might not be suitable for application in which nano-scale positioning is required. To improve the positioning accuracy, more advanced control techniques can be employed.

- For modeling, I presented an FE model of the actuator using ATILA and also an empirical model was developed based on the numerous tests I performed on the actuator. Nevertheless, presence of friction forces in the actuator makes it behave in a highly nonlinear way. More comprehensive models containing the nonlinearities present in the system could lead to higher-performance designs in the development of a next-generation actuator.

# REFERENCES

[1] H. Son and K.-M. Lee, "Distributed multipole models for design and control of PM actuators and sensors," *IEEE Trans. Mechatronics*, vol. 13, no. 2, pp. 228–238, April 2008.

[2] P. Karutz, T. Nussbaumer, W. Gruber, and J. W. Kolar, "Novel magnetically levitated two-level motor," *IEEE Trans. Mechatronics*, vol. 13, no. 6, pp. 658–668, Dec. 2008.

[3] M. Ataka, B. Legrand, L. Buchaillot, D. Collard, and H. Fujita, "Design, fabrication, and operation of two-dimensional conveyance system with ciliary actuator arrays," *IEEE Trans. Mechatronics*, vol. 14, no. 1, pp. 119–125, Feb. 2009.

[4] R. Merry, N. de Kleijn, M. van de Molengraft, and M. Steinbuch, "Using a walking piezo actuator to drive and control a high-precision stage," *IEEE Trans. Mechatronics*, vol. 14, no. 1, pp. 21–31, Feb. 2009.

[5] E. Steltz and R. S. Fearing, "Dynamometer power output measurements of miniature piezoelectric actuators," *IEEE Trans. Mechatronics*, vol. 14, no. 1, pp. 1–10, Feb. 2009.

[6] F. Claeyssen, N. Lhermet, and T. Maillard, "Magnetostrictive actuators compared to piezoelectric actuators," in *Proc. SPIE Conf. Smart Structures in Engineering and Technology*, 2003, vol. 4763, pp. 194–200.

[7] R. H. Bishop, *The Mechatronics Handbook*. Boca Raton, FL: CRC Press, 2002.

[8] Johnson Electric Inc. (2010), [Online]. Available: http://www.johnsonelectric.com

[9] K. Uchino, *FEM and Micromechatronics with ATILA Software*. Boca Raton, FL: CRC Press, 2008.

[10] F. Claeyssen, N. Lhermet, and G. Grosso, "Giant magnetostrictive alloy actuators," *J. Applied Electromagnetics in Materials*, vol. 5, pp. 67–73, 1994.
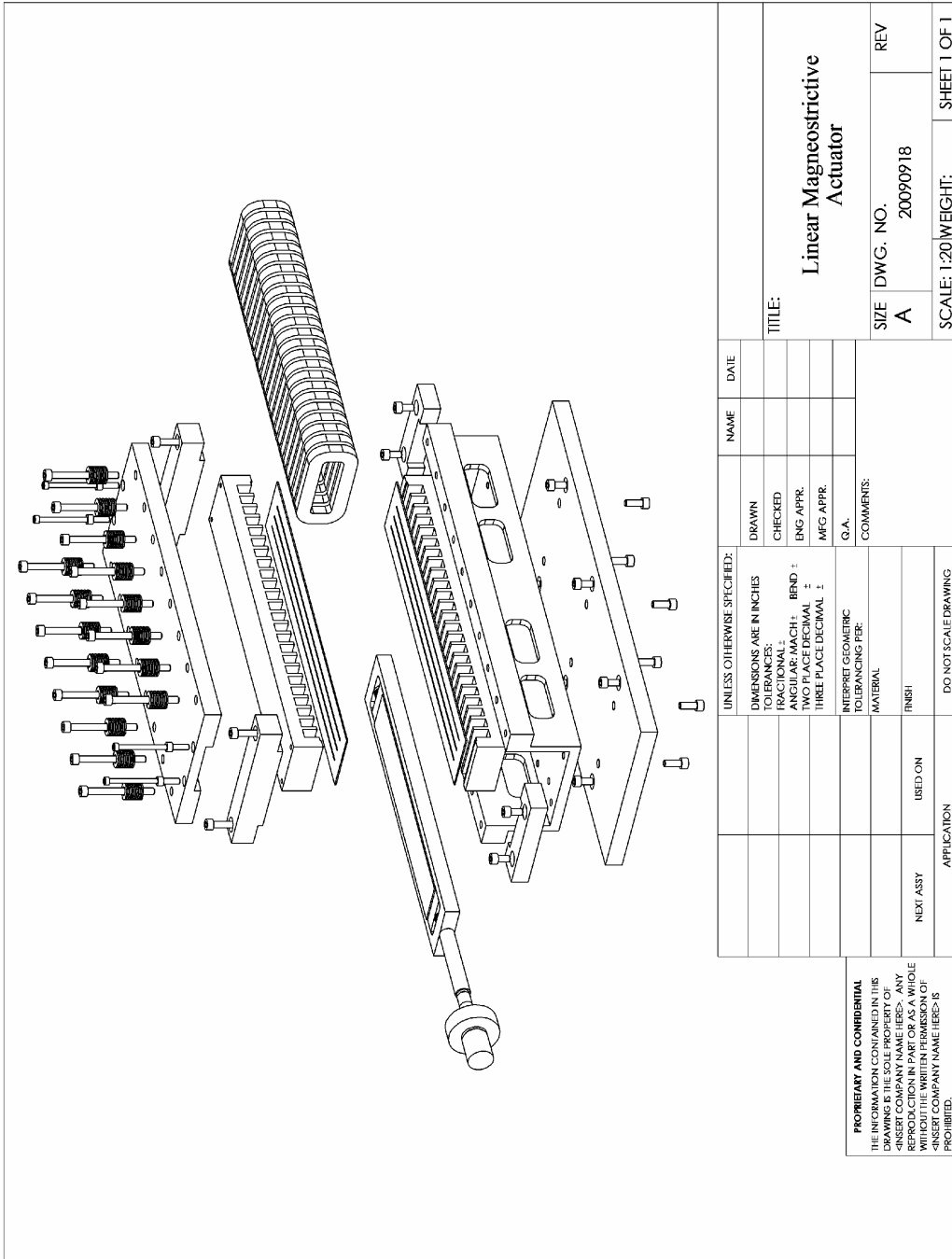
[11]  F. Claeyssen, N. Lhermet, R. L. Letty, and P. Bouchilloux, "Actuators, transducers and motors based on giant magnetostrictive materials," *J. Alloys and Compounds*, vol. 258, pp. 61–73, Aug. 1997.

[12]  J. Goldie, M. J. Gerver, J. Oleksy, G. P. Carman, and T. A. Duenas, "Composite Terfenol-D sonar transducers," in *Proc. SPIE Conf. Smart Materials Technologies*, Mar. 1999, vol. 3675, pp. 223–234.

[13]  L. Kvarnsjo, "Underwater acoustic transducers based on Terfnenol-D," *J. Alloys and Compounds*, vol. 258, pp. 123–125, Aug. 1997.

[14]  L. Kiesewetter, "The application of Terfenol in linear motors," in *Proc. 2$^{nd}$ Int. Conf. Giant Magnetostrictive Alloys*, 1988, ch. 7, p. 15.

[15]  W.-J. Kim, J. H. Goldie, M. J. Gerver, J. E. Kiley, and J. R. Swenbeck, "Extended-range linear magnetostrictive motor with double-sided three-phase stators," *IEEE Trans. Industry Applications*, vol. 38, no. 3, pp. 651–659, June 2002.

[16]  D. Kendall, and A. R. Piercy, "The frequency dependence of eddy current losses in Terfenol-D," *J. Applied Physics*, vol. 73, pp. 6174–6176, May 1993.

[17]  Ansoft LLC (2010), [Online]. Available: http://www.ansoft.com

[18]  ETREMA Products Inc. (2010), [Online]. Available: http://www.etrema-usa.com

[19]  J. E. Shigley, *Mechanical Engineering Design.* New York: McGraw-Hill, 1986.

[20]  W.-J. Kim and A. Sadighi, "A novel low-power linear magnetostrictive actuator with local three-phase excitation," *IEEE Trans. Mechatronics*, vol. 15, no. 2, pp. 299–307, Apr. 2010.

[21]  Ed Fagan Inc. (2010), [Online]. Available: http://www.edfagan.com

[22]  Wire Winders Inc. (2010), [Online]. Available: http://wirewinders.com

[23]    W.-J. Kim and A. Sadighi, "Design and relay-based control of a novel linear magnetostrictive motor," in *Proc. American Control Conf.*, June 2009, St. Louis, MO, pp. 3482–3487.

[24]    dSPACE Inc. (2010), [Online]. Available: http://www.dspaceinc.com

[25]    Baumer Inc. (2010), [Online]. Available: http://www.baumerelectric.com

[26]    Futek Advanced Sensor Technology Inc. (2010), [Online]. Available: http://www.futek.com

[27]    G. Engdahl, *Handbook of Giant Magnetostrictive Materials.* San Diego, CA: Academic Press, 2000.

[28]    F. Claeyssen, R. Le Letty, N. Lhermet, R. Bossut, and B. Hamonic, "Analysis of magnetostrictive inchworm motors using finite element modeling," in *Proc. Elsevier Conference Magnetoelastic Effects and Applications*, 1993, pp. 161–167.

[29]    International Center for Numerical Methods in Engineering (2010), [Online]. Available: http://gid.cimne.upc.es

[30]    A. Sadighi and W.-J. Kim, "Sensorless control of a novel linear magnetostrictive motor," in *Proc. IEEE Energy Conversion Congress and Exposition*, Sep. 2009, pp. 1726–1731.

[31]    W. Mei, T. Umeda, S. Zhou, and R. Wang, "Magnetostriction of grain-aligned $Tb_{0.3}Dy_{0.7}Fe_{1.95}$," *J. Alloys and Compounds*, vol. 224, pp. 76–80, June 1995.

[32]    Y. Z. Tsypkin, *Relay Control Systems.* Cambridge: Cambridge University Press, 1984.

[33]    D. Perrin, *Well Completion and Servicing*. Paris: Editions Technip, 1999.

[34]    K. Rajashekara, A. Kawamura, and K. Matsuse, *Sensorless Control of AC Motor Drives.* New York: IEEE Press, 1996.

[35]    T. J. E. Miller, *Electronic Control of Switched Reluctance Machines*. Woburn, MA: Reed Educational and Professional Publishing Ltd., 2001.

[36]    N. Ertugrul and P. Acarnley, "A new algorithm for sensorless operation of permanent magnet motors," *IEEE Trans. Industry Applications*, vol. 30, no. 1, pp. 126–133, Jan. 1994.

[37]    P. P. Acarnley, R. J. Hill, and C. W. Hooper, "Detection of rotor position in stepping and switched motors by monitoring of current waveforms," *IEEE Trans. Industrial Electronics*, vol. IE-32, no. 3, pp. 215–222, Aug. 1985.

[38]    H. H. Woodson and J. R. Melcher, *Electromechanical Dynamics*. New York: John Wiley & Sons, Inc., 1968.

[39]    A. P. Dorel, "Linear actuator using magnetostrictive power element," U.S. Patent Application 11/733905, May 15, 2008.

[40]    J. Huang, T. Fukuda, and T. Matsuno, "Model-based intelligent fault detection and diagnosis for mating electric connectors in robotic wiring harness assembly systems," *IEEE Trans. Mechatronics*, vol. 13, no. 1, pp. 86–94, Feb. 2008.

[41]    L. Yao and P.-Z. Huang, "Learning of hybrid fuzzy controller for the optical data storage device," *IEEE Trans. Mechatronics*, vol. 13, no. 1, pp. 3–13, Feb. 2008.

[42]    R.-E. Precup, S. Preitl, I. J. Rudas, M. L. Tomescu, and J. K. Tar, "Design and experiments for a class of fuzzy controlled servo systems," *IEEE Trans. Mechatronics*, vol. 13, no. 1, pp. 22–35, Feb. 2008.

[43]    L. X. Wang, "Fuzzy systems are universal approximators," in *Proc. IEEE Int. Conf. Fuzzy Systems*, CA, Mar. 1992, pp. 1163–1169.

[44]    E. H. Mamdani, "Twenty years of fuzzy control: Experience gained and lessons learnt," in *Proc. 2$^{nd}$ IEEE Int. Conf. Fuzzy Systems*, 1993, vol. 1, pp. 339–344.

[45]    B. K. Bose, "Expert system, fuzzy logic, and neural network applications in power electyronics and motion control," *Proc. IEEE*, Aug. 1994, vol. 82, no. 8, pp. 1303–1323.

[46]    J. S. R. Jang, "ANFIS: Adaptive-network-based fuzzy inference system," *IEEE Trans. Syst., Man, and Cybern.*, vol. 23, no. 3, pp. 665–685, May 1993.

[47]    J. S. R. Jang, C. T. Sun, and E. Mizutani, *Neuro-Fuzzy and Soft Computing*. Upper Saddle River, NJ: Prentice-Hall, 1997.

[48]    A. Ghaffari and A. Sadighi, "Design of a neuron-fuzzy controller for nonlinear systems," in *Proc. of the 6ᵗʰ IASTED Int. Conf. Intelligent Systems and Control*, June 2004, pp. 227–231.

[49]    A. D. Cheok and Z. Wang, "Fuzzy logic rotor position estimation based switched reluctance motor DSP drive with accuracy enhancement," *IEEE Trans. Power Electronics*, vol. 20, no. 4, pp. 908–921, July 2005.

[50]    F. Daldaban, N. Ustkoyuncu, and K. Guney, "Phase inductance estimation for switched reluctance motor using adaptive neuro-fuzzy inference system," *J. Energy Conversion & Management*, vol. 47, pp. 485–493, Mar. 2006.

**APPENDIX A**

**ENGINEERING DRAWINGS**

Fig. A.1. Exploded view of linear magnetostrictive actuator.
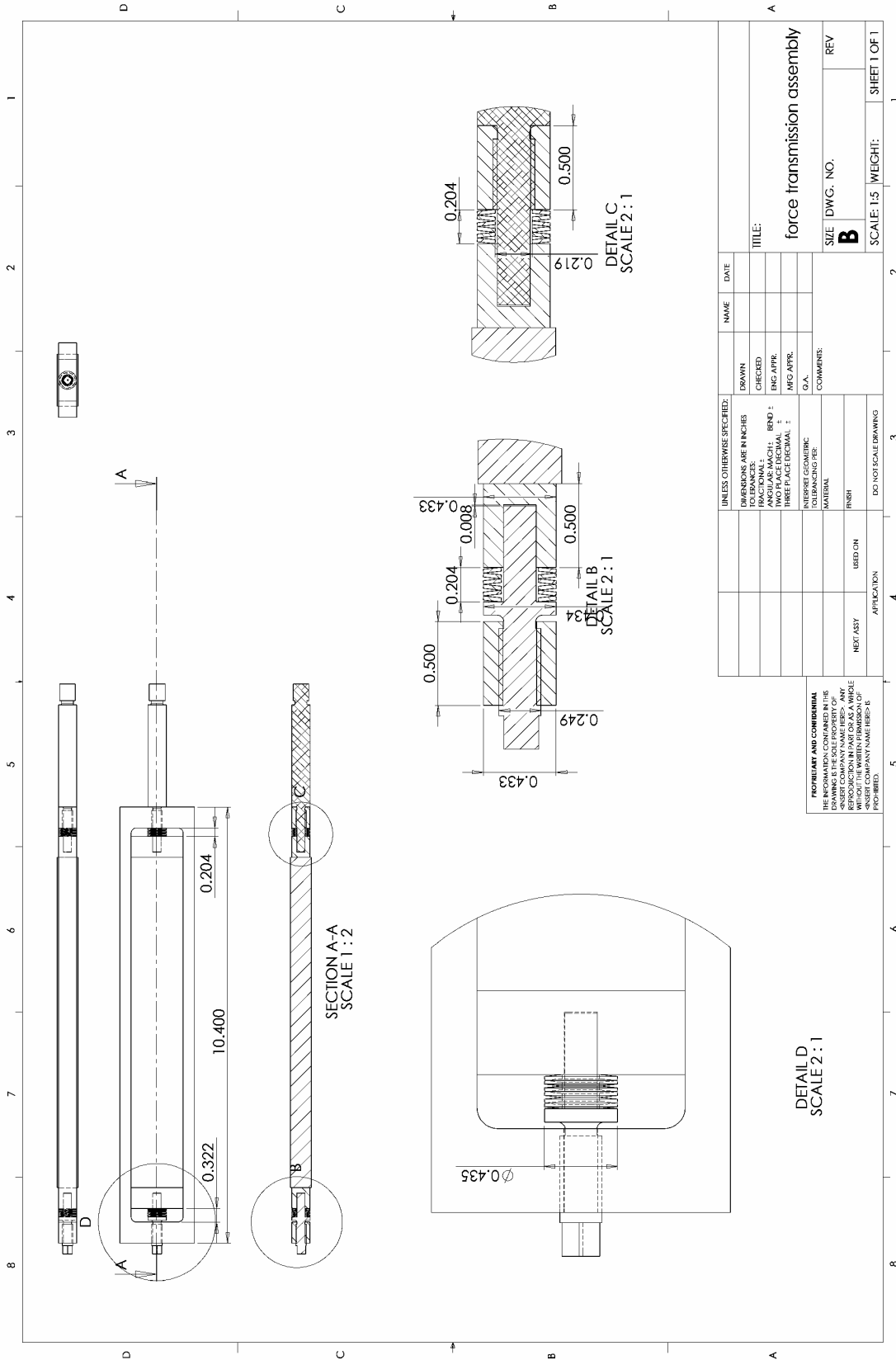
Fig. A.2. Exploded view of force transmission assembly.
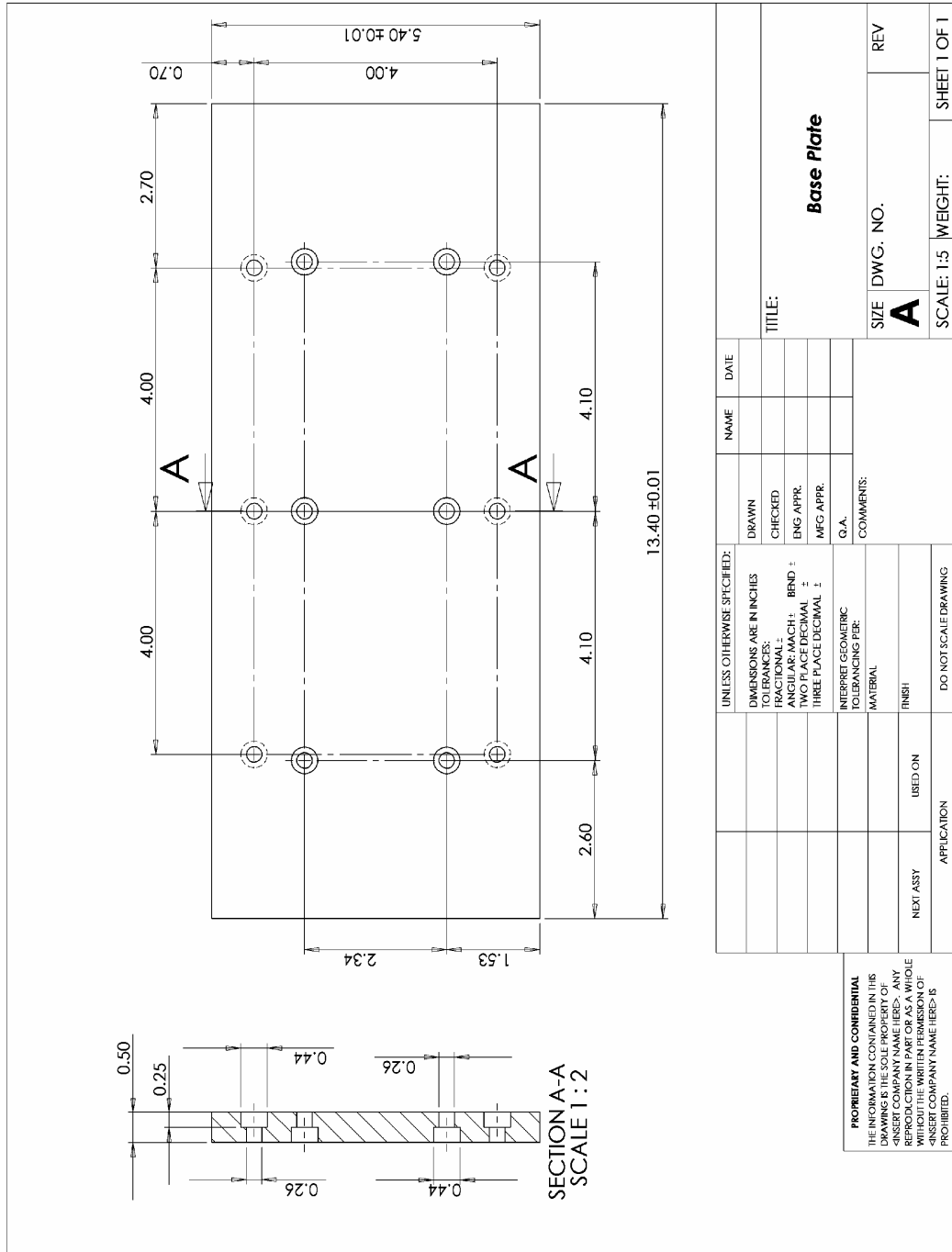
Fig. A.3. Base plate.

Fig. A.4. Carriage.

SECTION B-B
SCALE 2 : 1

0.41 0.00
+0.01

0.300 +0.001 -0.010

R0.120

B

B

0.00
2.08 -0.01

2.900

R0.530

0.63 -0.01
0.00

1.450
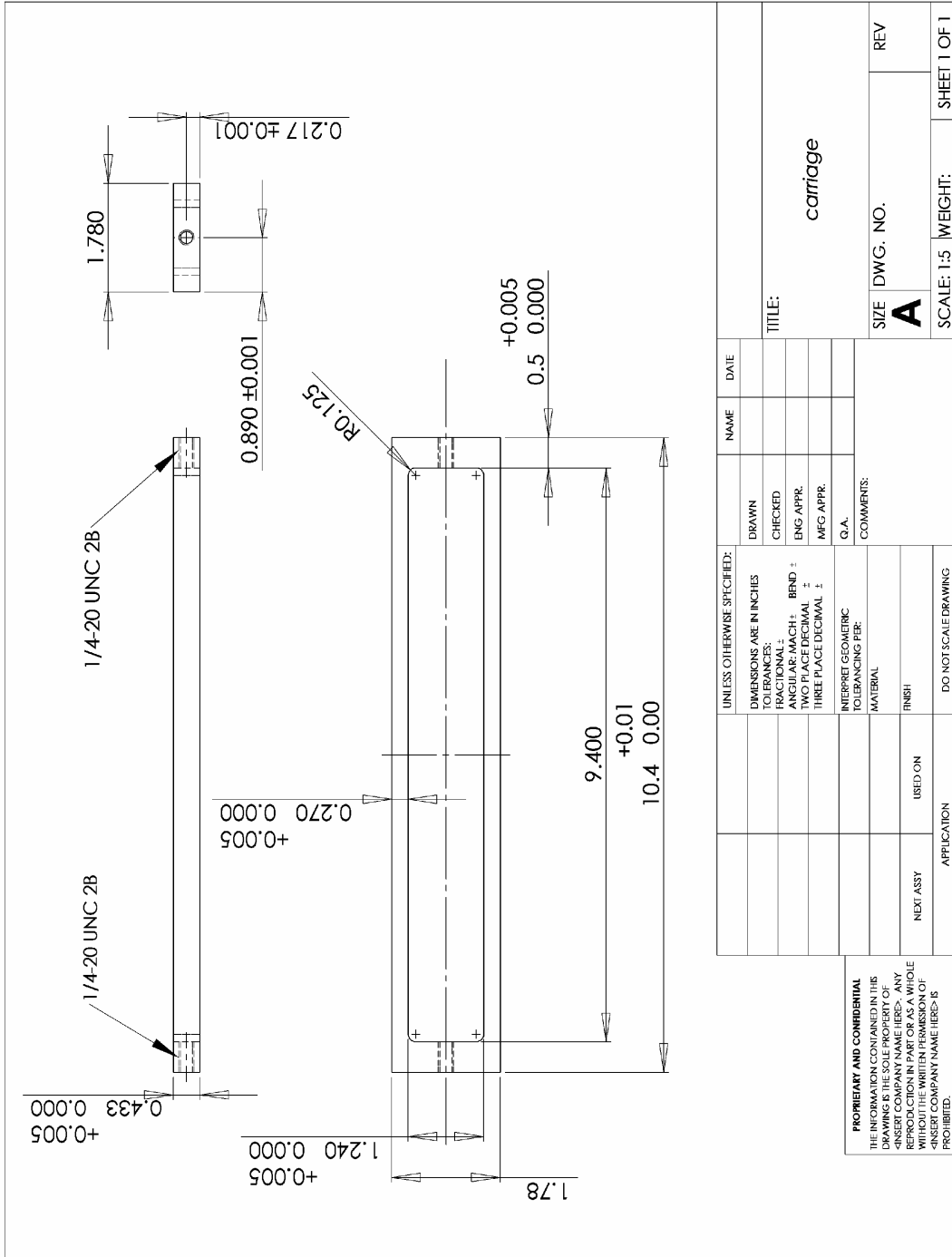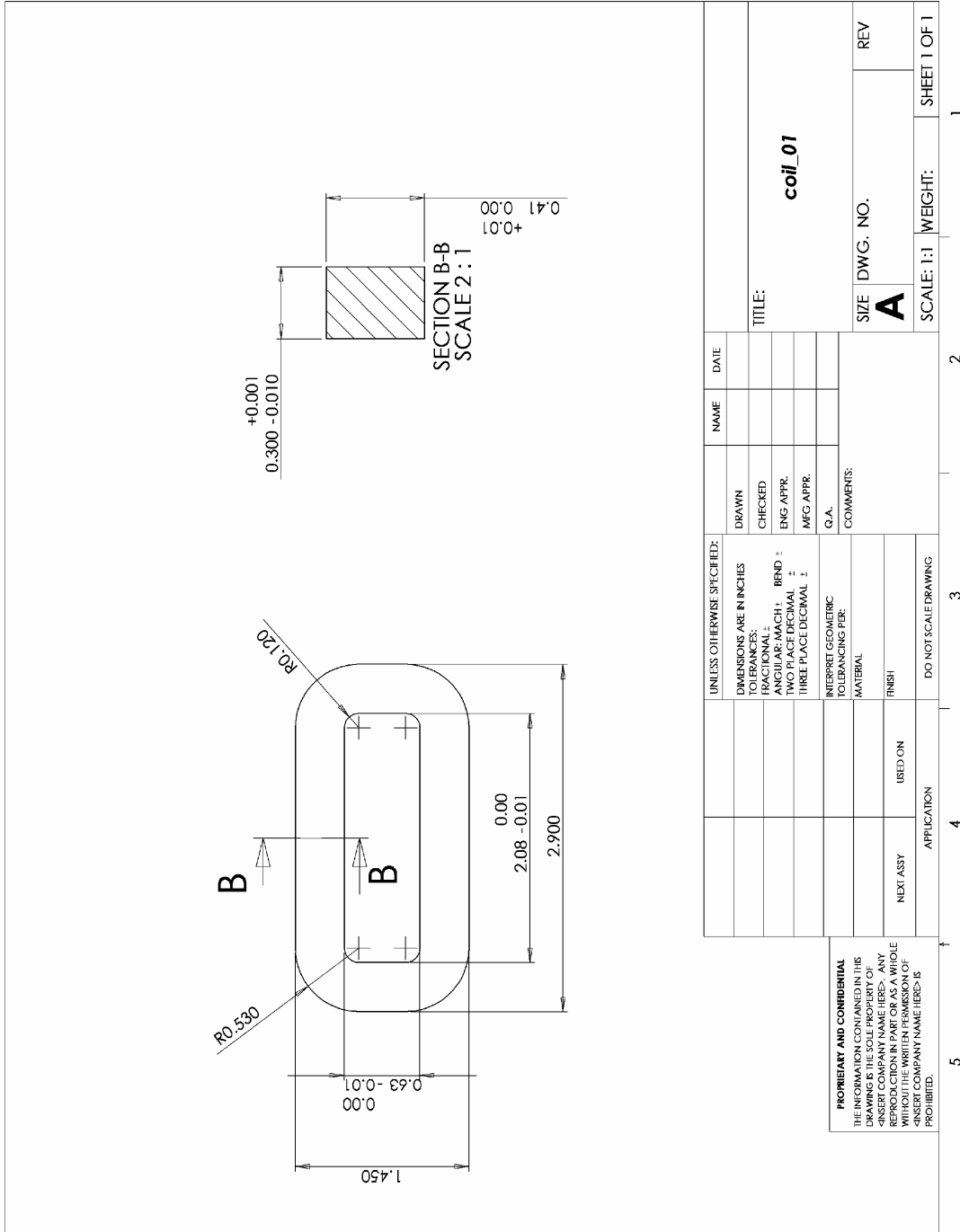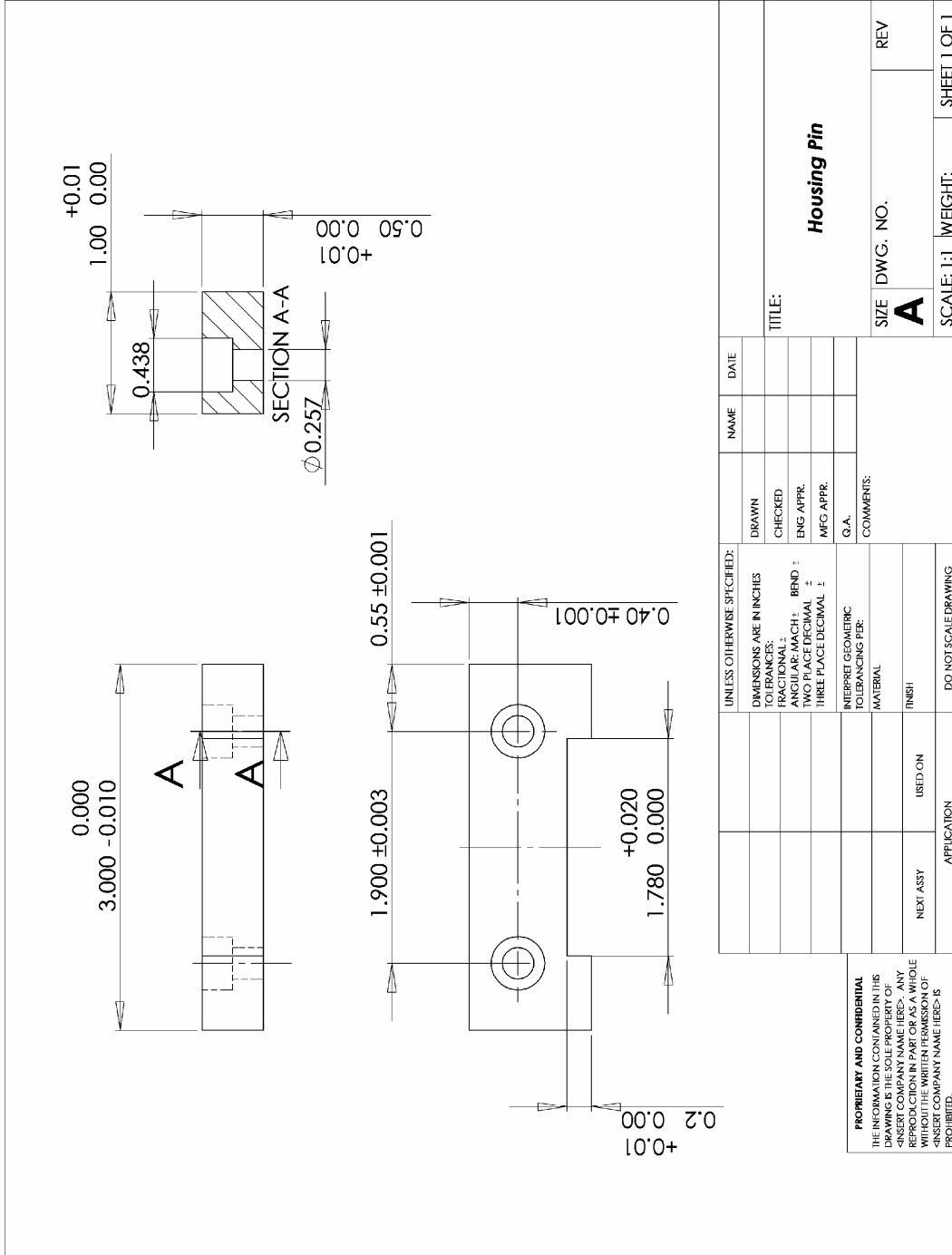
PROPRIETARY AND CONFIDENTIAL

THE INFORMATION CONTAINED IN THIS DRAWING IS THE SOLE PROPERTY OF <INSERT COMPANY NAME HERE>. ANY REPRODUCTION IN PART OR AS A WHOLE WITHOUT THE WRITTEN PERMISSION OF <INSERT COMPANY NAME HERE> IS PROHIBITED.

UNLESS OTHERWISE SPECIFIED:

DIMENSIONS ARE IN INCHES
TOLERANCES:
FRACTIONAL ±
ANGULAR: MACH ± BEND ±
TWO PLACE DECIMAL ±
THREE PLACE DECIMAL ±

INTERPRET GEOMETRIC
TOLERANCING PER:

MATERIAL

FINISH

DO NOT SCALE DRAWING

NAME DATE

DRAWN
CHECKED
ENG APPR.
MFG APPR.
Q.A.
COMMENTS:

TITLE:

coil_01

SIZE DWG. NO. REV
A

SCALE: 1:1 WEIGHT: SHEET 1 OF 1

NEXT ASSY USED ON
APPLICATION

5 4 3 2 1

Fig. A.5. Coil.

Fig. A.6. Housing pin.

Fig. A.7. Housing.

SECTION A-A
SCALE 1 : 2

Fig. A.8. Housing.

A

2.650
0.750
0.400
4.100
4.100
2.340
10.400
6.300
2.200
0.530
2.870

UNLESS OTHERWISE SPECIFIED:

DIMENSIONS ARE IN INCHES
TOLERANCES:
FRACTIONAL±
ANGULAR: MACH±   BEND ±
TWO PLACE DECIMAL   ±
THREE PLACE DECIMAL  ±

INTERPRET GEOMETRIC
TOLERANCING PER:

MATERIAL

FINISH

NAME   DATE

DRAWN
CHECKED
ENG APPR.
MFG APPR.
Q.A.
COMMENTS:

TITLE:

Housing_02

SIZE  DWG. NO.                REV
A

SCALE: 1:5  WEIGHT:   SHEET 1 OF 1

NEXT ASSY   USED ON
APPLICATION   DO NOT SCALE DRAWING

Fig. A.9. Inconel plate.

DETAIL E
SCALE 1 : 1

0.266
0.438
0.400 ±0.005

5.400 ±0.020
3.850 ±0.003
1.550 ±0.003
2.500 ±0.003
7.500 ±0.003
10.0 ±0.02
9.0 ±0.005
5.0 ±0.005
1.0 ±0.005
0.50 ±0.01
4.90 ±0.01

0.500
0.250
0.438
0.266
0.625
0.375
Ø0.386

E

UNLESS OTHERWISE SPECIFIED:

DIMENSIONS ARE IN INCHES
TOLERANCES:
FRACTIONAL ±
ANGULAR: MACH ±   BEND ±
TWO PLACE DECIMAL   ±
THREE PLACE DECIMAL   ±

INTERPRET GEOMETRIC
TOLERANCING PER:

MATERIAL

FINISH

DO NOT SCALE DRAWING

| | NAME | DATE |
|---|---|---|
| DRAWN | | |
| CHECKED | | |
| ENG APPR. | | |
| MFG APPR. | | |
| Q.A. | | |
| COMMENTS: | | |

TITLE:

load base plate

SIZE | DWG. NO. | REV
A
SCALE: 1:5 | WEIGHT: | SHEET 1 OF 1

NEXT ASSY | USED ON
APPLICATION

5   4   3   2   1

Fig. A.10. Load base plate.

Fig. A.11. Load interface.
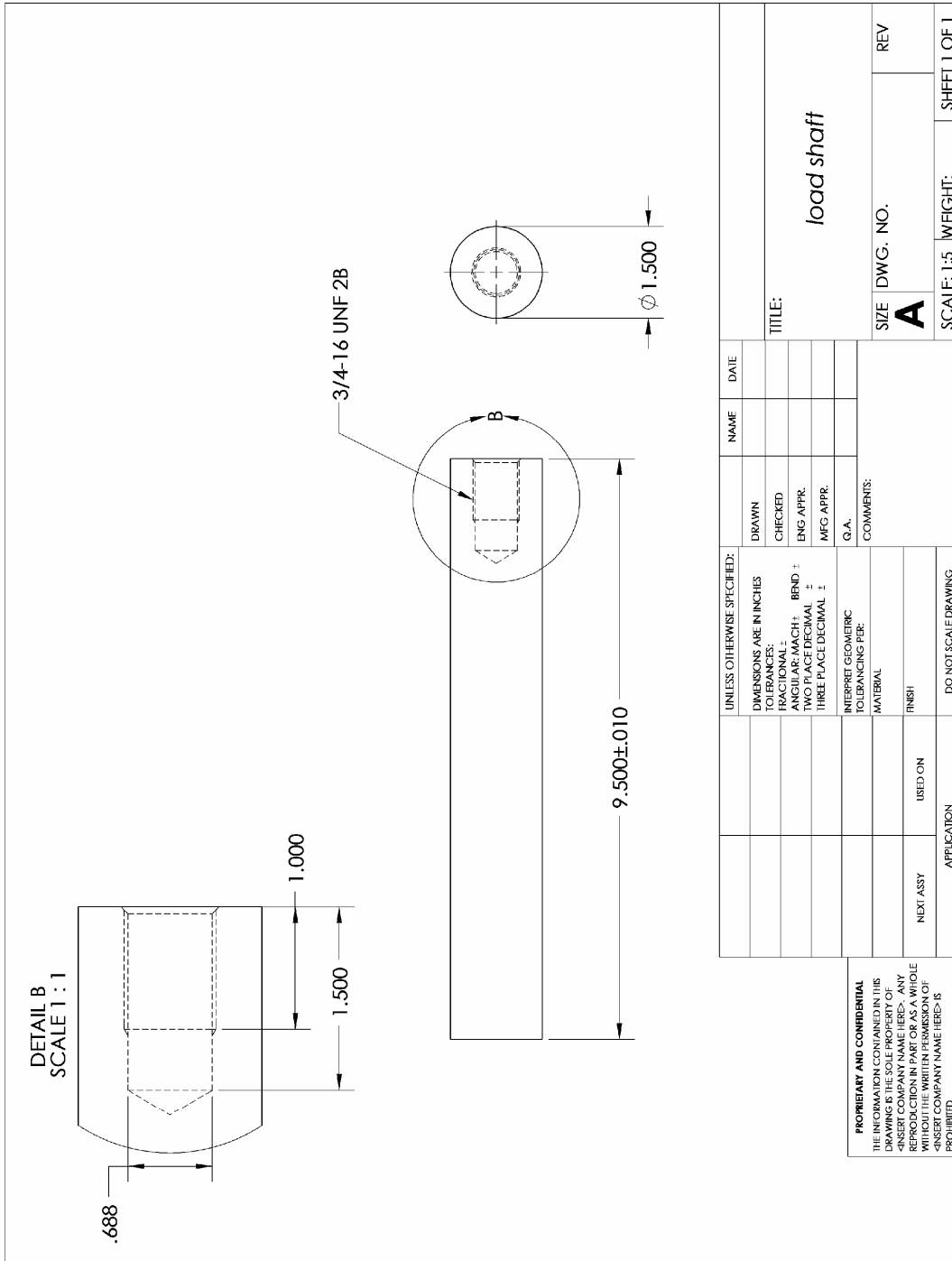
Fig. A.12. Load shaft.
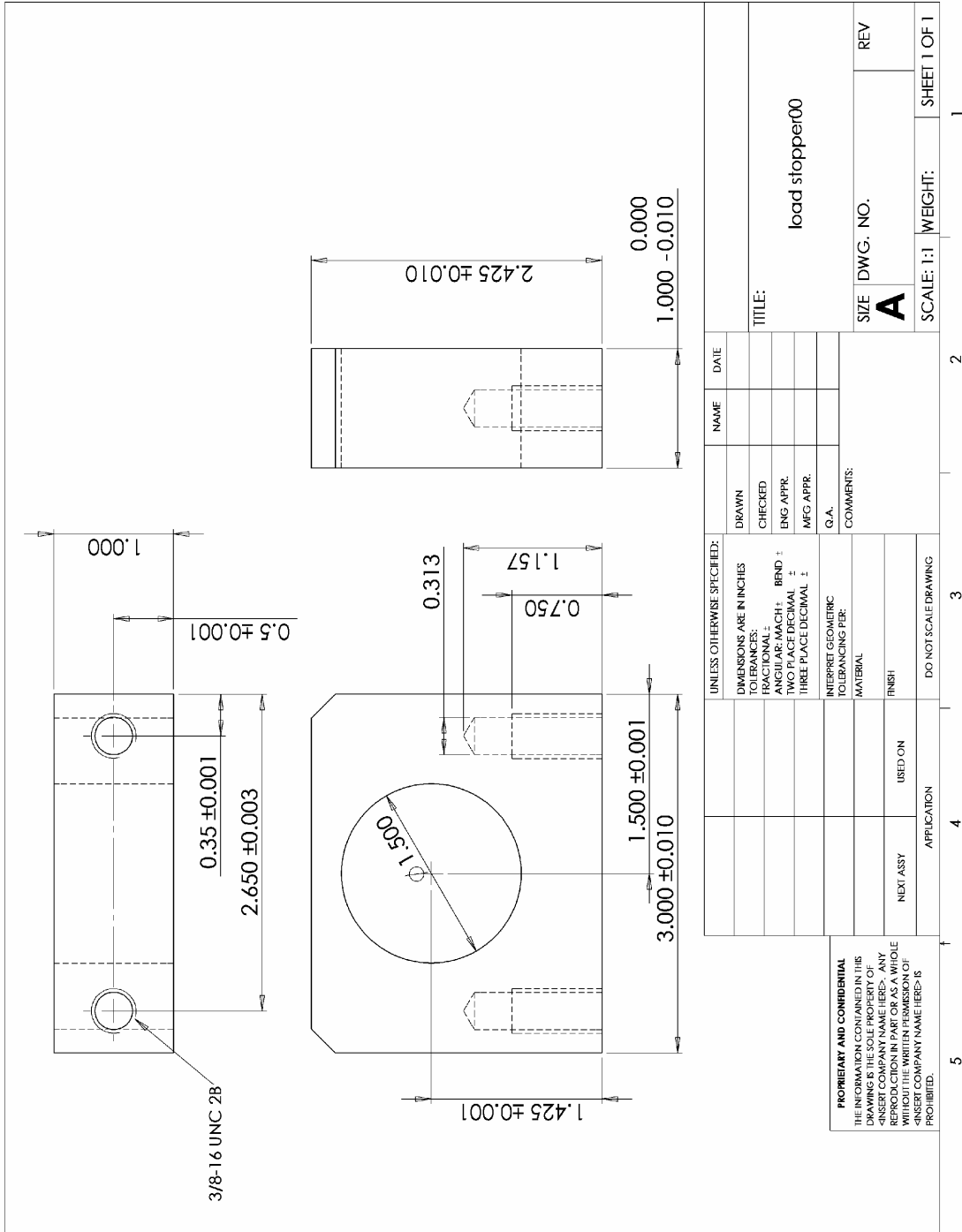
Fig. A.13. Load stopper.
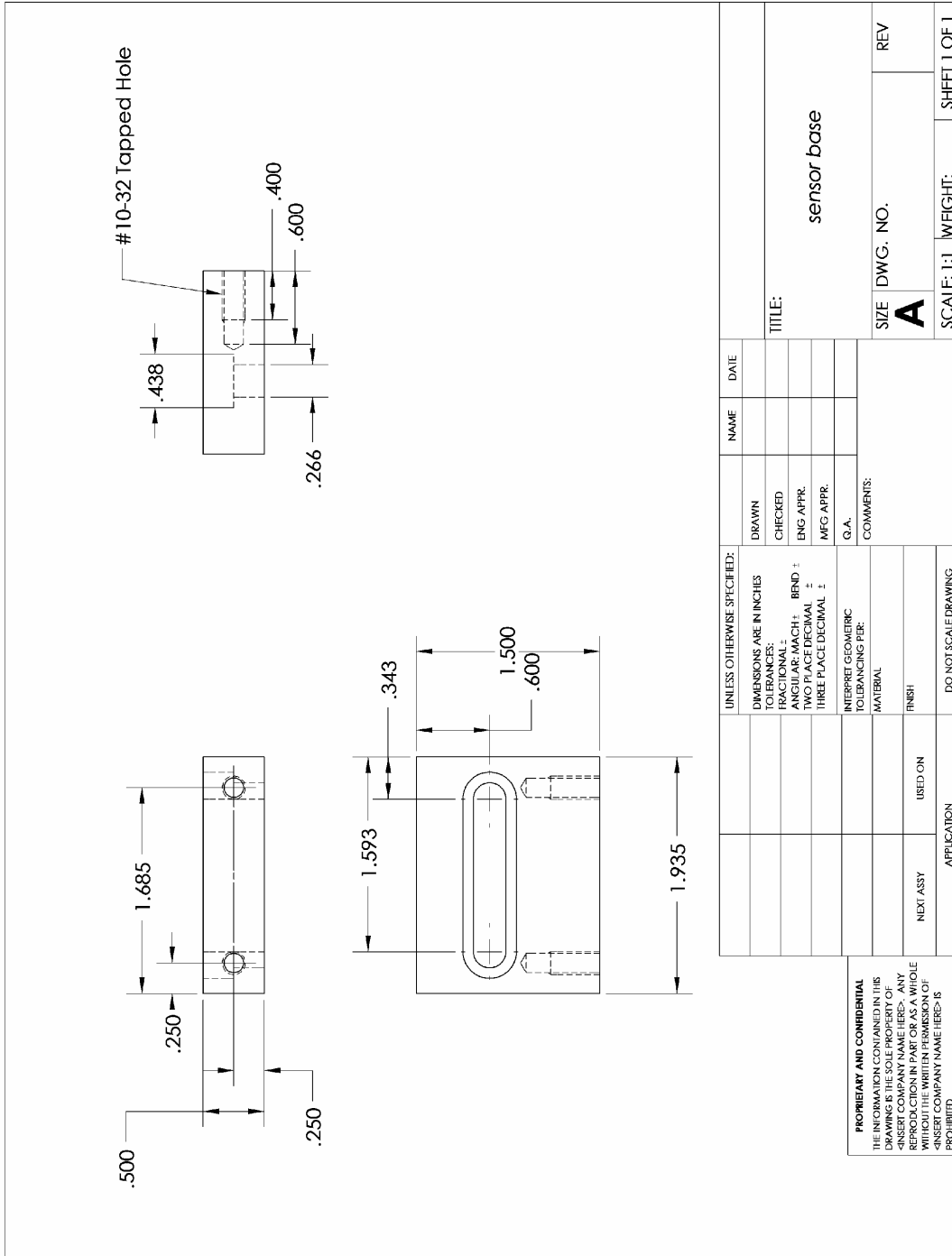
Fig. A.14. Laser sensor base plate.
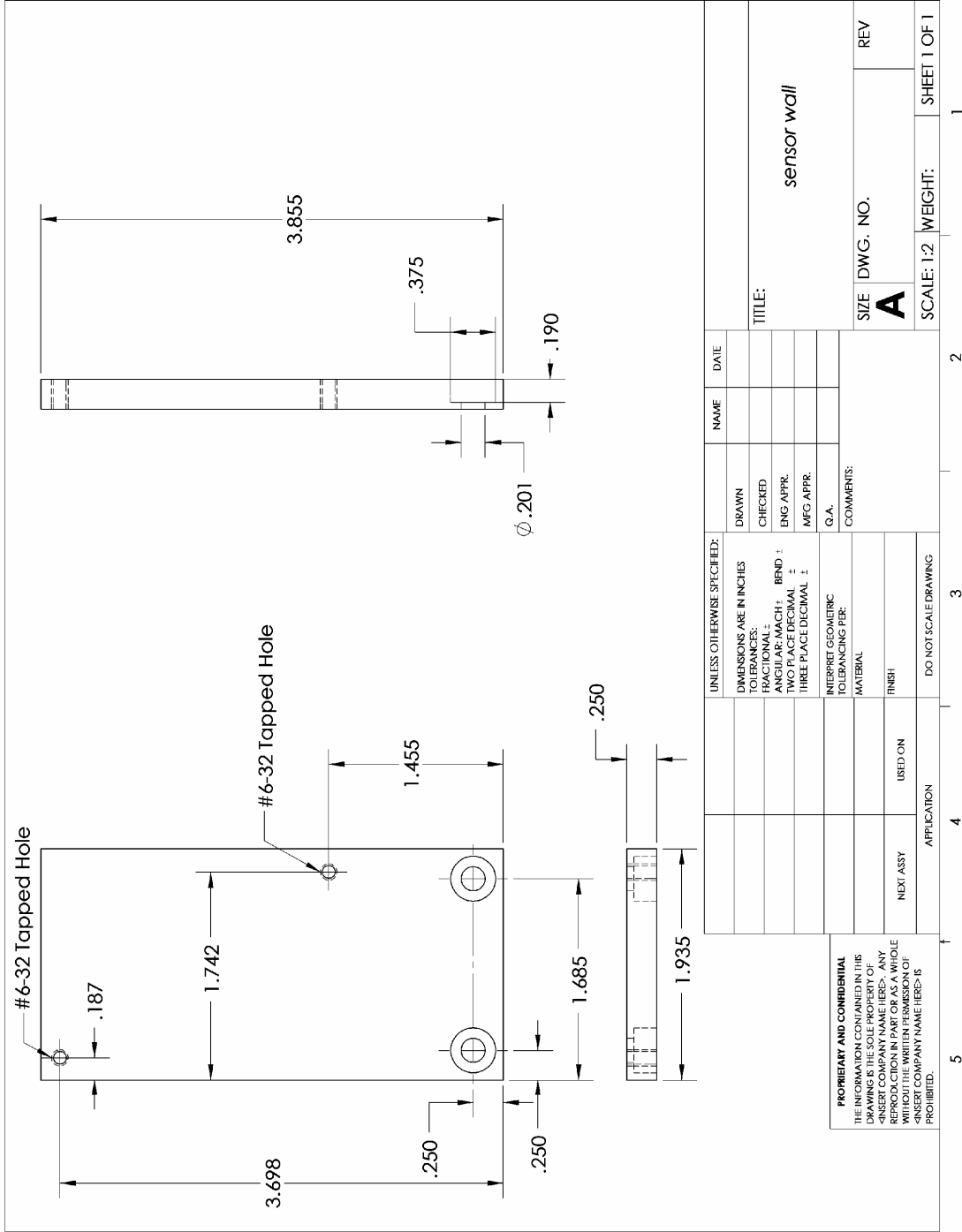
Fig. A.15. Laser sensor side plate.
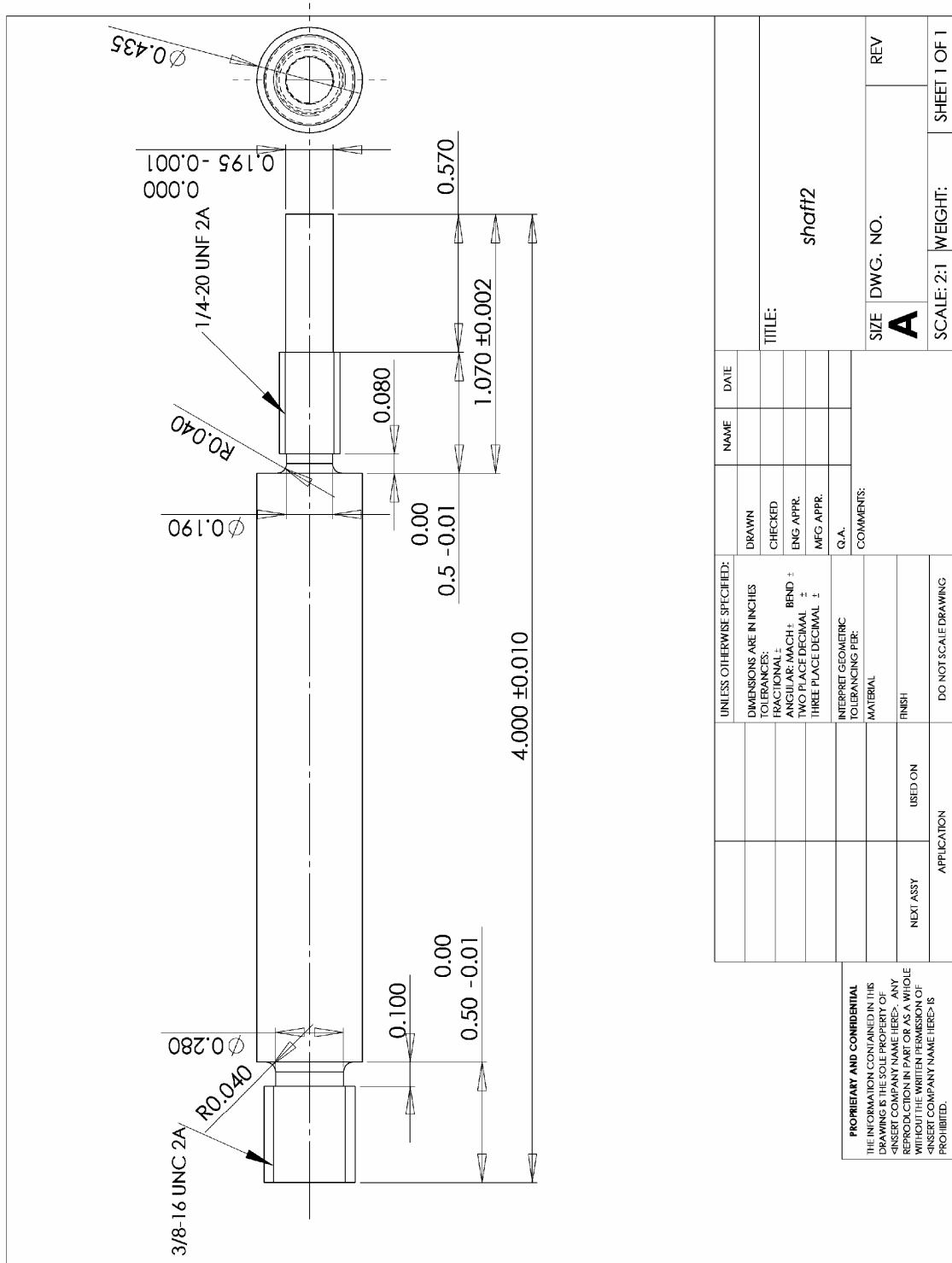
Fig. A.16. Output shaft.
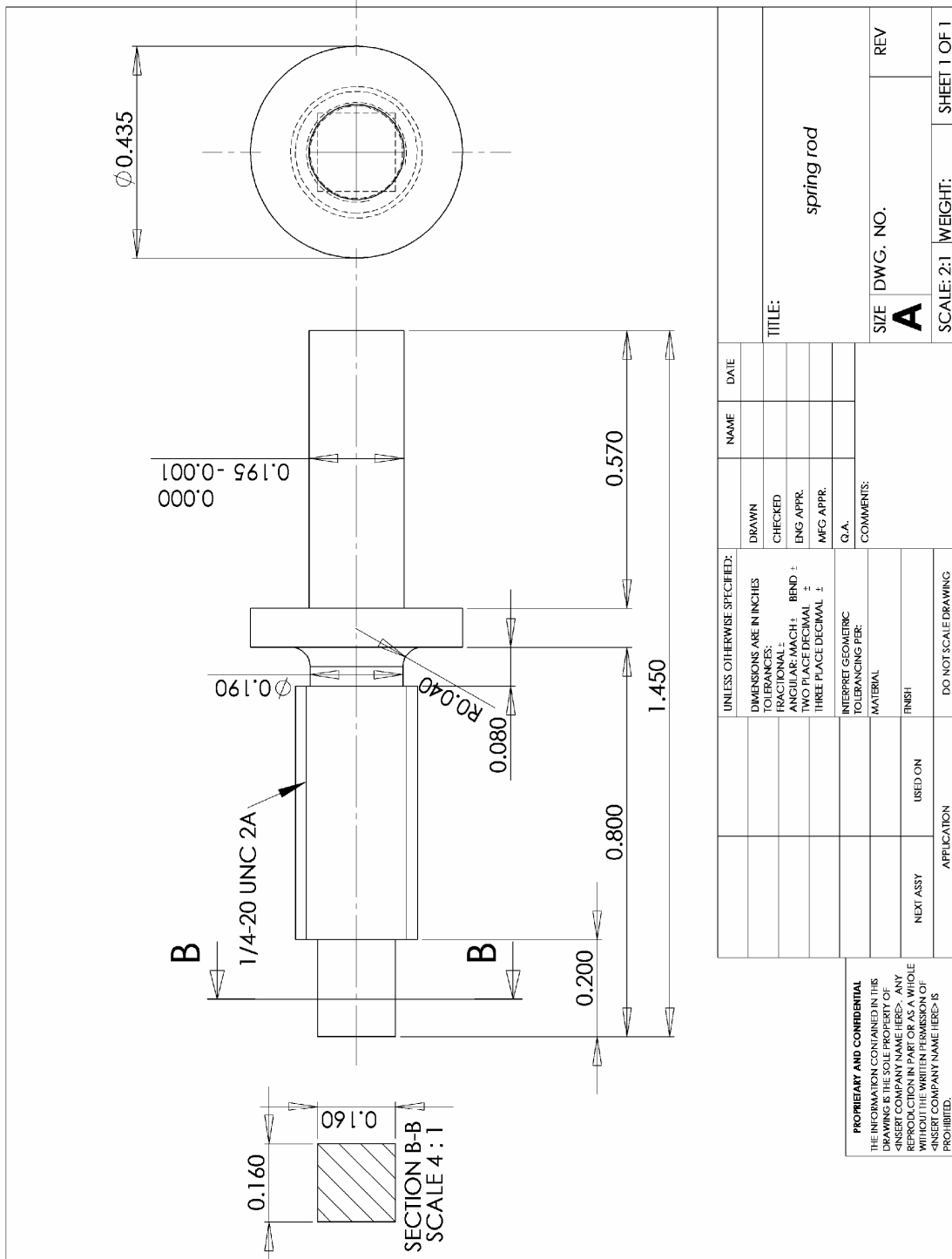
Fig. A.17. Spring shaft.
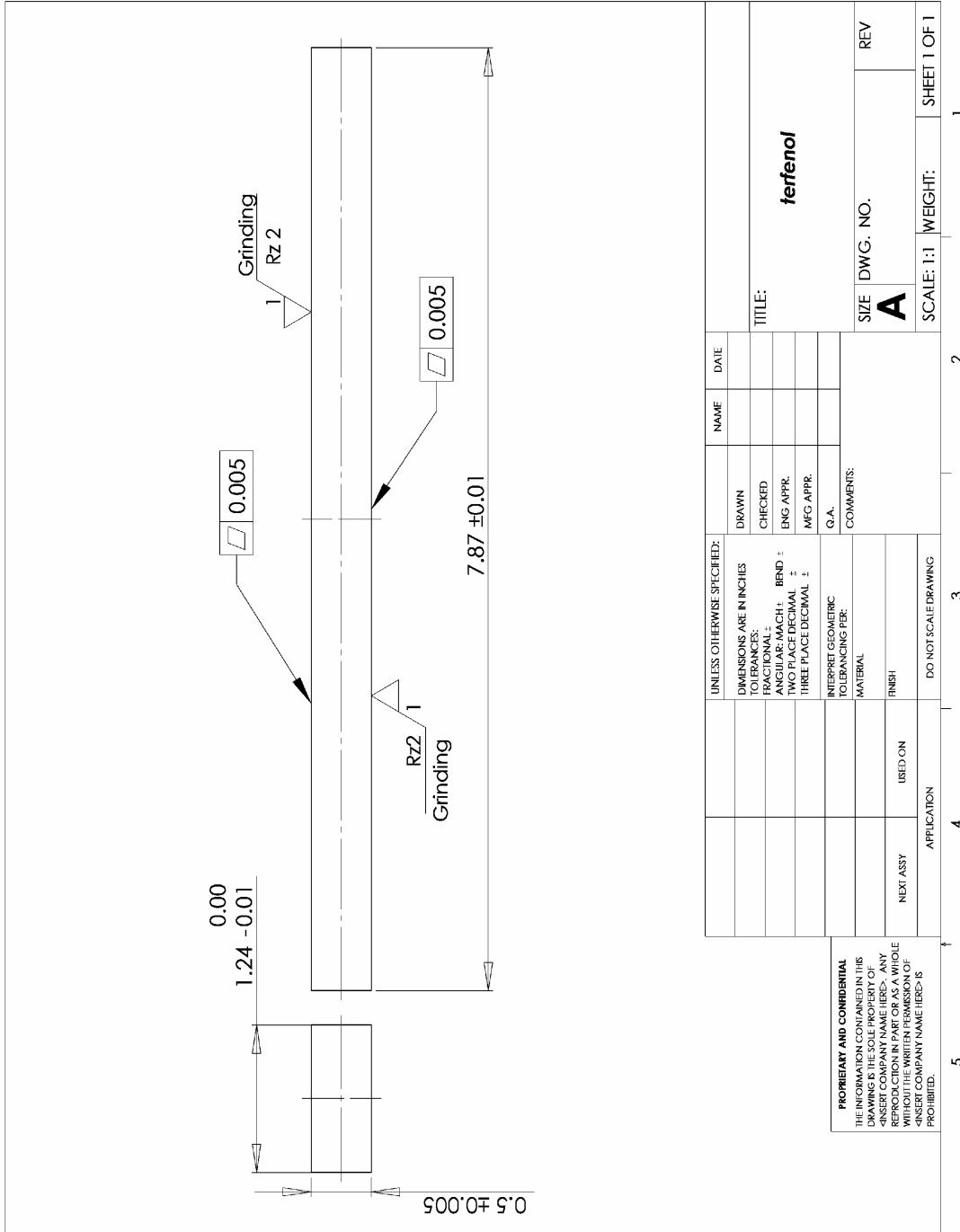
Fig. A.18. Squeezing plate.
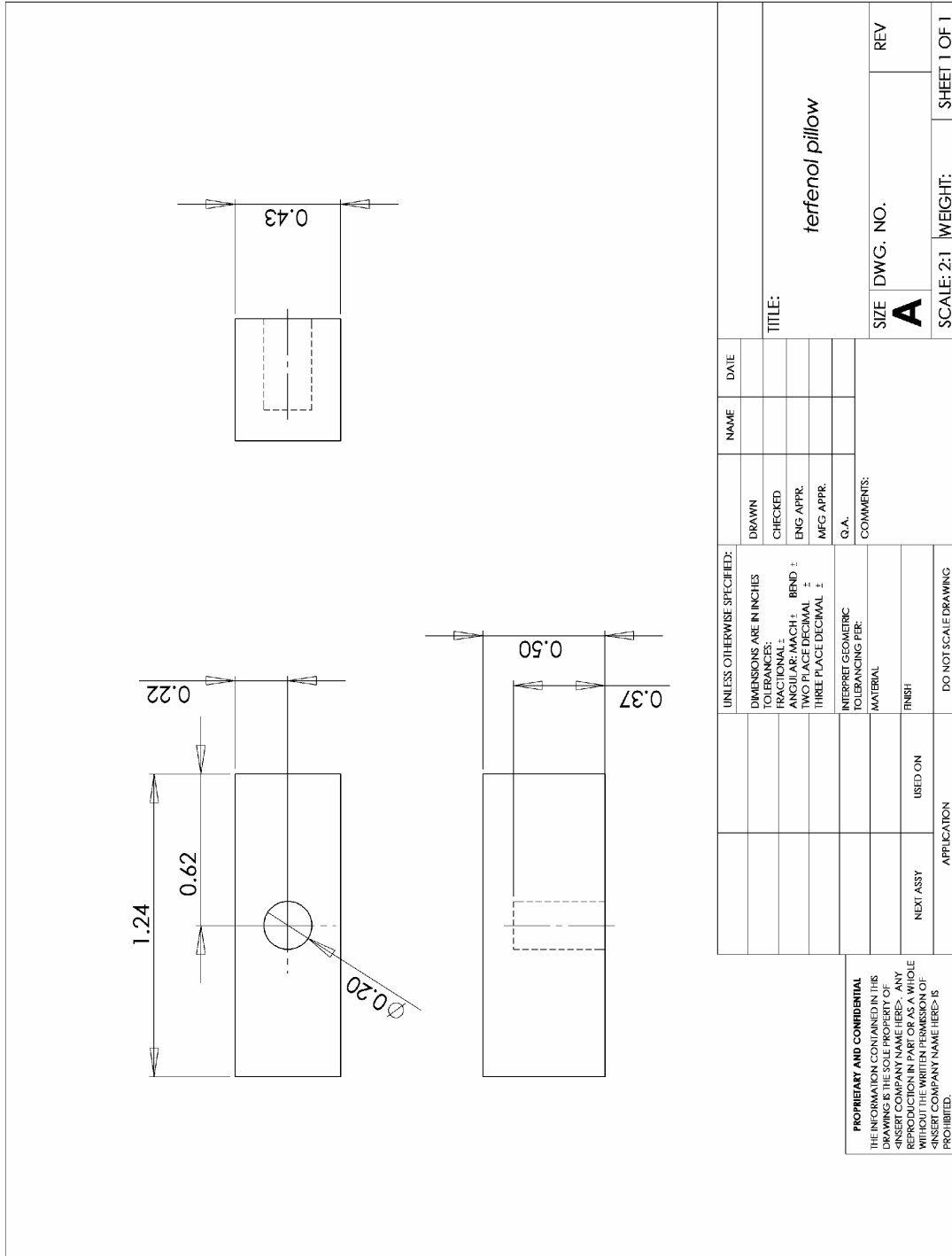
Fig. A.19. Stator.

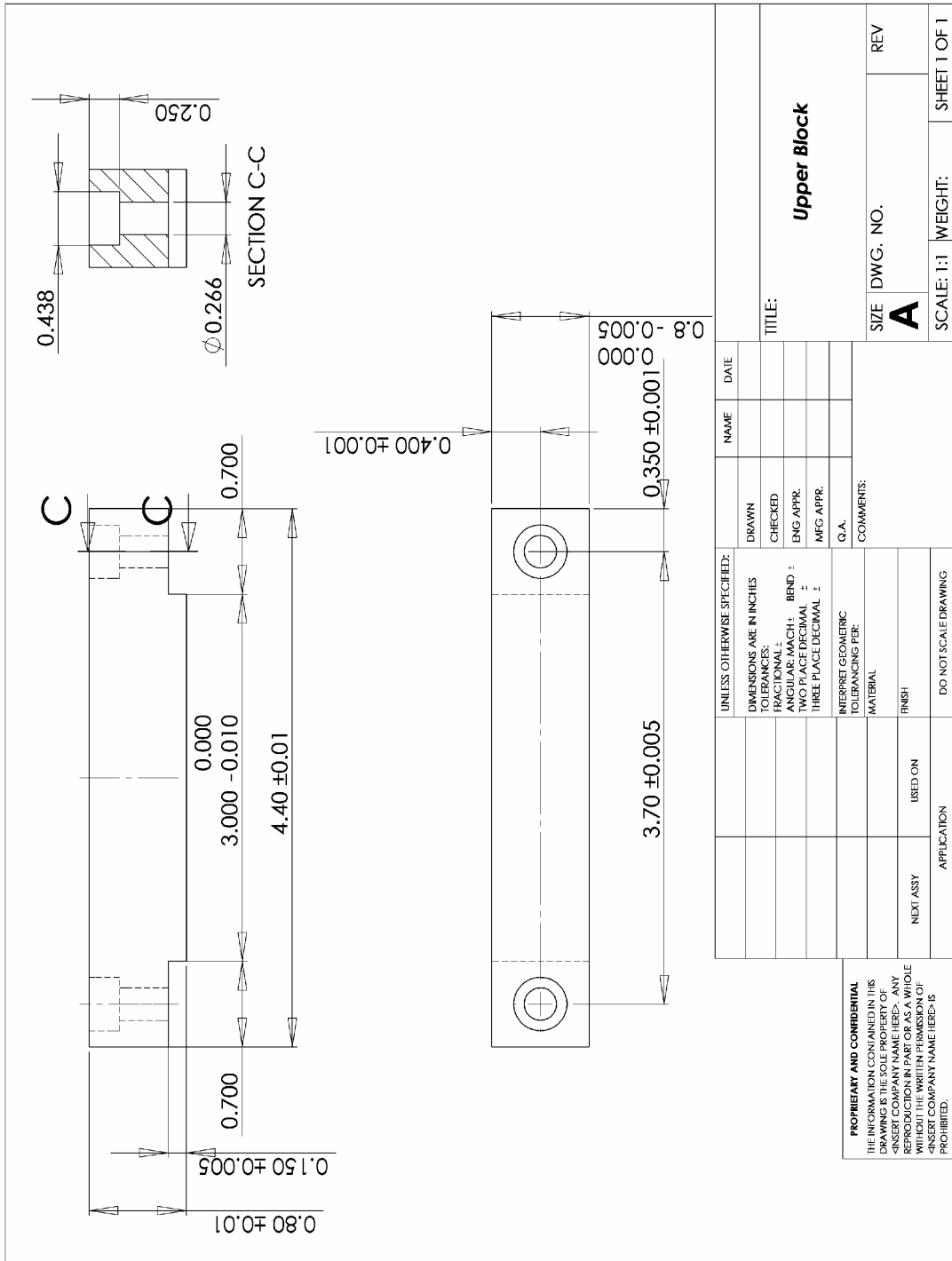Fig. A.20. Terfenol-D slab.

Fig. A.21. Terfenol-D pillow.

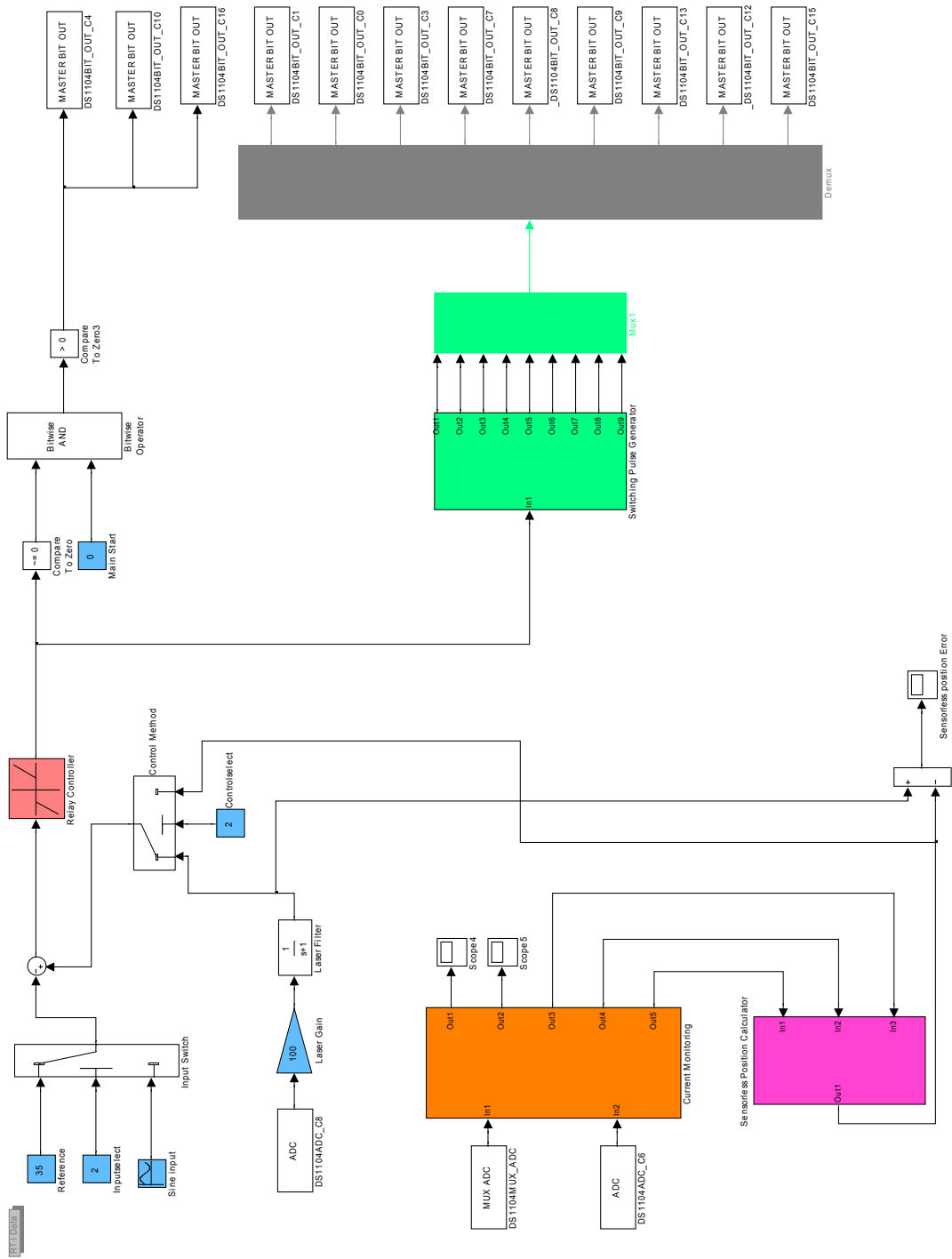Fig. A.22. Upper block.

**APPENDIX B**

**SIMULINK ® BLOCK DIAGRAMS**

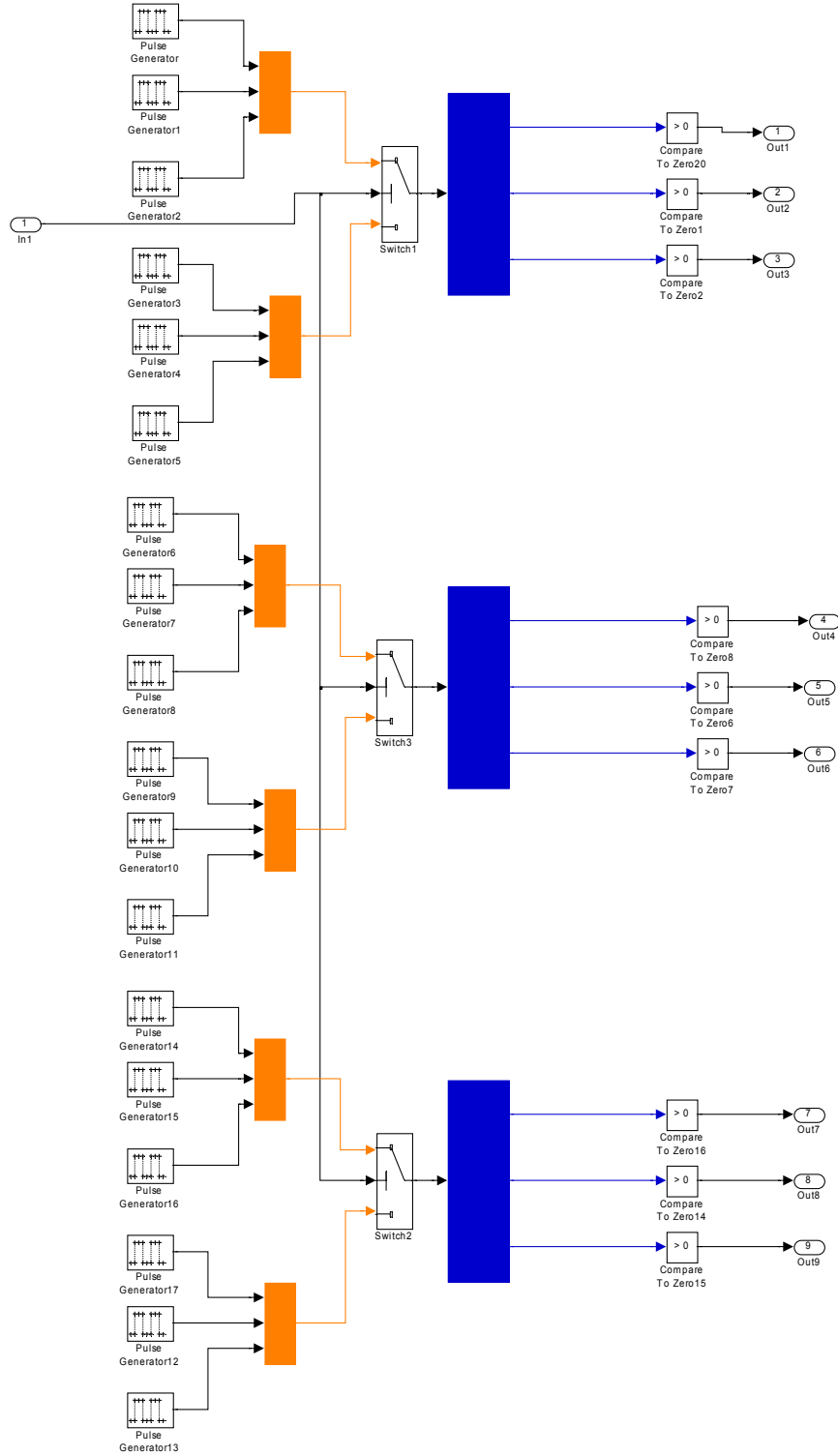Fig. B.1. The Simulink® block diagram for real-time position control.

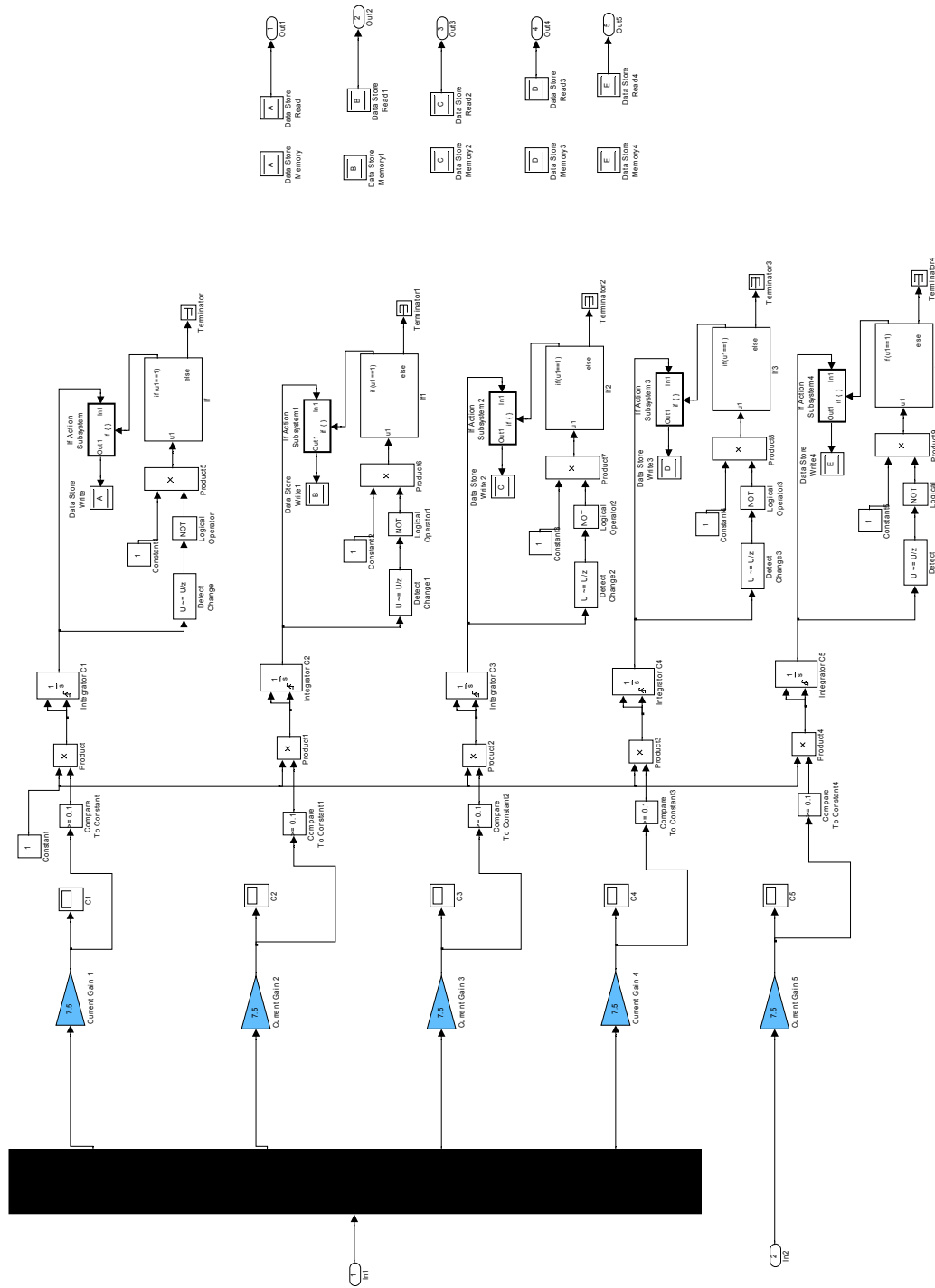Fig. B.2. The Simulink® block diagram for switching pulse generator.

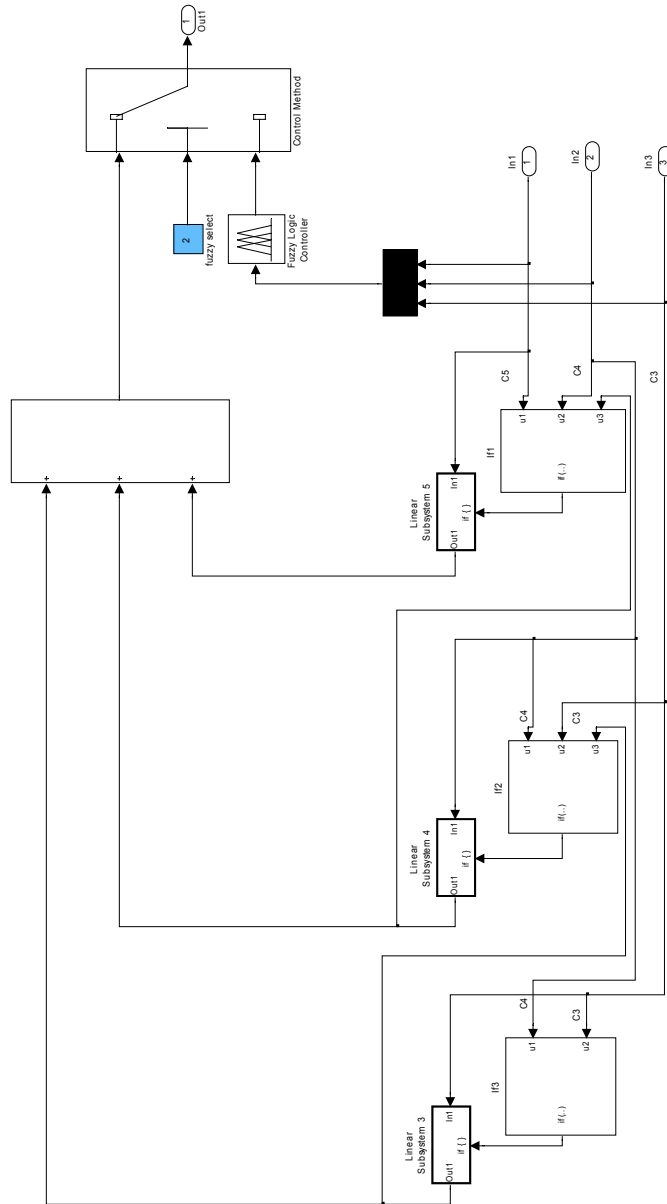Fig. B.3. The Simulink® block diagram for calculating the current pulse widths in sensorless control.

Fig. B.4. The Simulink® block diagram for sensorless position estimation.
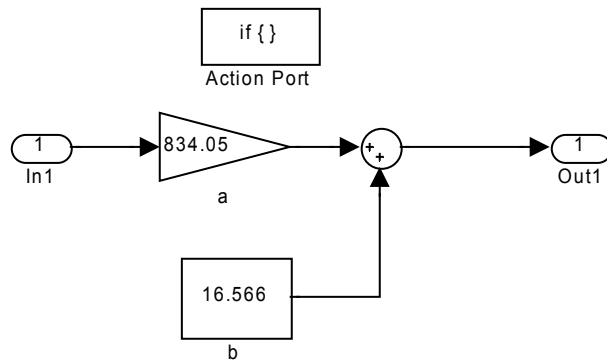
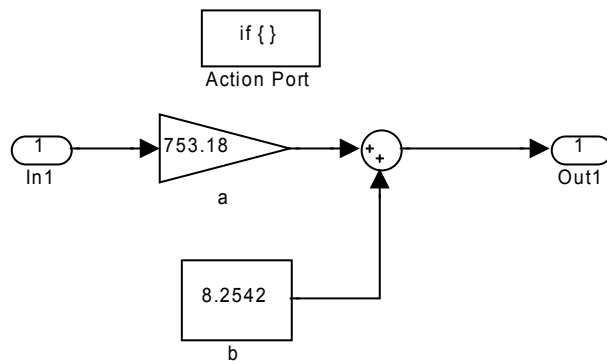Fig. B.5. The Simulink® block diagram for linear subsystem 3 in sensorless control.



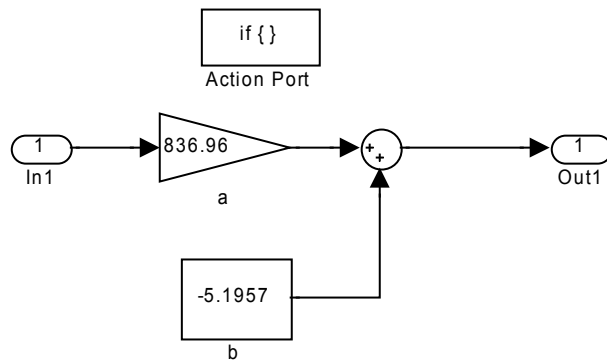Fig. B.6. The Simulink® block diagram for linear subsystem 4 in sensorless control.



Fig. B.7. The Simulink® block diagram for linear subsystem 5 in sensorless control

# VITA

## ALI SADIGHI

**Education**

**Texas A&M University**, College Station, TX. August 2010,
Doctor of Philosophy in mechanical engineering.

**K.N.Toosi University of Technology**, Tehran, Iran. July 2003,
Master of Science in mechanical engineering.

**Sharif University of Technology**, Tehran, Iran. July 2000,
Bachelor of Science in mechanical engineering.

**Journal Publications**

[1]    W.-J. Kim and **A. Sadighi**, "Novel low-power linear magnetostrictive actuator with local three-phase excitation," *IEEE/ASME Transactions on Mechatronics*, vol. 15, no. 2, pp. 299–307, Apr. 2010.

[2]    **A. Sadighi** and W.-J. Kim "Adatptive-neuro-fuzzy-based sensorless control of a smart-material actuator," in print, *IEEE/ASME Transactions on Mechatronics*, March 2010.

[3]    **A. Sadighi** and W.-J. Kim "Sensorless control of a novel linear magnetostrictive motor" Submitted to *IEEE Transactions on Industry Applications*.

**Awards**

***Best Student Paper Award Finalist***, *IEEE/ASME International Conference on Advanced Intelligent Mechatronics*, Montreal, Canada, July 2010.

**Address**
Texas A&M University
Department of Mechanical Engineering
3123 TAMU
College Station, TX 77843-3123